

NASA Contractor Report 202008

**National Aeronautics and Space Administration
(NASA)/American Society for Engineering Education
(ASEE) Summer Faculty Fellowship Program - 1996**

Volume 2

Richard B. Bannerot and Donn G. Sickorez, Editors

Grant NAG 9-867



June 1997

NASA Contractor Report 202008

National Aeronautics and Space Administration (NASA) American Society of Engineering Education (ASEE) Summer Faculty Program - 1996

Volume 2

Richard B. Bannerot, Editor

*University of Houston
Houston, Texas*

Donn G. Sickorez, Editor

*University Programs Office
Lyndon B. Johnson Space Center
Houston, Texas*

Grant NAG 9-867



National Aeronautics and
Space Administration

June 1997

PREFACE

The 1996 Johnson Space Center (JSC) National Aeronautics and Space Administration (NASA)/American Society for Engineering Education (ASEE) Summer Faculty Fellowship Program was conducted by the University of Houston and JSC. The 10-week program was operated under the auspices of the ASEE. The program at JSC, as well as the programs at other NASA Centers, was funded by the Office of University Affairs, NASA Headquarters, Washington, D.C. The objectives of the program, which began in 1965 at JSC and in 1964 nationally, are:

1. To further the professional knowledge of qualified engineering and science faculty members.
2. To stimulate an exchange of ideas between participants and NASA.
3. To enrich and refresh the research and teaching activities of participant's institutions.
4. To contribute to the research objectives of the NASA Centers.

Each faculty fellow spent at least 10 weeks at JSC engaged in a research project commensurate with his/her interests and background and worked in collaboration with a NASA/JSC colleague. This document is a compilation of the final reports on the research projects done by the faculty fellows during the summer of 1996. Volume 1 contains the first 12 reports, and volume 2 contains the remaining 13 reports.

Page intentionally left blank

CONTENTS

Volume 1

1.	ANDERSON, Gary: <i>Intelligent System Development Using a Rough Sets Methodology</i>	1-1
2.	BACHNAK, Rafic: <i>Electronic Design Automation: Integrating the Design and Manufacturing Functions</i>	2-1
3.	BASCIANO, Thomas: <i>Development of Methods to Evaluate Safer Flight Characteristics</i>	3-1
5.	BISHOP, Phillip: <i>Measurement of Carbon Dioxide Accumulation and Physiological Function in the Launch and Entry and Advanced Crew Escape Suit</i>	5-1
6.	BLACKWELL, Harvel: <i>Analysis of Flow from ARC-Jet Spectra</i>	6-1
7.	CACCESE, Vincent: <i>Design Criteria for X-CRV Honeycomb Panels – A Preliminary Study</i>	7-1
8.	CHOLEWIAK, Roger: <i>Studies of the Interactions Between Vestibular Function and Tactual Orientation Display Systems</i>	8-1
9.	COOMBS, Cassandra: <i>There's Iron in Them Thar Hills: A Geologic Look at the Aristarchus Plateau as a Potential Landing Site for Human Lunar Return</i>	9-1
11.	GIARRATANO, Joseph: <i>Inherit Space</i>	11-1
12.	HARVEY, Ralph: <i>Studies of Magmatic Inclusions in the Basaltic Martian Meteorites Shergotty, Zagami, EETA 79001 and QUE 94201</i>	12-1
13.	HAYES, Linda: <i>Developing Tools and Techniques to Increase Communication Effectiveness</i>	13-1
14.	HOGAN, Harry: <i>Estimating Trabecular Bone Mechanical Properties from Non-Invasive Imaging</i>	14-1

Volume 2

15.	JANIKOW, Cezary: <i>Improving Search Properties in Genetic Programming</i>	15-1
17.	KIME, Yolanda: <i>Prediction of Degraded Strength in Composite Laminates with Matrix Cracks</i>	17-1
18.	KLEIS, Stanley: <i>Bioreactor Mass Transport Studies</i>	18-1
19.	KOEHLERT, Erik: <i>Developing a Graphical User Interface for the ALSS Crop Planning Tool</i>	19-1
20.	LEMOINE, Sandra: <i>A Comparison of Total and Intrinsic Muscle Stiffness among Flexors and Extensors of the Ankle, Knee and Elbow</i>	20-1

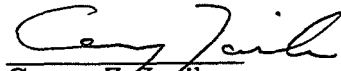
21.	LEON, V.: <i>Integration of CELSS Simulation with Long-Term Crop Scheduling</i>	21-1
22.	MCGINNIS, Michael: <i>Influence of Zero-shear on Yeast Development</i>	22-1
23.	MULLEN, Terence: <i>Computer Based Training: Field Deployable Trainer & Shared Virtual Reality</i>	23-1
24.	PATE, Dennis: <i>A Human Factors Analysis of EVA Time Requirements</i>	24-1
25.	RICHARDSON, Albert: <i>Simulation of the Predictive Control Algorithm for Container Crane Operation Using MATLAB Fuzzy Logic Tool Box</i>	25-1
27.	WASSIL-GRIMM, Andrew: <i>Database Development for Electrical, Electronic and Electromechanical (EEE) Parts for the International Space Station ALPHA</i>	27-1
28.	WILLIAMS, Trevor: <i>Dynamics Questions Associated with the AERCam Sprint Free-Flyer</i>	28-1
29.	WNUK, Michael: <i>Analysis of Impact Induced Damage and its Effect on Structural Integrity of Space Flight Composite Overwrapped Pressure Vessels</i>	29-1

Improving Search Properties in Genetic Programming

Cezary Z. Janikow and Scott DeWeese (student)
Department of Mathematics and Computer Science
University of Missouri at St. Louis
St. Louis, MO 63121

June 24, 1996

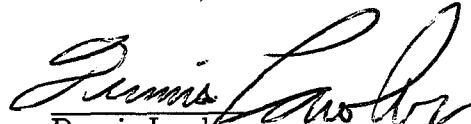
Dennis Lawler
Intelligent Systems Branch
Automation, Robotics and Simulation Division
Engineering Directorate



Cezary Z. Janikow



Scott DeWeese



Dennis Lawler

Improving Search Properties in Genetic Programming

Final Report

NASA/ASEE Summer Faculty Fellowship Program – 1996

Johnson Space Center

Prepared By: Cezary Z. Janikow, Ph.D.
Scott DeWeese
Academic Rank: Assistant Professor
Student
University & Department: University of Missouri – St. Louis
Department of Mathematics and
Computer Science
St. Louis, MO 63121

NASA/JSC

Directorate: Engineering
Division: Automation, Robotics and Simulation
Branch: Intelligent Systems
JSC Colleague: Dennis Lawler
Date Submitted: July 15, 1996
Contract Number: NAG-9-867

ABSTRACT

With the advancing computer processing capabilities, practical computer applications are mostly limited by the amount of human programming required to accomplish a specific task. This necessary human participation creates many problems, such as dramatically increased cost. To alleviate the problem, computers must become more autonomous. In other words, computers must be capable to program/reprogram themselves to adapt to changing environments/tasks/demands/domains.

Evolutionary computation offers potential means, but it must be advanced beyond its current practical limitations. Evolutionary algorithms model nature. They maintain a population of structures representing potential solutions to the problem at hand. These structures undergo a simulated evolution by means of mutation, crossover, and a Darwinian selective pressure. Genetic programming (GP) is the most promising example of an evolutionary algorithm. In GP, the structures that evolve are trees, which is a dramatic departure from previously used representations such as strings in genetic algorithms. The space of potential trees is defined by means of their elements: functions, which label internal nodes, and terminals, which label leaves. By attaching semantic interpretation to those elements, trees can be interpreted as computer programs (given an interpreter), evolved architectures, etc.

JSC has begun exploring GP as a potential tool for its long-term project on evolving dextrous robotic capabilities. Last year we identified representation redundancies as the primary source of inefficiency in GP. Subsequently, we proposed a method to use problem constraints to reduce those redundancies, effectively reducing GP complexity. This method was implemented afterwards at the University of Missouri. This summer, we have evaluated the payoff from using problem constraints to reduce search complexity on two classes of problems: learning boolean functions and solving the forward kinematics problem. We have also developed and implemented methods to use additional problem heuristics to fine-tune the searchable space, and to use typing information to further reduce the search space. Additional improvements have been proposed, but they are yet to be explored and implemented.

INTRODUCTION

Solving a problem on the computer involves two elements: a proper representation for potential solutions of the problem, and a search mechanism to explore the space spanned by the representation. In the simplest case of computer programs, the two elements are not explicitly separated and instead are hard-coded in the programs. However, separating them has numerous advantages, such as reusability for other problems which may require only modified representation. This idea has been long realized and practiced in artificial intelligence. There, one class of algorithms borrows ideas from nature, such as population dynamics, selective pressure, and information inheritance by offspring, to organize its search. This is the class of *evolutionary algorithms*.

Genetic algorithms (GAs) [1, 2, 3] are the most extensively studied and applied evolutionary algorithms. A GA uses a population of chromosomes coding individual potential solutions. These chromosomes undergo a simulated evolution facing Darwinian selective pressure. Chromosomes which are better with respect to a simulated environment have increasing survival chances. In this case, the measure of fitness to this environment is based on the quality of a chromosome as a solution to the problem being solved. Chromosomes interact with each other via *crossover* to produce new offspring solutions, and they are subjected to *mutation*.

Most genetic algorithms operate on fixed-length chromosome strings, which may not be suitable for some problems. To deal with this, some genetic algorithms adapted variable-length representation, as for machine learning [2]. Moreover, traditional genetic algorithms use low-level binary representation, but many recent applications use other abstracted alphabets [1].

Genetic programming (GP) [5, 6, 7] uses trees to represent chromosomes. At first used to generate LISP computer programs, GP is also being used to solve problems where solutions have arbitrary interpretations [5]. Tree representation is richer than that of linear fixed-length strings. However, there is a price to pay for this richness.

In general, the number of trees should equal the number of potential solutions, with one-to-one mapping between them. Unfortunately, this is hardly ever possible. Because we need each potential solution to be represented, the number of trees will tend to be much larger, with some of them being redundant or simply invalid. Therefore, some means of dealing with such cases, such as possibly avoiding the exploration of such extraneous trees, may be desired. Our preliminary experiments indicate that in fact reducing the search space does indeed improve search efficiency.

While for some problems some *ad-hoc* mechanisms for reducing the necessary search have been proposed [5, 6], there is no general methodology. Our objective is to provide a general systematic means, while also making sure that the means does not increase the overall computational complexity. During our last year's tenure at JSC, we explored a number of alternatives for identifying subspaces of trees, and we eventually proposed:

- a constraint specification language
- methods to modify existing GP mechanisms generating initial populations and offspring by crossover and mutation, which modifications would guarantee that only trees satisfying the specified constraints would ever evolve

lilgp [9] is a tool for developing GP applications. JSC has selected this tool for its work with GP. Funded by a follow-up grant from last year's Summer Program, we have modified *lil-gp* to read problem constraints, and to constrain its search in so-defined restricted space. Moreover, the modifications necessary to guarantee constraint satisfaction were shown not to increase the overall complexity of evolution of a single offspring [4].

The constraint specification language has two parts:

- one part allows the specification of constraints based on types of data, as related to function ranges and argument domains,
- the other part allows the specification of additional constraints based on semantic interpretation of either data or specific functions.

However, each individual function was restricted to a single type: *function overloading* was not possible. For example, the '+' function could not be used differently based on the fact that integer arguments generate integers, while floating point arguments generate floating point results. This summer we have explored such extended specifications, and subsequently we have proposed a methodology which processes such information yet still guarantees offspring feasibility and stays within the same evolution complexity per offspring. We have also explored ways to incorporate additional problem heuristics, and some mechanisms have been implemented. In the remaining part of this report we will briefly explain the two issues, and we will conclude with a few experimental results evaluating constrained evolution.

PREVIOUSLY IMPLEMENTED CONSTRAINTS

The previously implemented constraint specification language allow the incorporation of data-type information to limit potential tree structures. The constraints include:

- for each function
 - which functions can call this function (based on data type returned by the function)
 - which functions can be called by this function on each of its arguments (based on data type returned by the function)
 - the same as above based on semantic interpretations
- for each terminal
 - which functions can use the terminal values

The above information is preprocessed (which includes resolving inconsistencies and generating a minimal *normal form* for the constraints) and compiled into so called *mutation sets*.

To begin the simulation, the initial population must be generated. To generate a single tree, problem specifications are consulted to decide what potential functions can be used for the root of the tree. Once a plausible function is selected, its arity determines the number of children that must be recursively generated. Each child uses one of the functions/terminals

allowed (as expressed in the mutation sets) on the particular argument of the selected parent function. Given that, only constraint-satisfied programs would ever be initialized.

The two evolution operators (mutation and crossover) are similarly defined to guarantee that each offspring satisfies the normal constraints. Mutation is implemented similarly to the above initialization, except that mutation starts from an arbitrary node of an existing tree rather than from the absolute root. Crossover exchanges subtrees between two existing trees. Constrained crossover selects source material in such a way the the root of the subtree being moved to a destination tree uses a function listed in the mutation set for the parent's function.

[4] presents details of the constraints specification language, proves that the normal form represents the same constraints in a minimal form, that initialization/mutation/crossover indeed guarantee offspring feasibility, and that the necessary overhead is minimal and constant (*e.g.*, evolution complexity per offspring does not change except for small constant values).

WORK COMPLETED THIS SUMMER

This summer we have accomplished the following: conducted experiments aimed at evaluating changes in search properties under constrained search, implemented mechanisms allowing the use of additional problem heuristics and the use of overloaded functions, and conducted another set of experiments aimed at evaluating application of constrained search to selected robotic arm kinematics problems.

Evaluating Search Properties using 11-Multiplexer

A multiplexer is a boolean circuit with a number of inputs and exactly one output. In practical applications, a multiplexer is used to propagate exactly one of the inputs to the output. For example, in the computer CPU (central processing unit), multiplexers are used to direct the flow of digital information. The 11-multiplexer has two kinds of binary inputs: address ($a_0 \dots a_2$) and data ($d_0 \dots d_7$). It implements a boolean function, which can be expressed in DNF (disjunctive normal form) as:

$$a_2 a_1 a_0 d_7 \vee a_2 a_1 \bar{a}_0 d_6 \vee a_2 \bar{a}_1 a_0 d_5 \vee a_2 \bar{a}_1 \bar{a}_0 d_4 \vee \bar{a}_2 a_1 a_0 d_3 \vee \bar{a}_2 a_1 \bar{a}_0 d_2 \vee \bar{a}_2 \bar{a}_1 a_0 d_1 \vee \bar{a}_2 \bar{a}_1 \bar{a}_0 d_0$$

In [6], Koza has proposed to use the following function set $F_I = \{and, or, not, if\}$ and terminals $F_{II} = \{a_0 \dots a_2, d_0 \dots d_7\}$ for evolving the 11-multiplexer function with GP.

The function set is obviously complete, thus satisfying *sufficiency*. However, the set is also redundant — subsets of F_I , such as $\{and, not\}$, are known to be sufficient to represent any boolean formula. Thus, by placing restrictions on function use, we may reduce the amount of redundant subspaces in the representation space, and thus study the relationship between space redundancy and search efficiency. Moreover, in another experiment we artificially invalidated some of the redundant subspaces, which allowed us to compare the effects of explicitly removing invalid search spaces against the effects of other currently used methods.

When it comes to removing redundant search spaces, the impact can be both positive and negative. We conjecture that some of the spaces are "easier" for the solutions to evolve, using mutation and crossover. For example, we observed that *if* was a sufficient function

for the problem, and that the solution space involving this function only provided the most efficient search, both in terms of the simulation length required and the amount of processing necessary per simulation unit. On the other hand, some space reductions (especially those restricting the use of *if*) actually slowed down evolution. Accordingly, we have concluded that evolving a proper representation is indeed a very important goal for the future.

When parts of the GP search space involves invalid solutions, the state of the art approach involves either penalizing such solutions, or re-interpreting them as redundant solutions. We experimented with an approach in which constraints were used to explicitly disallow searching such spaces. We have observed that this approach always outperformed the existing approaches.

Incorporating Additional Problem Heuristics

We have implemented a new version, which can differentiate (using user supplied weights) between different elements of the mutation sets, that is functions/terminals allowed to label appropriate children. In the previous version, such elements were simply either allowed or disallowed. This new version allows the user to provide "soft" constraints, or heuristics. For example, suppose that the hypothesis that the *if* function should be used by itself for the 11-multiplexer problem, but the user is not sure about that. These weights can be used to specify that evolution should use this function most of the time, but nevertheless other functions can be explored as well.

This implementation is important for another reason: it can now be extended to modify those weights, and thus to evolve the representation used for problem solving.

Overloaded Functions

The previously implemented version allowed functions and terminals to be "typed", and this information (in addition to additional semantic information) was used to arrive at the constraints. However, in programming languages *function overloading* is a very powerful feature that could not be used with that implementation. For example, consider a problem where masses (*lb*) and times (*sec*) were being processed to evolve some distance equation. Both masses and times may have to be added, subtracted, divided, *etc.* . Moreover, when a mass is divided by another mass, a "unitless" fraction is computed, which when multiplied by a time gives a time again. Thus, the arithmetical functions produce different results in different contexts, and thus cannot be uniformly constrained.

We have developed a methodology to include such information with functions and terminals, and to process this information to further constrain the search space. This is version *v2.0*, which is being left at JSC.

Experiments with Inverse Kinematics

To assess the applicability of GP to robotic problems, and to evaluate the effectiveness of constraining the search space of functional descriptions, we have conducted a series of experiments involving a 2-D robotic arm. In the experiments, we assumed that the goal was to evolve a functional description for setting the two joints (angles) so that the arm tip would move to the vicinity of a given reachable position. In other words, the objective was to evolve a program that could read two variables ($x - y$ destination) and would output two values (the two angles for the joints).

This problem has been previously investigated by Koza [6], but his results were rather sketchy. An analytical solution involves trigonometric and arithmetical functions:

$$\phi_0 = \text{atan2}(y, x) \pm \text{acos} \left(-\frac{l_2^2}{2 \cdot l_1 \cdot \sqrt{x^2 + y^2}} + \frac{l_1}{2 \cdot \sqrt{x^2 + y^2}} + \frac{\sqrt{x^2 + y^2}}{2 \cdot l_1} \right)$$

$$\phi_1 = \mp \pi \pm \text{acos} \left(-\frac{x^2 + y^2}{2} + \frac{l_1}{2 \cdot l_2} + \frac{l_2}{2 \cdot l_1} \right)$$

We have conducted two separate sets of experiments, differing by the function set used:

- $F_I = \{fkin, \text{atan2}, \text{acos}, \text{hypot}, +, -, /, *\}$
 $F_{II} = \{x, y, \pi, 1, 2, l_1, l_2, l_{1.2}\}$
- $F_I = \{fkin, \text{atan2}, \text{acos}, \text{hypot}, +, -, /, *, \text{asin}, \text{sin}, \text{cos}, \text{sqrt}, \text{exp}\}$
 $F_{ii} = \{x, y, \pi, 1, 2, l_1, l_2, l_{1.2}\}$

where *fkin* is a function that makes a vector of its two arguments, *hypot* is a function computing the square root of the sum of squares of its two arguments (e.g., the distance of a point from the origin, and the remaining were the standard functions).

For each set, we have conducted four different experiments, with various levels of constraints. For invalid programs that might evolve in the less-constrained cases, we modified interpretations to ensure that each tree could be evaluated as a solution. For example, if the vector-constructing function *fkin* appeared as an argument to a function requiring a scalar, only the first element of the vector was used. When a function received an argument out of its domain, it simply passed the argument, bypassing the function itself.

- E_0 . There were no constraints in the experiment, thus every function was allowed to call any function or use any terminal.
- E_1 . In this experiment, we observe that *fkin* should only be placed at the root of a tree to create a vector, and at no other place. Also, the second angle must have information provided about the first angle (following Koza [6]). We specify these constraints using our constraints specifications.
- E_2 . In this experiment, we observe that many function combinations do not make sense, and we remove them explicitly by specifying proper constraints. For example, no trigonometric function can call any like trigonometric function (i.e., functions that compute angles, such as *acos*, cannot provide values to functions that do not expect angles — such as *acos* itself). The *hypot* function is only allowed to operate on the $x - y$ coordinates. Similar restrictions are placed on *atan2*.
- E_3 . In this experiments, we extend the constraints imposed in E_2 by providing data typing and overloading functions. We use *angle*, *length*, *number*, *vector*, and *length-Square* as types. Each function is only allowed to use arguments of the proper type, and to generate types based on their arguments (if overloaded). For example, the multiplication operator produces *lengthSquare* when both arguments are lengths. On the other hand, both arguments cannot be angles since this would produce an invalid *angleSquare* unit.

We have observed that indeed evolution would speed up with increasing constraints. This conclusion is less obvious here than for the 11-multiplexer problem. In particular, E_2 shows dramatic improvements over E_0/E_1 for both function sets. However, E_3 lacks such improvements. More experiments are needed to determine this behavior. One likely explanation, which we are currently testing, relates to the observation that tree sizes in the E_3 experiments increase. This increase can be attributed to constraining out one-child subtrees, leaving the valid trees necessarily denser.

Another important observation was that large variations existed between individual random runs. This has led to the conclusion that the search still lacks some necessary properties, and the observed improvements are for the most part the result of reducing the search space size. While this is a positive conclusion, it also indicates that better search mechanisms are needed. This leads to the suggestion that more operators are needed to further improve search properties of constrained GP.

SUMMARY AND FUTURE RESEARCH

We have developed two new versions. One is capable of evolving overloaded functions, which are constrained differently based on the context in which they appear (types of arguments), and the other allowing processing of some additional heuristics. We have also conducted a number of experiments aimed at evaluating the applicability of the method, which restricts the search space, to improve search properties. These preliminary experiments suggest that processing such constraints lead, in general, to improving the evolution. However, the same experiments suggest that evolving the representation (*i.e.*, evolving some constraints) is a very important means to further improve the evolution, as is the design of new operators.

In programming, it is widely known that program modularization is a very important means. At present, our constraint methodology has only been implemented for a single program (single tree), while *lil-gp* itself allows evolving modular programs (multiple trees). We have developed a preliminary means for extending our methodology, and we plan to implement that in a near future. This should further improve the effectiveness of such GP approaches.

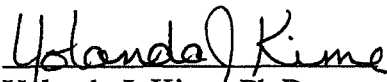
References

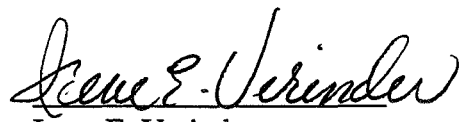
- [1] Davis, L. (ed.). Handbook of Genetic Algorithms. Van Nostrand Reinhold, 1991.
- [2] Goldberg, D.E. Genetic Algorithms in Search, Optimization, and Machine Learning. Addison Wesley, 1989.
- [3] Holland, J. Adaptation in Natural and Artificial Systems. University of Michigan Press, 1975.
- [4] Janikow, C.Z. "A Methodology for Processing Problem Constraints in Genetic Programming". To appear in Computers and Mathematics with Applications.
- [5] Kinnear, K.E. Jr. (ed.). Advances in Genetic Programming. The MIT Press, 1994.
- [6] Koza, J.R. Genetic Programming. The MIT Press, 1992.
- [7] Koza, J.R. Genetic Programming II. The MIT Press, 1994.
- [8] Richardson, J.T., Palmer, M.R., Liepins, G. & Hilliard, M. "Some Guidelines for Genetic Algorithms with Penalty Functions". In Proceedings of the Third International Conference on Genetic Algorithms. Morgan Kaufmann, 1989.
- [9] Zonker, D. & Punch, B. *lil-gp* 1.0 User's Manual. zonker@isl.cps.msu.edu.

PREDICTION OF DEGRADED STRENGTH IN COMPOSITE LAMINATES
WITH MATRIX CRACKS

Yolanda J. Kime
State University of New York, College at Cortland
ES2
8 August 1996

Irene E. Verinder
Structures and Dynamics Branch
Structures and Mechanics Division
Engineering Directorate


Yolanda J. Kime, Ph.D.


Irene E. Verinder

PREDICTION OF DEGRADED STRENGTH IN COMPOSITE LAMINATES
WITH MATRIX CRACKS

Final Report
NASA/ASEE Summer Faculty Fellowship Program - 1996
Johnson Space Center

Prepared by:	Yolanda J. Kime, Ph. D.
Academic Rank:	Associate Professor
University & Department:	Physics Department State University of New York College at Cortland Cortland, NY 13045
NASA/JSC	
Directorate:	Engineering
Branch:	Structures and Dynamics
JSC Colleague:	Irene E. Verinder
Date Submitted:	8 August 1996
Contract Number:	NAG 9-867

ABSTRACT

Composite laminated materials are becoming increasingly important for aerospace engineering. As the aerospace industry moves in this direction, it will be critical to be able to predict how these materials fail. While much research has been done in this area, both theoretical and experimental, the field is still new enough that most computer aided design platforms have not yet incorporated damage prediction for laminate materials. There is a gap between the level of understanding evident in the literature and what design tools are readily available to engineers. The work reported herein is a small step toward filling that gap for NASA engineers.

A computer program, LAMDGRAD, has been written which predicts how some of the materials properties change as damage is incurred. Specifically, the program calculates the Young's moduli E_x and E_y , the Poisson's ratio ν_{xy} , and the shear modulus G_{xy} as cracks develop in the composite matrix. The changes in the Young's moduli are reported both as a function of mean crack separation and in the form of a stress-versus-strain curve. The program also calculates the critical strain for delamination growth and predicts the strain at which a quarter-inch diameter delaminated area will buckle. The stress-versus-strain predictions have been compared to experiment for two test structures, and good agreement has been found in each case.

INTRODUCTION

The use of composite laminates for a variety of applications has increased steadily over the last decade. The aerospace industry, in particular, is interested in these materials because of the high strength-to-weight ratios they can provide. As the use of laminates becomes more prevalent in space applications at NASA, an understanding of how these materials *fail* becomes critically important. The ability to predict the initiation and development of damage in the laminate would be a useful tool, both during the design process and for reliability estimates once the laminate is in service. Though much work has been done in this area, both experimental and theoretical, there is still very little software available which translates that research into useable design tools for laminates. The work presented herein is a first step toward filling that niche.

LAMDGRAD, the computer program developed with this goal in mind, is designed specifically to be used with the Nastran™ data deck produced by I-Deas™, one of the primary computer aided design programs used in the Structures and Mechanics Division at Johnson Space Center. The program predicts the tensile stress at which the laminate first exhibits non-linear materials behavior (corresponding to the point at which the matrix material first cracks) and predicts the elastic properties for the laminate as damage develops. In addition, the program predicts the compressive strain at which a 1/4 inch diameter delamination will buckle, and, when supplied with the critical strain energy release rate (presumably determined from experiment), the program also calculates the critical strain for delamination growth.

THEORY

The theoretical analysis used for predicting matrix damage development and the resulting elastic properties in LAMDGRAD is almost entirely from the work of Allen and Lee [1]. The analysis used for prediction of delamination growth and buckling is the work of Flanagan [2]. The general laminate theory used for both is due to Nettles [3].

Allen and Lee use an internal state variable (ISV) approach to model matrix crack development. The damage of a matrix crack is averaged over a volume element, the ISV then reflects the damage state of that volume element. Under a tensile load in the 0° direction, the matrix material in the 90° plies is assumed to crack when the average stress in the those plies is equal to the transverse failure strength of the composite. The upshot is that the constitutive equation for the damaged plies is modified. The constitutive equation for the undamaged ply is given by

$$\begin{bmatrix} \bar{\sigma}_L \\ \bar{\sigma}_T \\ \bar{\sigma}_{LT} \end{bmatrix} = \begin{bmatrix} Q_L & Q_{LT} & 0 \\ Q_{LT} & Q_T & 0 \\ 0 & 0 & G_{LT} \end{bmatrix} \begin{bmatrix} \bar{\epsilon}_L \\ \bar{\epsilon}_T \\ \bar{\epsilon}_{LT} \end{bmatrix}$$

where the $\bar{\sigma}$'s and the $\bar{\epsilon}$'s are the volume averaged stresses and strains, respectively. The Q matrix is the plane stress stiffness tensor; with shear modulus G . The subscripts L and T denote longitudinal (parallel to the primary material axis) and transverse (normal to the primary material axis), respectively.

The constitutive equation of the damaged ply is then modified to be

$$\begin{bmatrix} \bar{\sigma}_L \\ \bar{\sigma}_T \\ \bar{\sigma}_{LT} \end{bmatrix} = \begin{bmatrix} Q_L(1 - \nu_{LT}\nu_{TL}j) & Q_{LT}(1 - j) & 0 \\ Q_{LT}(1 - j) & Q_T(1 - j) & 0 \\ 0 & 0 & G_{LT}(1 - \phi) \end{bmatrix} \begin{bmatrix} \bar{\epsilon}_L \\ \bar{\epsilon}_T \\ \bar{\epsilon}_{LT} \end{bmatrix}$$

where the damage parameters j and ϕ depend *only* on the ratio of the mean crack separation to the thickness of the ply, as follows[1]:

$$j = \frac{\lambda C_T (1 - \nu_T)(1 - \nu_T - 2\nu_{LT}\nu_{TL})}{(1 - \nu_{LT}\nu_{TL})^2 - \lambda C_T (\nu_T + \nu_{LT}\nu_{TL})^2}$$

where

$$\lambda C_T = \frac{16}{\pi^3} \sum_{n=1}^{\infty} \frac{\tanh\left[\frac{(2n-1)\pi a}{2t} \sqrt{G_T/C_T}\right]}{(2n-1)^3 \frac{a}{t} \sqrt{G_T/C_T}}$$

and

$$\phi = \frac{16}{\pi^3} \sum_{n=1}^{\infty} \frac{\tanh\left[\frac{(2n-1)\pi a}{2t}\right]}{(2n-1)^3 \frac{a}{t}}$$

where a is the mean crack separation, t is the ply thickness, G_T is the transverse shear modulus, and C_T is the transverse component of the 3d stiffness tensor.

Once the Q matrix of each ply is determined, the membrane matrices A , B , and D , of the total laminate can be calculated according to standard laminate theory [3] and the degraded elastic moduli of the laminate can be determined. Furthermore, by inverting the A matrix and setting the applied stress equal to the transverse failure strength of the weakest 90°, or near 90°, plies, the strain at which the matrix first cracks (and hence the materials properties become nonlinear) may be determined. The strains at which additional cracking occurs are determined in a similar fashion, and the full stress-versus-

strain curve developed. When the applied stress is greater than what can be supported by the 0° plies alone, the laminate is assumed to fail.

For the delamination buckling or growth calculations, the delaminated area is treated as a clamped, elliptical plate with enforced-edge displacements. The formulas resulting from the single-term Rayleigh-Ritz technique are too ugly to summarize here, and can be found in full gory detail in [2]. Several of the assumption, however, warrant comment. First, it is assumed that the delaminated layer is thin compared to the parent laminate. Secondly, the elastic properties of the parent layer are assumed to be the same as the undamaged laminate. Thirdly, the shape of the ellipse is assumed to remain constant.

IMPLEMENTATION AND RESULTS

The above theories are cast into code with some very minor modifications. First, though Allen and Lee's work assumes that only the 90° plies are degraded, I assume that any ply within 45° of the 90° plies are degraded. (Allen and Lee considered only $(0^\circ_q, 90^\circ_r)$ lay-ups.) I have also generalized their results so that any stacking sequence can be used, including cross-ply at any angle. None the less, unusual lay-ups will give unusual results. The program uses the plies nearest to 90° as the source for the transverse failure strength and the plies nearest to 0° as the source for the longitudinal failure strength. If there are *no* plies near 0° or 90° (that is, within 45° of those angles), the program defaults to strengths which will most likely be inappropriate. The program also does not correct the respective failure strengths if they are determined from non- 0° or non- 90° plies. The models used in the program are not appropriate for honeycomb structures.

In coding the delamination buckling and growth analysis, it is assumed that the delamination will grow or buckle at whichever interface gives rise to the largest predicted strain energy release rate, and hence the smallest critical strains. The software does *not* check to see if the delaminated layer is *thin* compared to the parent layer, as the theory assumes, although it will always be less than half of the thickness of the parent laminate.

The anticipated scenario is that an engineer will create the desired laminate or set of laminates in I-DeasTM and export the file to a NastranTM deck. Since LAMDGRAD is concerned only with the laminate lay-up and materials, any simple part, such as a flat plate, made of the laminate will suffice to generate the data deck needed by LAMDGRAD. LAMDGRAD will accommodate up to 40 different laminate lay-ups, each having up to 60 different layers.

The program prompts the user for the name of the data file. Using only the information provided in the NastranTM deck, the program calculates the stress-versus-

strain curves which results from matrix cracking due to stress in the x (0°) direction or, independently, the y (90°) direction.

LAMDGRAD also calculates the degraded elastic moduli E_x , E_y , the shear modulus G_{xy} , and the Poisson's ratio ν_{LT} as a function of the mean crack separation. This kind of information may be of greater importance for estimates of the reliability of a laminate which has incurred some matrix cracking damage, either in the course of manufacturing or in service.

The program also calculates the compressive strain at which a quarter-inch delaminated area will buckle. If the user further supplies the critical strain energy release rate, the program also calculates the strain at which a delamination of a specific size will grow.

The theoretical stress-versus-strain predictions made by LAMDGRAD have been compared to experiment for two different cross ply test structures. The first was an 8 ply laminate with a (0,45,-45,90)_S structure, and the second was a 16 ply laminate with a (90,0₂,-60,0,60,90,0)_S structure. Both were epoxy-carbon fiber composites. The experimental details are given in [4]. The results of the experiments for stress in the x direction are plotted with LAMDGRAD predictions in Figures 1 and 2, and for stress in the y direction in Figures 3 and 4. For both the slope (the degraded elastic modulus) and the failure stress, the agreement between prediction and experiment is fairly good.

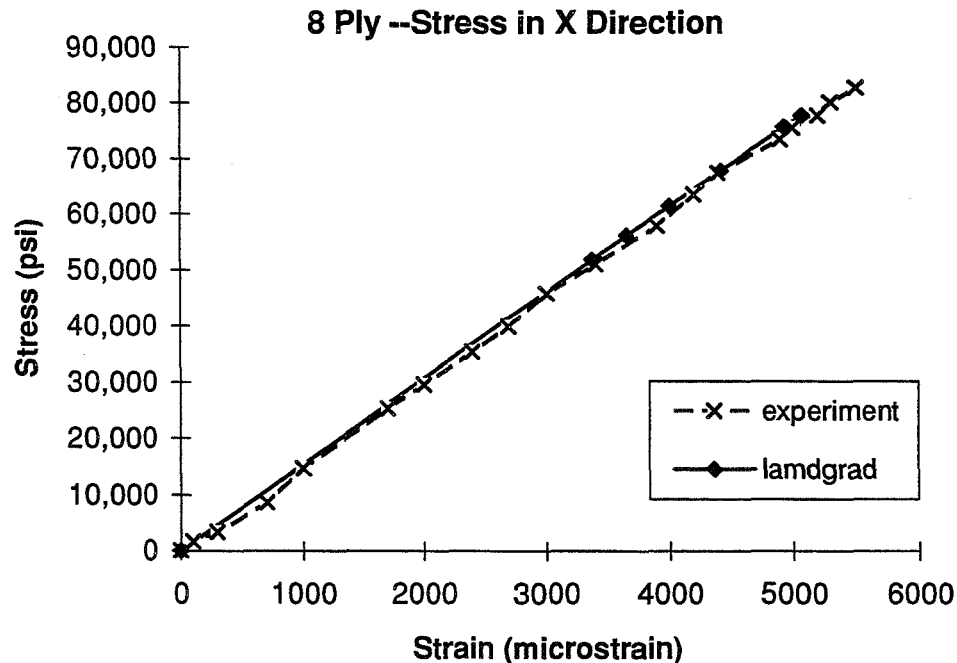


FIGURE 1

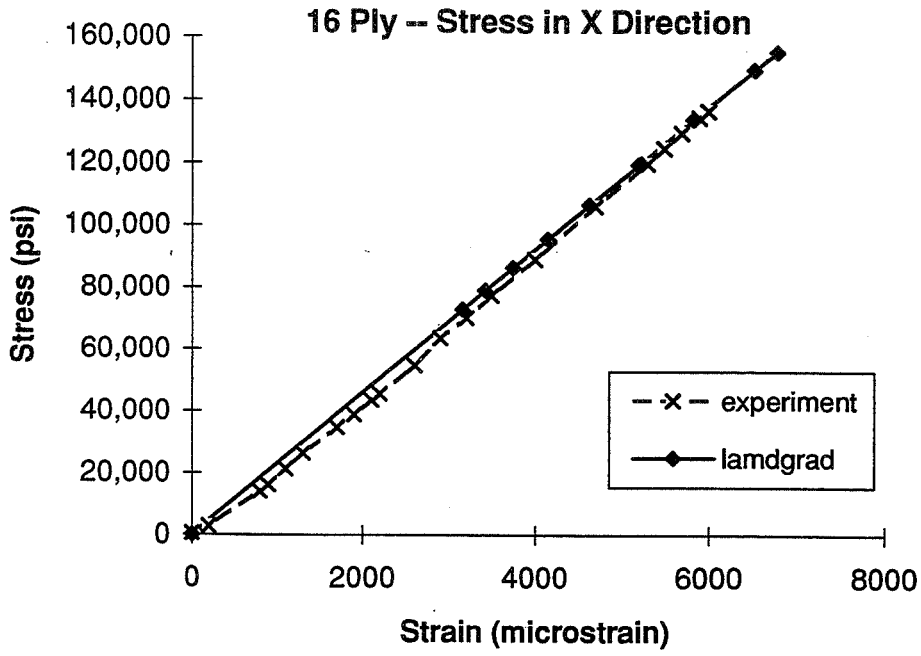


FIGURE 2

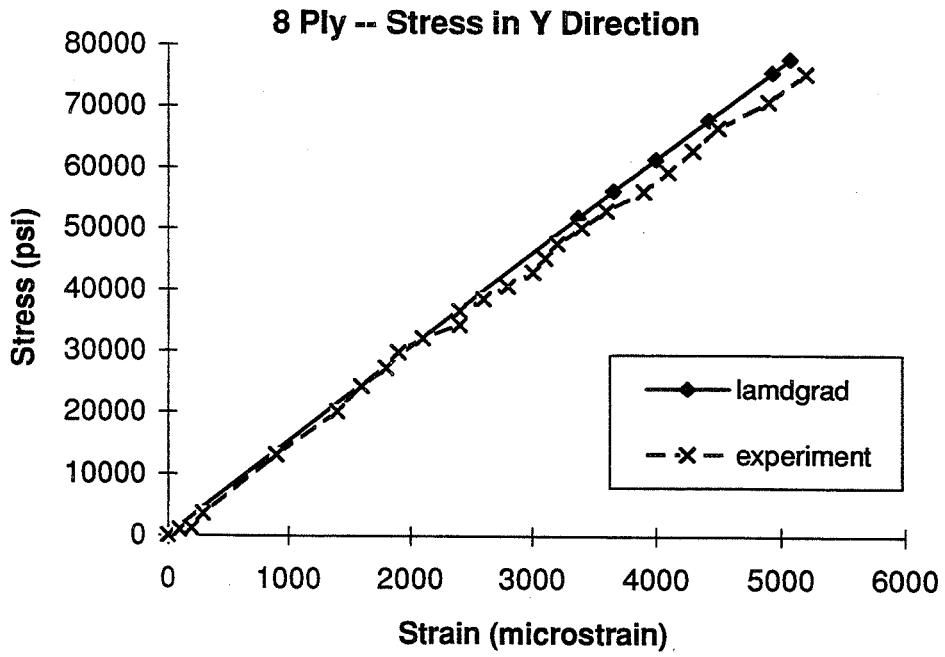


FIGURE 3

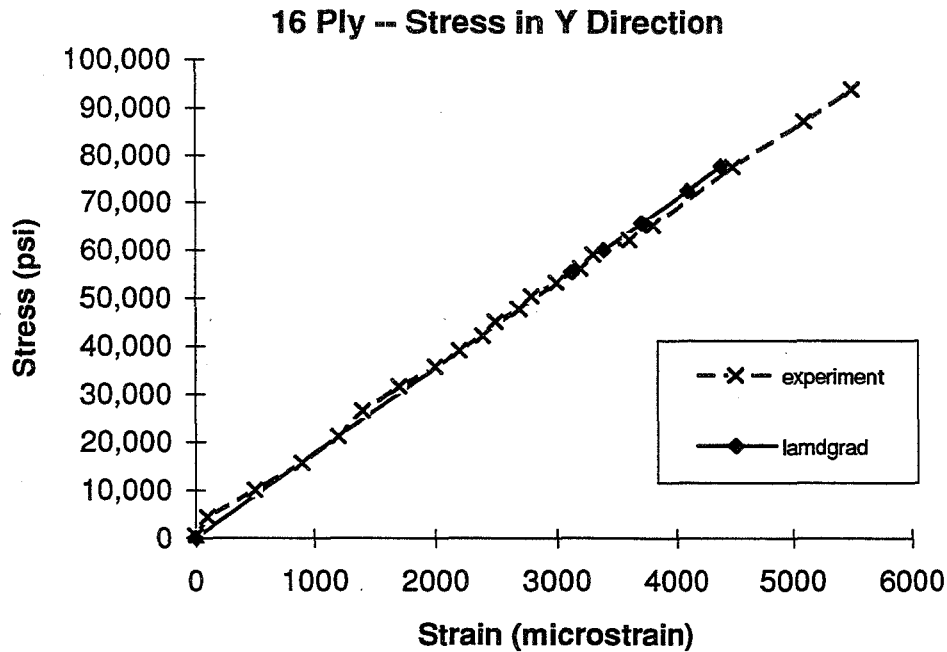


FIGURE 4

CONCLUSIONS

LAMDGRAD provides at least a small step toward laminate damage prediction tools for JSC's design engineers. And, while the program is fairly rudimentary in its scope, it seems to predict stress-versus-strain curves in reasonable agreement with experiment, at least for the structures tested. Clearly, more experimental work will have to be done to verify the buckling and delamination growth strain predictions before placing a great deal of trust in the results.

The program is admittedly limited in several regards. Most notably, the effect of delaminations is not currently included in the calculation of the stress-versus-strain curves; the only damage mode considered in that calculation is matrix cracking under tensile loads. It would be useful to be able to predict the degraded materials properties when delamination and fiber breakage are present in order to develop damage tolerant structures. Delamination and fiber breakage, especially under compressive loads, will need to be included eventually to give a complete description of the degraded materials properties. (Presumably none of the test structures had any delaminated areas so this

limitation of the program was not critical.) Furthermore, the theoretical developments followed, both for the stress-versus-strain calculation [1] and the delamination buckling and growth [2], are technically *only* appropriate for laminates made from orthotropic plies. This is not a severe restriction -- the vast majority of the ply materials used in aerospace laminates *are* orthotropic. It is a limitation, none the less. The program also assumes a monotonic load -- it does not yet address behavior under cyclic loading.

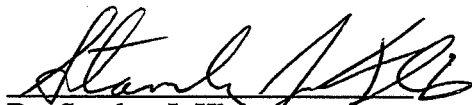
REFERENCES

- [1] David H. Allen and Jong-Won Lee, "Matrix Cracking in Laminated Composites Under Monotonic and Cyclic Loadings", in *Microcracking-Induced Damage in Composites*, eds. G.J. Dvorak and D.C. Lagoudas, AMD vol. 111 (1990) pp 65-75.
- [2] Gerry Flanagan, "Two-Dimensional Delamination Growth in Composite Laminates Under Compression Loading", *Composite Materials: Testing and Design (Eighth Conference)*, ASTM STP 972, J.D. Whitcomb, Ed., Am. Soc. for Testing and Materials, Philadelphia (1988) pp 180-190.
- [3] A.T. Nettles, *Basic Mechanics of Laminated Composite Plates*, NASA Reference Publication 1351 (1994)
- [4] Vincent Caccese, Final Report NASA/ASEE Summer Faculty Fellowship Program, Johnson Space Center (1996) pp 7-1.
- [5] MSC/NASTRAN Quick Reference Guide, version 68, Michael Reymond and Mark Miller, Eds., MacNeal-Schwendler Corp. (1994)

Bioreactor Mass Transport Studies

Dr. Stanley J. Kleis
Cynthia M. Begley
University of Houston
SD4
2 August, 1996

Dr. Neal Pellis, JSC Colleague
Biomedical Operations and Research Branch
Medical Sciences Division
Space and Life Sciences Directorate


Dr. Stanley J. Kleis


Dr. Neal Pellis


Cynthia M. Begley

BIOREACTOR MASS TRANSPORT STUDIES

Final Report

NASA/ASEE Summer Faculty Fellowship Program- 1996

Johnson Space Center

Prepared By:	Stanley J. Kleis, Ph.D. Cynthia Begley, M.S.
Academic Rank:	Associate Professor Research Assistant
University and Department:	University of Houston Department of Mechanical Engineering Houston, TX 77204-4792
NASA/JSC	
Directorate:	Space and Life Sciences
Division:	Medical Sciences
Branch:	Biomedical Operations and Research
JSC Colleague:	Neal R. Pellis, Ph.D.
Date Submitted:	August 2, 1996
Contract Number:	NAG 9-867

ABSTRACT

The objectives of the proposed research efforts were to develop both a simulation tool and a series of experiments to provide a quantitative assessment of mass transport in the NASA rotating wall perfused vessel (RWPV) bioreactor to be flown on EDU#2. This effort consisted of a literature review of bioreactor mass transport studies, the extension of an existing scalar transport computer simulation to include production and utilization of the scalar, and the evaluation of experimental techniques for determining mass transport in these vessels.

Since mass transport at the cell surface is determined primarily by the relative motion of the cell assemblage and the surrounding fluid, a detailed assessment of the relative motion was conducted. Results of the simulations of the motion of spheres in the RWPV under microgravity conditions are compared with flight data from EDU#1 flown on STS-70.

The mass transport across the cell membrane depends upon the environment, the cell type, and the biological state of the cell. Results from a literature review of cell requirements of several scalars are presented. As a first approximation, a model with a uniform spatial distribution of utilization or production was developed and results from these simulations are presented.

There were two candidate processes considered for the experimental mass transport evaluations. The first was to measure the dissolution rate of solid or gel beads. The second was to measure the induced fluorescence of beads as a stimulant (for example hydrogen peroxide) is infused into the vessel. Either technique would use video taped images of the process for recording the quantitative results. Results of preliminary tests of these techniques are discussed.

INTRODUCTION

The bioreactor development team at NASA/JSC is responsible for the development of a complete cell cultivation system capable of growing and maintaining anchorage dependent cells in a microgravity environment for extended periods of time. The bioreactor system provides control of many parameters required for the successful cell culture while suspending the cells in a fluid environment that allows three dimensional assembly. The present report will address only the fluid dynamics and mass transport within the culture vessel.

The current bioreactor vessel design is based in part on the viscous pump reactor vessel developed jointly by NASA/JSC and Dr. S. Kleis of the Turbulent Shear Flow Laboratory (TSFL), University of Houston [1]. The basic elements of the vessel are shown in Figure 1. A three dimensional flow field is established by rotating the outer cylindrical vessel wall and the inner cylindrical spin filter at different rates. The disc near one end of the spin-filter acts as a viscous pump to establish a three dimensional flow pattern within the vessel. Fluid enters the vessel from the external flow loop, in the gap between the vessel end and the disc. It then circulates within the vessel before being extracted through the porous spin filter.

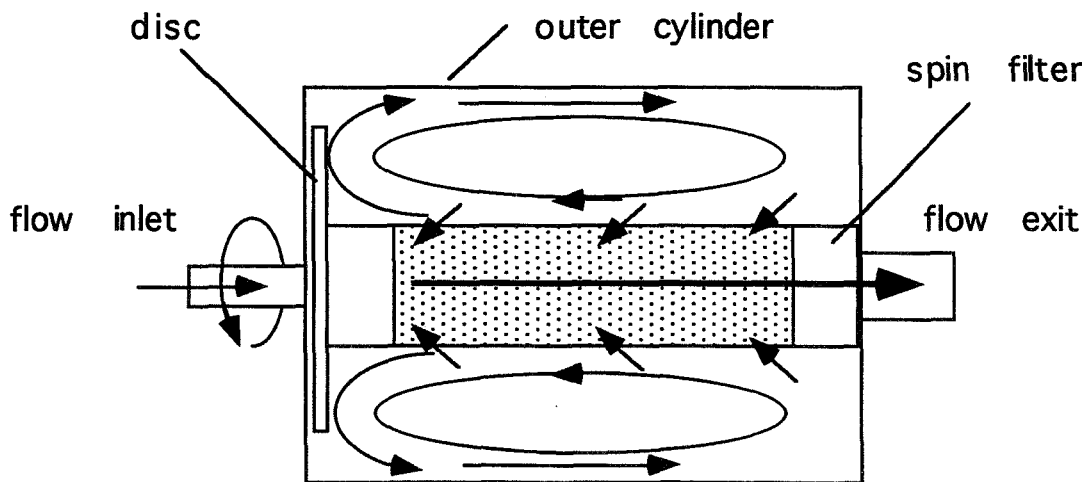


Figure 1.- Bioreactor Flow Fields Elements.

As part of the development of the current vessel design, a numerical model of the flow field within the vessel was developed [2]. The model has previously been verified under a wide range of operating conditions in a unit gravity environment by extensive measurements of the velocity fields and flow visualizations at TSFL.

An accurate model of the fluid flow field is required to be able to predict mass transport within the vessel. A mass transport model is necessary so that the effects of changes in the cell hydrodynamic environment can be separated from direct microgravity effects on cells. In the presence of body forces, density differences between the cells attached to micro carriers and the fluid medium cause relative motions, resulting in both mechanical shear and increased mass transport. In the microgravity environment, buoyancy effects are greatly reduced; the normal earth gravity is replaced by centripetal acceleration as the dominant body force. For a typical rotation rate of 2 rev/min in a 5 cm diameter vessel, the magnitude of the body force is reduced to approximately 0.001 m/s^2 compared with gravitational acceleration of 9.8 m/s^2 on earth. In the absence of other factors, cells would go from a convection dominated mass transport regime on earth to a diffusion dominated regime in microgravity. The viscous pump bioreactor vessel was designed to provide a steady three dimensional flow field with controllable rates of shear. This allows the establishment of local velocity gradients within the flow field. The local shear flow about the cells can provide control over the mass transfer rates. It is expected that, for most cell types, the shear rates required for adequate mass transport is well below the shear rates that causes damage to the cells by mechanical stress. In fact, it is expected that the shear rates for good mass transport are much lower than the stresses due to cells on microcarriers falling at terminal velocity in earth's gravity. If these characteristics are demonstrated, the bioreactor can be used to study the effects of controlled stress levels on cell function as well as to provide a low stress environment for studies of direct gravity effects on cells. One of the results of the EDU#1 experiments aboard STS-70 was an obvious change in the structure of cell assemblages cultivated in the vessel under microgravity conditions. The formation of very large structures is certainly a result of the lower mechanical stresses.

The success of the cell culture experiments aboard STS-70 demonstrate the ability of the bioreactor system to provide a well

controlled environment with adequate mass transport when operated at the relatively high rotation rates used in the experiments. The stress levels in the vessel can be reduced further by reducing the differential rotation rates of the inner and outer vessel walls. However, at some point, the secondary flow driven by the differential rotations will become so slow that the mass transport will become diffusion limited. It is likely that at these conditions, the mass transport will be insufficient to maintain a healthy cell population for most cell types. Cell types for which this is not a problem could be cultivated in static cultures.

The purpose of the present investigation was to establish a simulation of the mass transport within the vessel to be able to predict, for given cell requirements of scalar transport (oxygen, carbon dioxide, nutrients, products, etc.), the scalar concentration distributions within the vessel for given operating conditions. This would allow the prediction of the correct operating conditions or limits of operation for the vessel to avoid cell stress due to poor environmental factors.

MASS TRANSPORT PREDICTIONS

The prediction of mass transport at the cellular level within the vessel can be separated into four parts. It is first necessary to know the cell utilization or production rates of the scalar. Second, concentration distributions of the scalar quantities in the fluid phase determine the local environment for the cell. Third, it is necessary to know the details of the concentration gradients in the fluid at the cell surface. Finally, the concentration gradients at the cell surface depend upon the local scalar concentration and the relative motion of the cells to the surrounding fluid. Thus, the trajectory of the cell assemblages within the fluid must be known. It will be assumed for the present studies that the process of mass transport can be separated into these individual stages, however, the process is in general interdependent with the cell utilization or production rates depending upon many factors including the concentration itself.

During the period of the 1996 ASEE Summer Faculty Fellowship Program, these various aspects of the problem were addressed. A literature search to address the question of appropriate cell utilization models was conducted. Modifications were made to

include scalar production or utilization in some existing programs to solve for the scalar concentration distributions in the fluid phase. A program to accurately predict particle trajectories within the vessel was completed. And, the possible use of chemiluminescent dyes as indicators of mass transport for future studies was investigated.

LITERATURE SURVEY

An extensive literature search including over 170 papers was performed. Only the most applicable papers are included here. A complete list is available upon request.

Determination of mass transport in ground based bioreactors is difficult. Several models have been suggested based on turbulence and power input (most commonly variations on Harriot's slip velocity theory [3] and Kolmogoroff's theory) which have yielded wide ranges of results [4, 5, 6, 7]. These models cannot be directly related to the laminar flow conditions encountered in the microgravity bioreactor. Cell mass transport models [8, 9, 10, 11] are generally based on measurements of inflow and outflow concentrations which are used in mass balances to determine cell utilization or uptake rates. These are then divided by total cell populations to get an uptake rate per cell. This approach assumes that the cells are experiencing the same concentrations of scalars throughout the bioreactor (perfect mixing) and that cells are all the same size and will utilize the same amounts of metabolite (oxygen, glucose, etc.) regardless of how they are attached, aggregated, or differentiated. This is not the case in the microgravity bioreactor.

The bulk of the literature on oxygen transport in bioreactors concentrates on the gas-liquid transfer through sparging or surface aeration with mechanical agitation. The volumetric mass transfer coefficient, $k_L a$, for dissolving the oxygen into the medium is determined experimentally and is dependent on the type of bioreactor, aeration method, and type of medium/cells. The cellular oxygen uptake rate is then directly related to the volumetric transfer coefficient. This approach assumes perfect mixing and uniform cell size and uptake. It also assumes that all cells are in the same state (growth, maintenance, etc.). For the perfused microgravity bioreactor which has no head space or sparging, this method corresponds to measuring the dissolved oxygen in the fresh

medium and in the extracted medium and using the difference averaged over the total cell population in the bioreactor to determine the uptake rate per cell (or per ml). This kind of per cell uptake number may be a good approximation for microbial suspensions but probably breaks down in the presence of the wide variety of sizes of aggregates and level of differentiation found with mammalian cells in this bioreactor.

Riley et al [12] developed a correlation for effective diffusivities for cells in immobilized systems including the case of cells grown inside alginate or gel beads which are in a suspension culture. This method may provide insight into how to predict the effective diffusivity of differentiated mammalian cell aggregates grown on microcarriers in the microgravity bioreactor. However, ultimately the concentration distribution equation relies on knowing the rate of metabolite consumption by the cells. More recent work in this area by Glacken et al [13, 14] is promising.

SCALAR TRANSPORT SIMULATION

The current scalar transport model determines the bulk flow concentration distribution in the bioreactor (rather than assuming perfect mixing) based on the velocity profile. A detailed description of the bulk flow computations can be found in Freitas [15]. A source term has been added to include the rate of cellular utilization/production of the scalar of interest. The model was tested with a constant uniform oxygen uptake rate with a value typical of those for mammalian cell cultures found in the literature [16, 17], however nonuniform and time varying uptake rates can also be handled.

The challenge which remains is to combine the scalar concentration model with a cell utilization model that is based on true per cell uptake as opposed to an averaged cellular uptake or production. Uptake rates must include a model of growth kinetics. This model must also be combined with the bead/cell trajectory model to determine which areas of the bioreactor, and therefore which concentration gradients, the different sized cell structures will experience.

Output from the program includes the concentration profile at any given time which can be graphically displayed with the streamlines and bead/particle trajectories overlaid. The model can

also provide a histogram that shows time required for various percentages of the bioreactor volume to reach the desired saturation level as well as a measure of the percent of cells that are not receiving their desired nutrient concentration level. Concentration of the scalar in the media extracted from the spin filter can also be predicted.

Typical results showing the effects of oxygen utilization on the time for oxygen distribution in the vessel are shown in Figure 2. The uniform oxygen uptake rate of 5×10^{-9} g/cc/s is based upon a 1.0×10^6 cell/ml mammalian cell culture density. The case of 10 rpm spin filter and disc rotation, 1 rpm outer wall rotation, 5 cc/min perfusion rate was used as typical of the conditions which will be run on EDU#2. As expected, Figure 2 shows that it takes longer for the perfused oxygen to reach the 10% saturation level with cells present.

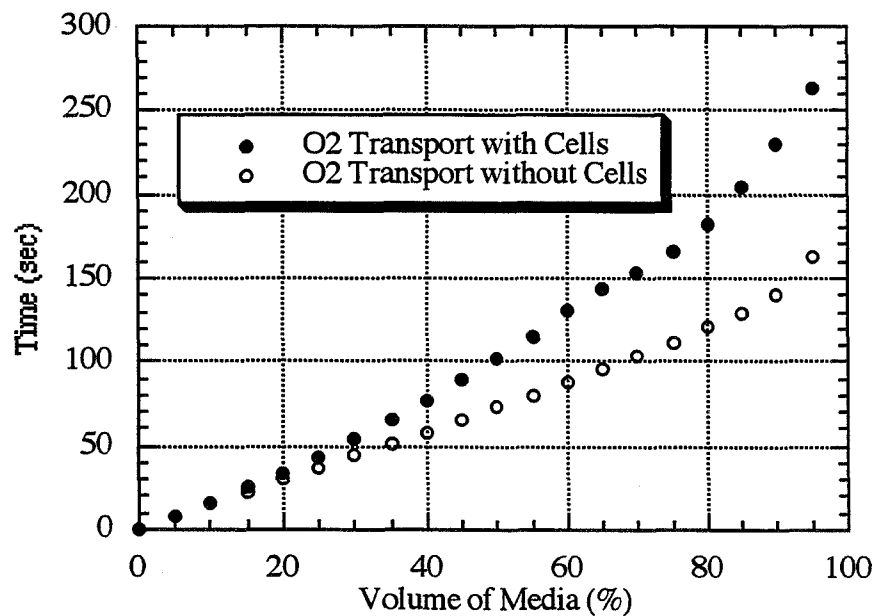


Figure 2.- Time required to reach 10% of the perfused oxygen concentration given a 5% initial concentration in the bioreactor vessel.

In Figure 3, the extracted media oxygen concentration is plotted versus time. It takes on the order of 150 seconds for an appreciable change in the exit oxygen concentration to occur. Note

that, in the case with cells present, the cells consume all of the available oxygen in the outlet flow region before the perfused oxygen begins to reach that area.

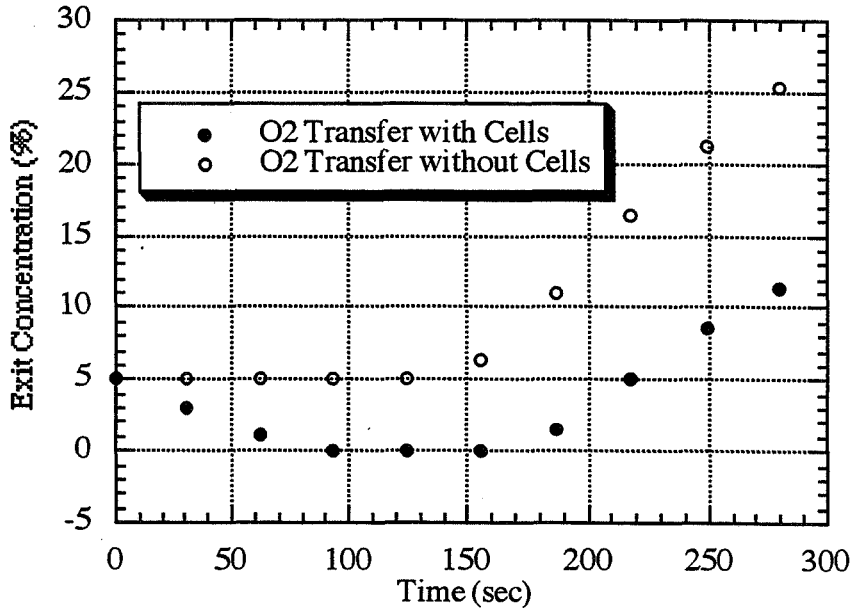


Figure 3.- Spin filter extraction concentration as a percent of inlet concentration given a 5% initial concentration in the bioreactor vessel.

PARTICLE POSITION ESTIMATES

The bead trajectory simulations provide both the position time history and the relative motion of the bead and fluid. As described above, both pieces of information are required for predicting mass transport. Details of the study of the motion of a sphere in the bioreactor can be found in Robeck [18]. A summary of the equation development and some typical results are given below.

Bead positions are estimated from force balances on the beads in the velocity fields computed for the prescribed operating conditions. The general force balance equation for a sphere in an unsteady, non uniform flow field is given by Maxey and Riley [19],

$$m_p \frac{dV_i}{dt} = (m_p - m_f)g_i + m_f \left. \frac{Du_i}{Dt} \right|_{Y(t)} - \frac{1}{2} m_f \frac{d}{dt} \left\{ V_i(t) - u_i[Y(t), t] - \frac{1}{10} a^2 \nabla^2 u_i \right\}_{Y(t)}$$

$$-6\pi a\mu \left\{ V_i(t) - u_i[Y(t), t] - \frac{1}{6} a^2 \nabla^2 u_i|_{Y(t)} \right\} - 6\pi a^2 \mu \int_0^t \frac{\left(\frac{d}{dt} \left\{ V_i(\tau) - u_i[Y(\tau), \tau] - \frac{1}{6} a^2 \nabla^2 u_i|_{Y(\tau)} \right\} \right)}{[\pi\nu(t-\tau)]^{1/2}} d\tau,$$

where m_p is the mass of the particle, m_f is the mass of fluid displaced by the sphere, a is the sphere radius, V_i is the i th sphere velocity component, u_i is the corresponding fluid velocity component evaluated at the current sphere position and time, and μ is the fluid viscosity. The last term is the Basset history integral term, which accounts for the transient decay of the initial conditions and the disturbance of the fluid by the relative motion of the sphere.

Due to the low Reynolds number limitation on their equation, Maxey and Riley did not include a lift force in their equation. Thus, the first modification to the equation was to add a term for the lift force. The expression used for the lift was taken from a derivation for the force on a sphere in an inviscid, nonuniform, rotational flow (Auton, et. al. [20]). Although the flow in the bioreactor is certainly not inviscid, it has been assumed that the inviscid lift will be a good approximation to the actual side force acting on the sphere. The lift term is

$$F_L = m_f C_L (u - V) \times \omega.$$

C_L is the lift coefficient, which is 1/2 for a sphere, and ω is the fluid vorticity. The other quantities are as described above. Saffman [21] derived the lift force due to shear in a viscous flow, however, this contribution was estimated from the simulated results to be much smaller in magnitude and has been neglected.

The evaluation of the Basset integral is difficult due to the poor convergence at long times. This problem has been addressed in some recent studies which also extend the Reynolds number range to which the equations apply. Lovalenti and Brady [22] derived an equation for motion at small but finite Reynolds number. This equation contains a term which they refer to as an unsteady Oseen correction, which is essentially a history effect corrected for higher Reynolds number. The derivation of the equation was performed using the assumption of an unsteady, uniform flow field. The bioreactor flow field is not uniform, but the term is taken to be a first approximation to what the actual history force would be in a

nonuniform field. The unsteady Oseen force includes history effects from components of the force parallel and perpendicular to the direction of motion. The perpendicular component is considered to be a higher order correction and is not attempted in the current model. The unsteady Oseen term, as included in the model is then

$$F_{Os}(t) = \frac{3}{8} \left(\frac{ReSl}{\pi} \right)^{\frac{1}{2}} \left\{ \int_0^t \left[\frac{2}{3} F_s(t) - G(A) F_s(\tau) \right] \frac{2d\tau}{(t-\tau)^{\frac{3}{2}}} \right\}.$$

Re is the Reynolds number based on particle radius and relative velocity, $(V-u)*2a/\nu$; Sl is the Strouhal number, which is $a/(tc*uc)$, where tc and uc are the characteristic time and velocity for the flow field. F_s is the Stokes drag force, and τ is again a time variable of integration. The function G(A) and the variable A are defined by:

$$G(A) = \frac{1}{|A|^2} \left(\frac{\frac{1}{\pi^2} \operatorname{erf}(|A|) - \exp(-|A|^2)}{2|A|} \right),$$

$$A(t, \tau) = \frac{Re}{2} \left(\frac{t-\tau}{ReSl} \right)^{\frac{1}{2}} \left(\frac{X(t) - X(\tau)}{t-\tau} \right).$$

In the equation for A, $X(t)-X(\tau)$ is the integrated particle displacement relative to the fluid in the direction in question.

After modification with these corrections, the equation of motion for a small spherical particle in an unsteady, nonuniform flow at low Reynolds number is

$$\begin{aligned} m_p \frac{dV_i}{dt} = & (m_p - m_f) g_i + m_f \frac{Du_i}{Dt} \Big|_{Y(t)} - \frac{1}{2} m_f \frac{d}{dt} \left\{ V_i(t) - u_i[Y(t), t] - \frac{1}{10} a^2 \nabla^2 u_i \Big|_{Y(t)} \right\} \\ & - 6\pi a \mu (1 + .375 Re) \left\{ V_i(t) - u_i[Y(t), t] - \frac{1}{6} a^2 \nabla^2 u_i \Big|_{Y(t)} \right\} + m_f C_L (u_i - V_i) \times \omega_i \\ & + \frac{3}{8} \left(\frac{ReSl}{\pi} \right)^{\frac{1}{2}} \left\{ \int_0^t \left[\frac{2}{3} (1 + .375 Re) F_s(t) - G(A) (1 + 375 Re) F_s(\tau) \right] \frac{2d\tau}{(t-\tau)^{\frac{3}{2}}} \right\}. \end{aligned}$$

The term $0.375*Re$ is the steady Oseen correction to the Stoke's drag, F_s .

These equations were solved using a fourth order Runge-Kutta method for the position coordinates as functions of time using the fluid velocities computed by a previous numerical model for steady fluid motion.

The inclusion of the lift and unsteady Oseen correction obviously complicates the equations and greatly increases the computation time. Several test cases were run to see how significant each of these terms was in determining the particle trajectories. The results (see Robeck, [18]) show significant changes in particle trajectory due to both terms, thus the complete equation must be used for estimates of particle trajectories in the bioreactor operating in a microgravity situation.

The only data which will be presented here compares output from the model with information from videotaped images from actual space flight of the bioreactor vessel taken on STS-70. Detailed position data for the 3.175mm acetate bead is difficult to obtain from the video tapes due to optical distortions and the high density of cellular matter left in the vessel after the cell experiments. One thing that can be determined to a good degree of accuracy is the time it takes for a bead to make one complete trip around the vessel in the theta direction. One needs only to note the times at which the particle passes directly in front of the spin filter to get this information. This can be compared with predicted times from the simulation to help assess the validity of the model.

Figure 4 shows this comparison for the case with 5 rpm inner cylinder rotation rate, 1 rpm outer vessel rotation rate, and 10 ml/min. perfusion. The solid line represents the angular position found using the computer program. The program wraps the data so that theta only goes between zero and 2π , but this has been undone, so the solid line is total number of radians traveled. The symbols represent actual times from the flight data that the bead passed in front of the spin filter. Since the theta choice is fairly arbitrary, that is, there is nothing special about any particular angle, the data were synchronized in the following way. There was a gap in the time data from the videotape, because at one point the bead moved beyond the range of axial position that could be seen in the videotape. This was assumed to correspond to the theta when the position was at its lowest z point from the model. The z data has been plotted in a dashed line to show this. The z value is actually

the dimensionless z times ten, done so the variable would be visible when plotted on the same scale as the theta.

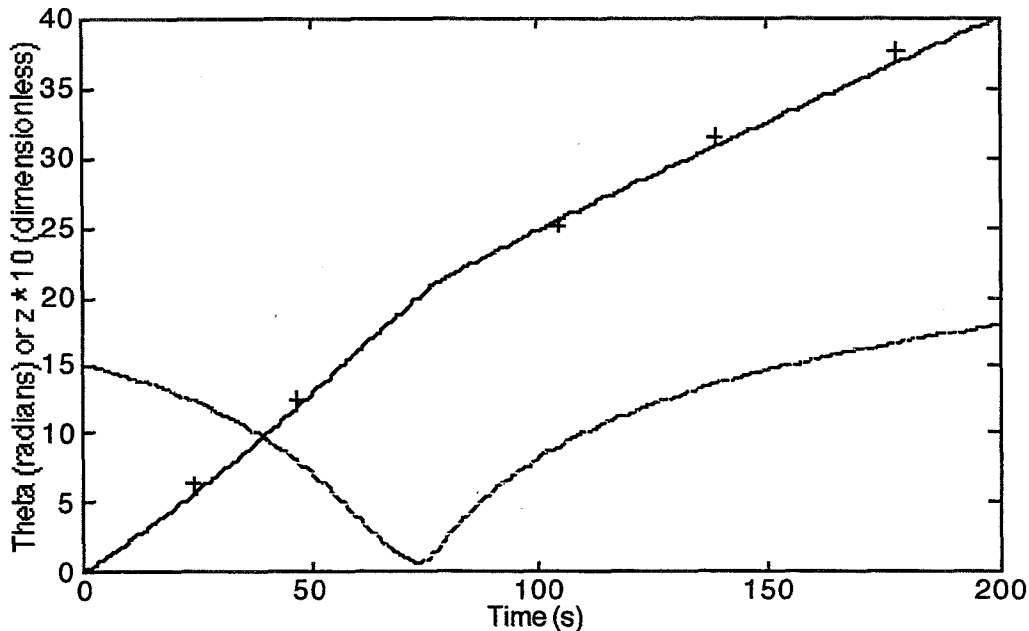


Figure 4.- Theta vs. Time from Model vs. Flight Data Points (5 rpm inner, 1 rpm outer, 5 ml/min. Perfusion)

The agreement between modeled and actual circulation times is extremely good. This not only indicates that the theta component equation is a good model, but the r and z equations as well, since the velocity in the theta direction is highly dependent upon the position of the particle in the (r,z) plane. The results of these and other comparisons show that the complete model is required to produce accurate predictions of particle trajectories. For a more detailed comparison and discussion see Robeck [18].

EXPERIMENTAL TECHNIQUE DEVELOPMENT

One of the goals of this study was to evaluate two possible experimental techniques with the hope that they could be used on EDU#2 to provide a data base of flight data to test the mass transport models. The first technique used dissolving spheres, where the sphere diameter could be recorded and used to infer the

mass transfer at the cell surface (phase change). Commercially available cake decorations were obtained and tested for dissolution rate. It was found that these spheres of approximately 3mm would dissolve in vigorously stirred water in about 2 minutes. Further tests in a free suspension are difficult due to the rapid settling velocity in earth's gravity. Tests could be conducted by supporting the spheres in the fluid phase. The main difficulty in using this method for EDU#2 is the requirement of keeping the beads out of the fluid until the test begins and then inserting them into the fluid.

The second technique considered was the use of a chemiluminescent dye bound in Ca-alginate beads, which could be activated by infusing a stimulant into the vessel [23, 24, 25, 26, 27]. This study is not yet complete, but preliminary results are encouraging. The main advantage of this approach is the ability to control the reaction by the infusion of reactant. It is also attractive because the reaction is an oxygen transport problem and the diffusion characteristics of Ca-alginate are known.

CONCLUSIONS

A great deal of progress has been made toward the accurate prediction of mass transport within the RWPV bioreactor.

1. Simulation programs for the transport of a scalar within the vessel have been written and tested for simple utilization situations.
2. A literature survey has been completed, providing some information on cell utilization and production for various quantities.
3. An accurate bead trajectory simulation for the motion of a sphere in the bioreactor has been completed and tested against actual flight data, with excellent results.
4. Preliminary tests on experimental techniques for measuring mass transport on EDU#2 are encouraging. Further development is required.

REFERENCES

- [1] Kleis, S. J., Schreck, S., and Nerem, R. M., "A Viscous Pump Bioreactor", *Biotechnology and Bioengineering*, Vol. 36, pp. 771-777, 1990.
- [2] Abdallah, A. K., "Numerical Simulation of the Viscous-Pump-Bioreactor Flow", Masters Thesis, University of Houston, 1989.
- [3] Harriott, P., "Mass Transfer to Particles: Part 1. Suspended in Agitated Tanks", *A.I.Ch.E. Journal*, Vol. 8, No. 1, pp. 93-102, 1962.
- [4] Nienow, A. W., "Dissolution Mass Transfer in a Turbine Agitated Baffled Vessel", *The Canadian Journal of Chemical Engineering*, Vol. 47, pp. 248-258, 1969.
- [5] Sano, Y., Yamaguchi, N., and Adachi, T., "Mass Transfer Coefficients for Suspended Particles in Agitated Vessels and Bubble Columns", *Journal of Chemical Engineering of Japan*, Vol. 7, No. 4, pp. 255-261, 1974.
- [6] Nienow, A. W., "Agitated Vessel Particle-Liquid Mass Transfer: A Comparison between Theories and Data", *The Chemical Engineering Journal*, Vol. 9, pp. 153-160, 1975.
- [7] Bello, R. A., Robinson, C. W., and Moo-Young, M., "Gas Holdup and Overall Volumetric Oxygen Transfer Coefficient in Airlift Contactors", *Biotechnology and Bioengineering*, Vol. XXVII, pp. 369-381, 1985.
- [8] Lavery, M. and Nienow, A. W., "Oxygen Transfer in Animal Cell Culture Medium ", *Biotechnology and Bioengineering*, Vol. XXX, pp. 368-373, 1987.
- [9] Dorresteyn, R. C., Numan, K. H., De Gooijer, C. D., and Tramper, J., "On-Line Estimation of the Biomass Activity During Animal-Cell Cultivations", *Biotechnology and Bioengineering*, Vol. 50, pp. 206-214, 1996.

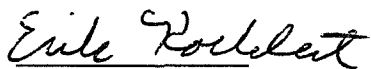
- [10] Zeng, A.-P., "Mathematical Modeling and Analysis of Monoclonal Antibody Production by Hybridoma Cells", *Biotechnology and Bioengineering*, Vol. 50, pp. 238-247, 1996.
- [11] Miller, R. and Melick, M., "Modeling Bioreactors ", *Chemical Engineering*, pp. 112-120, 1987.
- [12] Riley, M. R., Muzzio, F. J., Buettner, H. M., and Reyes, S. C., "A Simple Correlation for Predicting Effective Diffusivities in Immobilized Cell Systems", *Biotechnology and Bioengineering*, Vol. 49, pp. 223-227, 1996.
- [13] Glacken, M. W., Adema, E., and Sinskey, A. J., "Mathematical Descriptions of Hybridoma Culture Kinetics: I. Initial Metabolic Rates ", *Biotechnology and Bioengineering*, Vol. 32, pp. 491-506, 1988.
- [14] Glacken, M. W., Adema, E., and Sinskey, A. J., "Mathematical Descriptions of Hybridoma Culture Kinetics: II. The Relationship Between Thiol Chemistry and the Degradation of Serum Activity", *Biotechnology and Bioengineering*, Vol. 33, pp. 440-450, 1989.
- [15] Freitas, S., "Mass Transport in Laminar Flow Bioreactors", Masters Thesis, University of Houston, 1991.
- [16] Kargi, F. and Moo-Young, M., "Transport Phenomena in Bioprocesses", *Comprehensive Biotechnology: The Principles, Applications and Regulations of Biotechnology in Industry, Agriculture and Medicine*, Vol. 2, pp. 5-56.
- [17] Shuler M. L. and Kargi F., *Bioprocess Engineering: Basic Concepts*, Prentice Hall International Series in the Physical and Chemical Engineering Sciences, 1992.
- [18] Robeck, C. M., "Motion of a Sphere in a Space Flight Bioreactor", Undergraduate Honors Thesis, University of Houston, 1996.

- [19] Maxey, M. R. and Riley, J. J., "Equation of motion for a small rigid sphere in a nonuniform flow", *Phys. Fluids*, Vol. 26, pp. 883-889, 1983.
- [20] Auton, T. R., Hunt, J. C., and Prud'homme, M., "The force on a body in inviscid unsteady non-uniform rotational flow", *J. Fluid Mech.*, Vol. 197, pp. 241-257, 1988.
- [21] Saffman, P. G., "The lift on a small sphere in a slow shear flow", *J. Fluid Mech.*, Vol. 22, pp. 385-400, 1965.
- [22] Lovalenti, P. M. and Brady, J. F., "The hydrodynamic force on a rigid particle undergoing arbitrary time-dependent motion at small Reynolds number.", *J. Fluid Mech.*, Vol. 256, pp. 561-605, 1993.
- [23] Yappert, M. C. and Ingle, J. D. Jr., "Absorption-Corrected Spectral Studies of the Lucigenin Chemiluminescence Reaction", *Applied Spectroscopy*, Vol 43, pp. 767-771, 1989.
- [24] Uchida, T., Kanno, T., and Hosaka, S., "Direct Measurement of Phagosomal Reactive Oxygen by Luminol-Binding Microspheres", *Journal of Immunological Methods*, Vol. 77, pp. 55-61, 1985.
- [25] Faulkner, K. and Fridovich, I., "Luminol and Lucigenin as Detectors for O₂ ", *Free Radical Biology and Medicine*, Vol. 15, pp. 447-451, 1993.
- [26] Van Dyke, K., Allender, P., Wu, L., Gutierrez, J., Garcia, J., Ardekani, A., and Karo, W., "Luminol- or Lucigenin-Coated Micropolystyrene Beads, a Single Reagent to Study Opsonin-Independent Phagocytosis by Cellular Chemiluminescence: Reaction with Human Neutrophils, Monocytes, and Differentiated HL60 Cells", *Microchemical Journal*, Vol. 41, pp. 196-209, 1990.
- [27] Larena, A. and Martinez-Urreaga, J., "Solvent Effects in the Reaction of Lucigenin with Basic Hydrogen Peroxide: Chemiluminescence Spectra in Mixed Polar Solvents", *Monatshefte fur Chemie*, Vol. 122, pp. 697-704, 1991.

Developing A Graphical User Interface For The
ALSS Crop Planning Tool

Erik Koehlert
Texas A&M University
NASA mailcode: ER2
August 19, 1996
Contract Number: NAG 9-867

NASA Colleague: Jon Erickson
Intelligent Systems Branch
Automation, Robotics and Simulation Division
Engineering Directorate


Erik Koehlert


Jon Erickson

Page intentionally left blank

Abstract

The goal of my project was to create a graphical user interface for a prototype crop scheduler. The crop scheduler was developed by Dr. Jorge Leon and Laura Whitaker for the ALSS (Advanced Life Support System) program. The addition of a system-independent graphical user interface to the crop planning tool will make the application more accessible to a wider range of users and enhance its value as an analysis, design, and planning tool. My presentation will demonstrate the form and functionality of this interface.

This graphical user interface allows users to edit system parameters stored in the file system. Data on the interaction of the crew, crops, and waste processing system with the available system resources is organized and labeled. Program output, which is stored in the file system, is also presented to the user in performance-time plots and organized charts. The menu system is designed to guide the user through analysis and decision making tasks, providing some help if necessary. The Java programming language was used to develop this interface in hopes of providing portability and remote operation.

INTRODUCTION

The intelligent crop planner provides an essential tool for sustaining a crew in a closed ecological life support system. The interaction between plants and crew members must be kept in balance while meeting waste processing and space requirements. Reservoirs of oxygen, carbon dioxide, water, as well as fresh and stored edibles, must be maintained at an adequate level. Harvesting, planting, and food and waste processing activities must be scheduled to fit in with daily maintenance and research activities. The crop planning tool developed by Dr. Jorge Leon and Laura Whitaker takes all these constraints into account and helps the crew to plan a crop schedule that maximizes crew survival. A graphical user interface that allowed parameter changes and their corresponding outcomes to be viewed quickly by the crew would enhance the usability of the crop planning tool. There are three major goals that the crop planner must accomplish.

First, the graphical user interface (GUI) should provide editing and viewing capabilities for system parameters and output data contained in the file system. System parameters are stored in five files named crew.dat, crop.dat, initial.dat, waste.dat, and reservoir.dat. Output data from the scheduler and simulator are stored in files named o2.dat, co2.dat, wheat.dat, lettuce.dat, wcons.dat, wharv.dat, lcons.dat, lharv.dat. The crop planning tool uses numerical data in these files to generate a schedule, simulate the outcome, and advise on system parameter changes. When rewriting, these files must be kept in the same format so as not to interfere with operation of the crop planning tool.

Next, portability for the GUI across various computer platforms is desired. The type of system that the crop planning tool will be run on, is still under speculation at this time. Making the GUI platform independent will eliminate the need for rewriting it in another language, or recompiling it for use on another computer platform. Also, platform independence provides greater accessibility during the developmental stages of the GUI and crop planning tool.

Finally, the GUI should also allow the user to run the crop planning tool without having to exit the GUI to execute the program. The crop planner is written in ANSI C and requires that a random seed variable be sent to it to execute the program. The results of the crop planner, which are stored in the file system, should be available from within the GUI either during or after execution of the crop planning tool.

GUI DEVELOPMENT

The first step in developing the interface was to select the programming language. Portability had to be a major feature and extensive graphics capabilities were needed to have form-based input screens and output screens containing colorful charts and graphs. The Java programming language looked strong in these areas and was chosen over TCL and TK. Java provides: good platform independent graphics capabilities, a language similar to C/C++, the ability to run programs written in ANSI C or C++ (referred to as native method implementation), and the bonus of network compatibility for the possibility of remote operation. These reasons made Java a good choice for this project.

Next, the overall look of the interface was determined. The major activities conducted while working in the GUI are viewing and editing system parameters, running the crop planner program, viewing program results, getting help, and exiting the program. A toolbar at the top of the GUI should therefore display choices for these activities. While viewing and editing, system parameters should be displayed neatly on a form-based screen with editable text fields. Parameters should be labeled clearly with their name and have units designated. One form based screen per file seemed like the best method of splitting parameter data up into crew, crop, waste, initial, and reservoir categories. A "save" button allows edited values to be stored to the corresponding file for each form.

There is a large amount of numerical data generated when running the crop planning tool. Viewing program results effectively, necessitates the use of charts and graphs. Determining the success of a simulated crop schedule should be a quick process. Identifying trends and individual occurrences where system reservoir levels approach dangerous levels should be easy to accomplish. Graphs should be clearly labeled, scaled accurately, and convey the significance of data quickly to the user. Text-based output like (event occurrences or program suggestions) should be displayed in labeled, scrollable text areas.

The last step for GUI development was to find the documentation and sample programs necessary to accomplish the development goals given above. Books and on-line documentation would provide my major sources for information on Java, since the language is relatively new and few people in my area know about it.

RESULTS

The GUI's main component structure was created successfully. It allows the user to view a title screen upon entrance into the GUI. The top toolbar provides links to screens allowing form-based system parameter editing, graphing of data output, and help. The form-based editing system reads data from files into editable text areas, names and labels data accordingly, and allows edited parameters to be saved to the file system. Edited parameters are stored in the correct format for reading by the planner program. Running the planner program from within a Java-based GUI was not accomplished. The graphing module for displaying output data files is under construction.

CONCLUSIONS

The creation of a graphical user interface using Java was made difficult by the newness of the language. The language is still under construction and contains many bugs. The source code and tutorial documentation provided by Sun Microsystems (the main developer of the Java programming language) was modified almost weekly while I was doing this project. Books and other on-line resources were centered on using Java for web page applications which do not access the file system or use native method implementation.

Java's native methods are expected to change in the next release of Java, which is expected out soon. This new release is expected to take care of many of the problems attributed to implementing native methods. If this new release does not allow the planner program to be run from within the GUI, then a CGI script may provide the solution.

More work needs to be done on completing the graphing routine. Source code for a simple graphing program that inputs data from an HTML page has been found. I am using this code as a starting point to design a graphing function that provides file reading capabilities and scales automatically to accommodate greater numbers of data points.

A Comparison of Total and Intrinsic Muscle Stiffness
Among Flexors and Extensors of the Ankle, Knee, and Elbow

Sandra M. Lemoine, Ph.D.
Shenandoah University
SD3
August 14, 1996

Steven F. Siconolfi, Ph.D.
Neuromuscular Laboratory in the Neurosciences Laboratories
Life Sciences Research Laboratories
Medical Sciences Division
Space and Life Sciences Directorate


Sandra M. Lemoine, Ph.D.


Steven F. Siconolfi, Ph.D.

**A COMPARISON OF TOTAL AND INTRINSIC MUSCLE STIFFNESS
AMONG FLEXORS AND EXTENSORS OF THE ANKLE, KNEE, AND ELBOW**

**Final Report
NASA/ASEE Summer Faculty Fellowship Program-1996
Johnson Space Center**

Prepared by:	Sandra M. Lemoine, Ph.D
Academic Rank:	Associate Professor
University & Department:	Shenandoah University Kinesiology Program Winchester, VA 22601
NASA/JSC	
Directorate:	Space and Life Sciences
Division:	Medical Sciences
Branch:	Life Sciences Research Laboratories
JSC Colleague:	Steven F. Siconolfi, Ph.D.
Date Submitted:	August 14, 1996
Contract Number:	NAG 9-867

ABSTRACT

This study examined 3 methods that assessed muscle stiffness. Muscle stiffness has been quantified by tissue reactive force (transverse stiffness), vibration, and force (or torque) over displacement. Muscle stiffness also has two components: reflex (due to muscle sensor activity) and intrinsic (tonic firing of motor units, elastic nature of actin and myosin cross bridges, and connective tissue). This study compared three methods of measuring muscle stiffness of agonist-antagonist muscle pairs of the ankle, knee and elbow.

Method One

Transverse Stiffness is the stiffness recorded by pressing a tonometer into the muscle group and recording the relative tissue reactive force. A Russian designed myotonometer (a small pressure sensor pushed onto the muscle) will assess the reaction of muscles during isometric contraction at rest and at 20, 40, 60, 80, and 100% of maximum voluntary contraction (MVC).

Method Two

Intrinsic Stiffness is the stiffness when neural inputs have little or no influence on force production. Subjects will produce maximal contractions while the muscles are first lengthened and then shortened. The torque is generated from a maximal isokinetic concentric contraction produced by the subject immediately after completing a maximal isokinetic eccentric contraction with the same muscle. This post-eccentric concentric contraction has two linear components: one at and above optimal muscle length and one below this length.

Method Three

Total Stiffness is the sum of reflex and intrinsic stiffness. Muscle stiffness will be measured while subjects move the joint over a set range of motion while trying to maintain a target force

Muscle stiffness was measured on a Lido Isokinetic Dynamometer and with a handheld myotonometer. The Lido measures the amount of force or torque applied by the subject and the velocity in which that force is applied or resisted. Electrodes were placed on major flexor and extensor muscles to record EMG activity of muscles during testing.

10 subjects were completed and full data analysis will be completed by October 1996. The results and discussion in this report represents a detailed analysis of the new NASA method of measuring tricep surae (ankle, plantar flexion) stiffness from one subject.

INTRODUCTION

The primary focus of the Neuromuscular Laboratory (NML) is to determine how neural (central and peripheral) components affect muscle performance. Muscle stiffness (agonist and antagonist muscles) can affect performance (Figure 1). However, one must be able to quantify and understand the underlying physiological mechanisms that affect stiffness. Therefore, this study examined methods to assess muscle stiffness. Muscle stiffness has been quantified by tissue reactive force (transverse stiffness), vibration, and using Hooke's Law (force or torque over displacement). Muscle stiffness also has two components: reflex (due to muscle spindle activity), and intrinsic (actin & myosin cross-bridges and connective tissue). This study compared muscle stiffness of agonist-antagonist muscle pairs of the ankle, knee, and elbow using three different methods. The first method utilized a Russian designed myotonometer. This tonometer assesses tissue reactive force (when measured at rest, reactive force = intrinsic). The next method measured total stiffness by perturbing the distal limb to produce a 1 Hz frequency. During this motion, the subject attempted to maintain a target force (Sinkjaer et al 1988). The third method used Hooke's law to quantify stiffness from the torque vs position regression. The slope of this regression is Hooke's constant. The torque was generated from a maximal isokinetic concentric contraction produced by the subject immediately after completing a maximal isokinetic eccentric contraction with the same muscle. This post-eccentric concentric contraction has two linear components: one at and above optimal muscle length and one below this length. The slope of the regression below the optimal muscle length is intrinsic (tonic firing of motor units, elastic nature of actin and myosin cross-bridges, and connective tissue) stiffness, while the slope above this point is the total stiffness. Reflex stiffness is the difference between these measures. Previous research demonstrates an increase in stiffness with increases in background or initial forces.

The aim of this preliminary investigation was to compare transverse to Intrinsic and Sinkjaer to NASA's measures of total stiffness in three different agonist-antagonist muscle pairs in men and women.

- Hypothesis 1:** All stiffness will increase with increases in background or initial torques.
- Hypothesis 2:** Total stiffness by the NASA method will equal the stiffness by the Sinkjaer method and both will be higher than intrinsic (NASA method) and transverse stiffnesses at all levels of background or initial torques.
- Hypothesis 3:** The transverse stiffness will be equivalent to intrinsic stiffness for each muscle.
- Hypothesis 4:** The stiffness of agonist-antagonist muscle pairs will be equivalent.

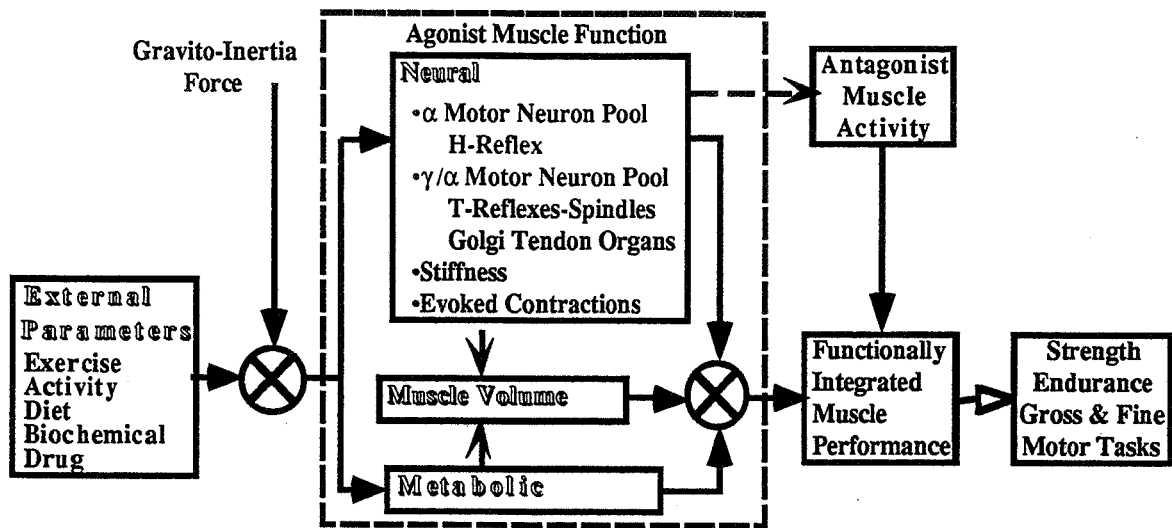


Figure 1. This figure represents a schematic of the interrelationships between neural and metabolic factors and how they, in combination with muscle size, functionally integrate to control muscle performance. Also included in this figure are the influences of outside sources, such as the possible co-contraction of the antagonist muscle and external parameters. External parameters include exercise, daily activity, diet, biochemical (e.g., hormones, growth factors, etc.), drugs, and gravity. Gravity is the gravito-inertial force since movement in a 1-g field requires a more continuous force while in 0-g movement only requires impulse type forces. Some external parameters (exercise, activity, drug availability) will affect muscles differently when applied in different gravitational fields. In addition, different gravitational fields may influence diet, the quantity and activity of naturally occurring biochemicals (e.g., hormones, growth factors, etc.), higher order neural functions with descending tracks to the alpha motor neuron pools, delivery of oxygen, and muscle oxygen kinetics. Changes in these parameters may affect neural and metabolic factors that in turn would influence muscle size and performance.

METHODS

Subjects

Subjects were 10 (6 men and 4 women) healthy volunteers with no current or past orthopedic problems of the right ankle, knee or elbow.

Total Stiffness

Total Stiffness is the sum of reflex and intrinsic stiffness. Sinkjaer et al (1988) passively moved the ankle (ROM of 1, 2, 4, & 7 degrees) at ~1.1 Hz while the subject contracted the muscle to maintain a target force (0, 20, 40, 60, and 80% maximal voluntary isometric contraction). The mean force becomes the background torque and the $\Delta\text{Force}/\text{ROM}$ was the total stiffness.

LIDO Application of the Sinkjaer Method

- Lido set at continuous passive motion with no pauses.
 - + ROM-1 is $\pm 5^\circ$ about the neutral ankle and 60° of leg or elbow flexion.
 - + Contraction velocity of $20^\circ/\text{s}$ (produces 1 Hz movements) for 10° ROM (ROM-1).
- Subject monitored force on screen to keep at target level (bar graph feedback).
- Subject's target forces were 0, 20, 40, 60, 80, and 100% MVC (isometric).
- Subject performed 6 trials with rest for 1 minute between each level of background torque.
- EMGs were recorded from agonist and antagonist muscle pairs.
- EMG, force and position data was collected with a computer data acquisition system.
- Stiffness of the flexors and extensors of the ankle, knee, and elbow was recorded.

Intrinsic Muscle Stiffness

Intrinsic muscle stiffness is the stiffness when neural inputs have little or no influence on force production. Sinkjaer et al (1988) measured intrinsic stiffness with electric stimulation (which was not well tolerated by the subject). We used the maximal isokinetic force prior to optimal muscle length to minimize the reflex input to force generation and evaluate stiffness as the slope of the torque vs position (angle) regression.

NASA Method for Total and Intrinsic Stiffness

Intrinsic muscle stiffness was assessed on the LIDO Multi-Joint Isokinetic Dynamometer.

- The subject performed a maximal eccentric contraction followed immediately by a concentric contraction. The slope of the post-eccentric concentric contraction is the intrinsic stiffness.
- This was done over the complete ROM (ROM-2: 20 Dorsiflexion to 25 Plantar for ankle, $10-90^\circ$ ROM for the knee and $10-110^\circ$ for elbow).
- Subjects completed 6 post-eccentric concentric contraction at each ROM for LIDO contraction speeds of 40, 80, 120, 160, 200, and $240^\circ/\text{s}$.
- Subjects rested for at least 1 minute between each set of 6.
- EMGs were recorded from agonist and antagonist muscle pairs.
- EMG, force and position data was collected with computer data acquisition system.
- Stiffness flexors and extensors of the ankle, knee, and elbow were recorded.

Transverse Stiffness (Russian Protocol).

Transverse stiffness is the stiffness recorded by pressing a tonometer into the muscle group and recording the relative tissue reactive force. The tissue reactive force produces a curvilinear response ($\sim 2^{\text{nd}}$ order). At the point where the curve becomes linear (Figure 2), stiffness is measured as the difference in force (downward force of tonometer - tissue reactive force) for the standard deflection (2 mm).

- Subjects relaxed and 6 measures of tone were recorded over the largest part of the muscle (marked with a pen).
- Subjects performed 3 maximal isometric contractions, each lasting $\sim 5-10$ seconds.
- Investigators repeated transverse muscle stiffness measures while the subject exerted forces equal to 20, 40, 60, and 80% maximal voluntary isometric contraction.
- Subjects rested for at least 1 minute between each contraction.
- Stiffness of the flexors and extensors of the ankle, and extensors of the knee, and elbow were recorded.

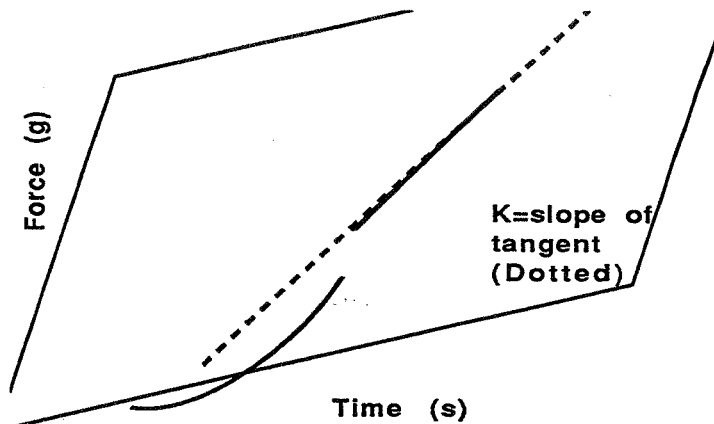


Figure 2. Tissue Reactive Forces Over Time from a Russian Myotonometer.

Data Analysis

1. Linear and polynomial regression will determine the relationship between stiffness from each method and the background or initial torque.
2. Dependent t-ratios or ANOVAs will determine differences between stiffness methods at the different levels of background torques. Newman-Keuls Post Hoc testing will be used when appropriate.

RESULTS/DISCUSSION

We have 10 complete data sets (EMG, force and position). Analysis software is still being written so that inter-scorer variability does not influence the results. The planned data analysis will not be completed until October, 1996. Therefore, this section reports a detailed analysis of the new NASA method of measuring tricep surae (ankle, plantar flexion) stiffness from one subject. Data was analyzed in the raw volt form.

Figure 3 shows the change in stiffness (@ 100 ms intervals) during the post eccentric (prestretched and preloaded) concentric contraction. Notice that stiffness starts high (0.75 V/V) then decreases and reaches equilibrium (~0.62 V/V) about 450 ms into the contraction. At this time the subject's foot is past optimal angles for peak force generation and all reflex input (from stretch and Golgi tendon organ receptors) should be minimal. Examination of the EMG activity of the agonist (medial gastrocnemius; MG) and antagonist (tibialis anterior: TA) may show the relative contributions of the stretch and Golgi tendon organ (force sensor) receptor input to the total stiffness.

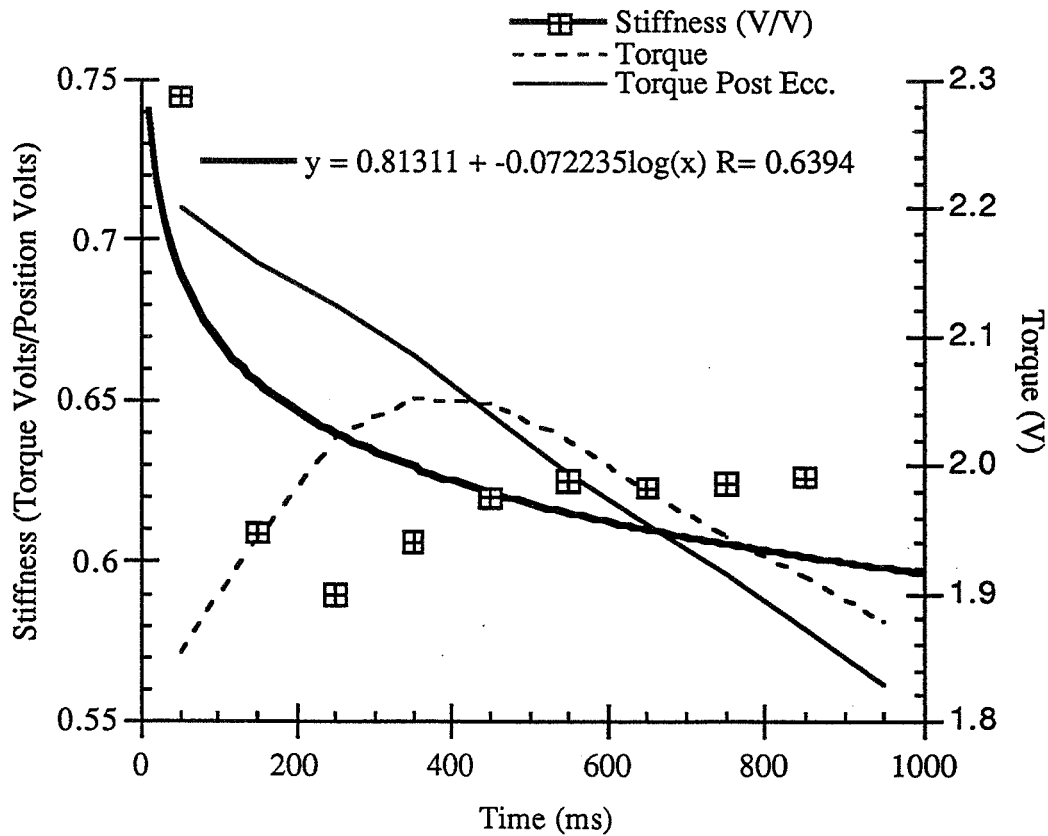


Figure 3: Serial stiffness (Torque in Volts/Position in Volts shown as boxes) values of the tricep surae (calf) during the post-eccentric concentric contraction (thin line) are shown. The heavy solid line shows the logarithmic plot the stiffness vs time (ms) data. The dotted line shows the normal concentric contraction and the area of optimal (peak part of curve) force production.

Figure 4 shows the force (during plantar flexion of the ankle) and MG EMG (averaged with root mean square) of concentric and post-eccentric (prestretched and preloaded) concentric contractions. Figure 1 suggests that the reflexes (stretch and force receptor inputs) may help determine muscle stiffness. The EMG data showed larger activity for the first 100 ms during the prestretched concentric contraction. This may indicate the involvement of the stretch reflex. However, during the next 100 ms interval there was no difference between the EMG activity of the two contractions. This suggests that stretch reflex contributed to the increase in muscle force and therefore stiffness during the onset of this contraction.

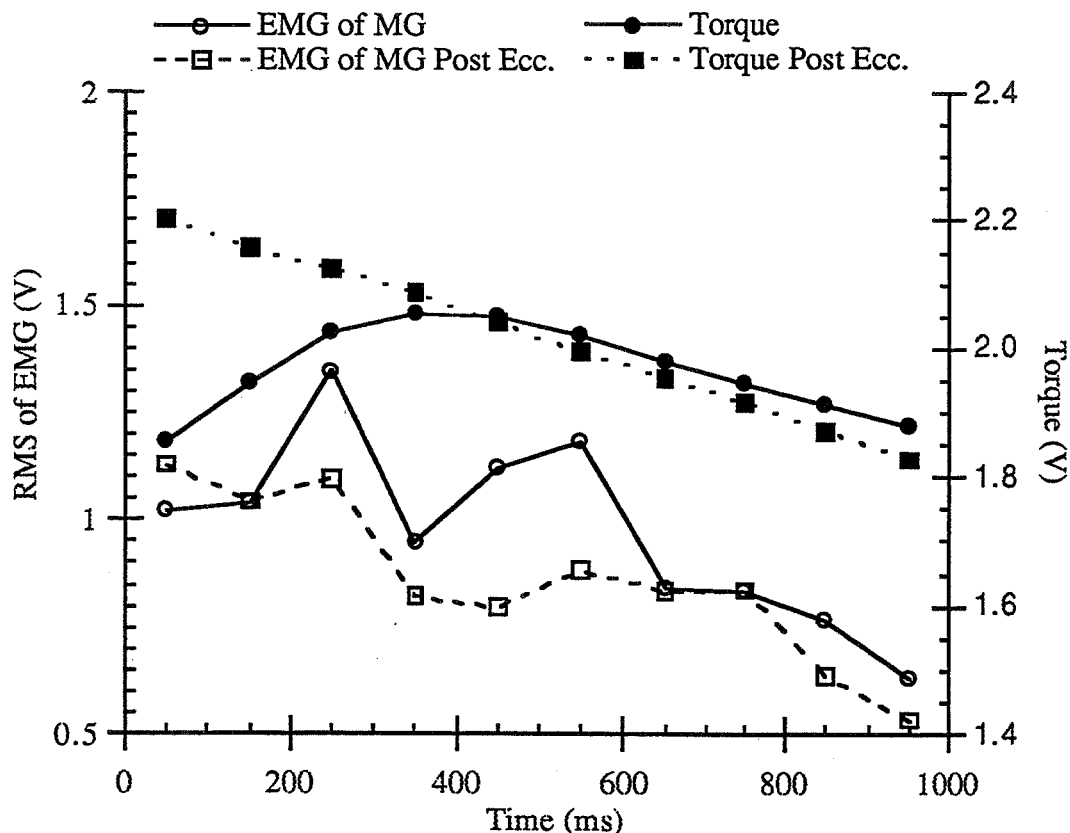


Figure 4: RMS (root mean square averaging) EMG of medial gastrocnemius (agonist muscle) during the concentric (open circles - solid line) and post-eccentric concentric contraction (open boxes - dashed line) are shown. Torque (V) during the concentric (closed circles - solid line) and post-eccentric concentric contraction (closed boxes - dashed line) are shown.

Figure 5 shows the force (during plantar flexion of the ankle) and the TA EMG (root mean square) of the tibialis anterior muscle (antagonist muscle). Notice the increase in EMG of activity (open arrow) of the antagonist muscle during the first 400 ms of the normal contraction, while during the contraction following an eccentric contraction the EMG activity tends to decrease (closed arrow). This demonstrates the firing of Golgi tendon organs located in the Achilles tendon. These muscle sensors respond to changes in force by activating antagonist muscles. The early decrease in antagonist muscle activation in the post eccentric contraction decreases some of the resistive force in the joint and progressively decreases joint stiffness. This is reflected in the total and intrinsic stiffness. Total stiffness reflects muscle and joint stiffness (joint stiffness possibly increases due to stretch and Golgi tendon organ receptors adding force to the agonist and antagonist muscles prior to optimal force production).

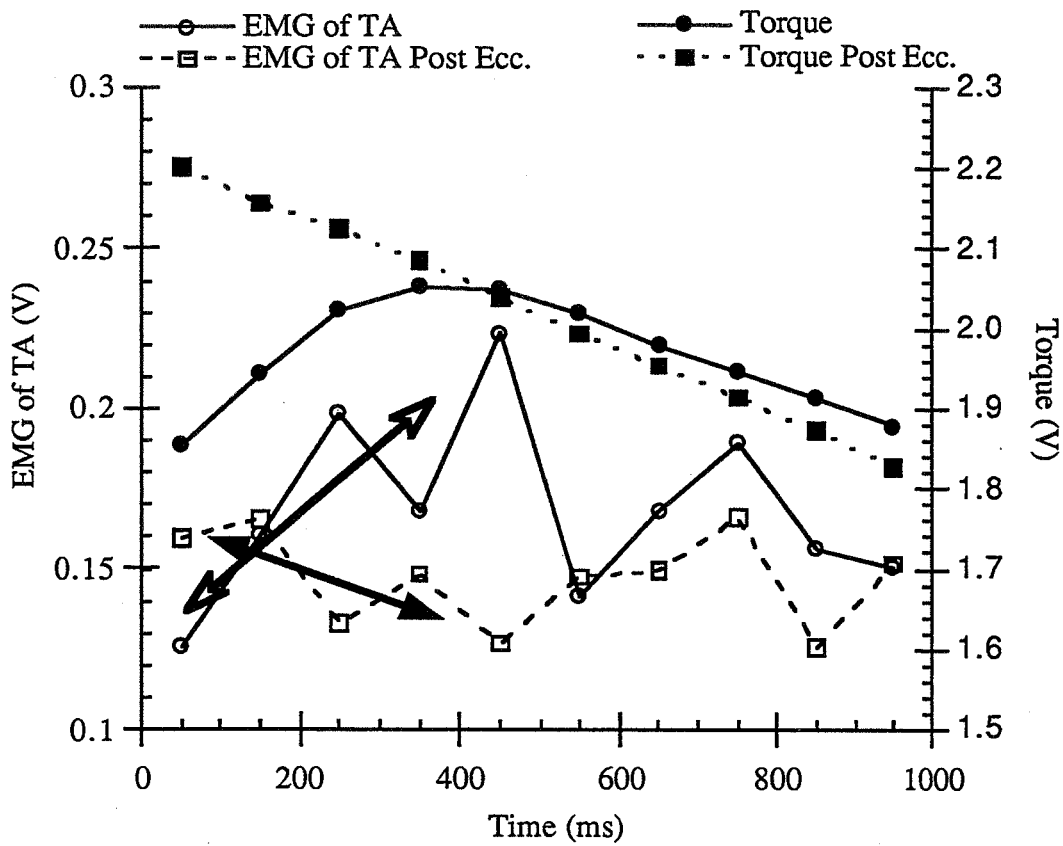


Figure 5: RMS (root mean square averaging) EMG of tibialis anterior (antagonist muscle) during the concentric (open circles - solid line) and post-eccentric concentric contraction (open boxes - dashed line) are shown. Torque (V) during the concentric (closed circles - solid line) and post-eccentric concentric contraction (closed boxes - dashed line) are shown.

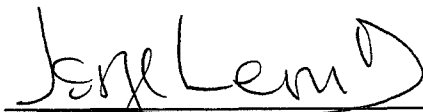
REFERENCE

Sinkjær T, E Toft, S Andreassen, BC Hornemann. Muscle stiffness in human ankle dorsiflexors: Intrinsic and reflex components. *J. Neurophysiology*. 60:1110-1121, 1988.

**INTEGRATION OF CELSS SIMULATION WITH
LONG-TERM CROP SCHEDULING**

V. Jorge Leon
Texas A&M University
ER2
July 12, 1996

Jon Erickson
Intelligent Systems Branch
Automation, Robotics and Simulation Division
Directorate of Engineering


V. Jorge Leon


Jon Erickson

**INTEGRATION OF CELSS SIMULATION WITH
LONG-TERM CROP SCHEDULING**

**Final Report
NASA/ASEE Summer Faculty Fellowship Program - 1996
Johnson Space Center**

Prepared by:	V. Jorge Leon, Ph. D.
Academic Rank:	Assistant Professor
University & Department:	Texas A&M University Engineering Technology Department College Station, TX 77843-3367
NASA/JSC	
Directorate:	Engineering
Division:	Automation, Robotics and Simulation
Branch:	Intelligent Systems
JSC Colleague:	Jon Erickson, Ph. D.
Date Submitted:	July 12, 1996
Contract Number:	NAG 9-867

INTEGRATION OF CELSS SIMULATION WITH LONG-TERM CROP SCHEDULING

V. Jorge Leon
Texas A&M University

Jon Erickson
NASA-JSC

ABSTRACT

This project presents guidelines for the integration of the Intelligent Crop Scheduler (ICS) developed by Leon (1995) with a version of the Biological Life Support System (BLSS) simulation based on the work by Volk and Rummel (1987). These guidelines will also aid in defining the appropriate model detail of simulation-based schedulers. ICS determines *what, when* and *how much* to plant of different crops. These decisions are made such that the critical reservoir levels are maintained close to their nominal or desired settings during the duration of the mission. Initial feasibility of the approach has been demonstrated using simplified implementations of the scheduling approach and CELSS "world" model developed by the investigator at JSC in the Summer of 1995. The BLSS model incorporates more detail. The increased fidelity is in terms of added mass-regeneration formalism (biochemical stoichiometry), more plants, and more accurate modeling of the mechanical system. This report describes the main features of the Crop scheduler and CELSS simulator, discusses integration issues, and provides with detailed guidelines for the integration of these two applications.

INTRODUCTION

A CELSS must sustain a moderate size crew for a number of years with minimum re-supply of mass. In this environment, long-term strategic resource management becomes vital. In particular, higher plants are critical resources for food and carbon-dioxide to oxygen regeneration. Plants play an important role in the regeneration of water, wastes, and nitrogen components. Decisions of *what*, *when* and *how much* to plant are non-trivial due to the long-term dynamics associated with plant growth and human behavior. Other complicating factors include, food processing, limited space, limited reservoirs and energy considerations. Ultimately, planting decisions must be driven by the goal of providing the crew with adequate living conditions for the successful completion of mission objectives. The crop planting problem poses a challenging combinatorial optimization problem augmented by the complexity of the underlying world model.

This report is organized as follows: A background section provides with the foundations for the remainder of the paper. The crop scheduler and simulator are described; integration issues are determined and discussed; a minimal set of modifications are given for model consistency; some future model improvements are listed; finally, a two-phase integration plan is proposed.

BACKGROUND

The Crop Scheduling Problem

Crop scheduling refers to the decisions of *What*, *When*, and *How Much* to plant during a given planning horizon. *What* to plant decisions must select between various plant types (about 15 or more). *When* to plant consider a planning horizon measurable in years, while the phenomena under consideration take place in the order of days. *How much* to plant is restricted by the maximum planting area in the growth chambers (currently a few hundred square meters) and the size of the planting trays (currently about one square meter). As a result, the decision under consideration arenon trivial due to the large size of the solution space.

The crop scheduling problem has important differences from a traditional *scheduling* and *planning* problems. In traditional scheduling, mainly the decisions concerning *when* to plant would be considered; hence, it is assumed that *what* and *how much* to plant is known in advanced. On the other hand, in traditional planning problems the decisions of *when* to plant need not be fully specified. Clearly, the crop scheduling problem considered here is very challenging (Leon, 1995).

Intelligent Crop Scheduler (ICS)

As shown in Figure 1, the ICS consists of two modules. The first module is the *Schedule Generator* (ICS-SG) and is based on the work in Leon (1995). The second module is a *Schedule Simulator* (ICS-SS) developed by Leon and Whitaker (1995). ICS-SG

generates a schedule of planting decisions and passes it to the simulator, ICS-SS, for more detailed validation. ICS-SG uses a lower fidelity model of the world than the ICS-SS. Determining what is the appropriate level of detail of the simulation models for scheduling involves a trade-off between accuracy of the predicted behavior and computation time. Preliminary testing with ICS suggests that good performance is achieved if ICS-SG and ICS-SS deal with phenomena in the order of "days." More detailed simulation may not be justifiable since only planting decisions and a relatively long planning horizon (e.g., 1-2 years) are considered. It may be necessary to develop more detailed simulations (hours) to evaluate short-term (e.g., a few weeks) system performance. Some additional guidelines are given later in this report.

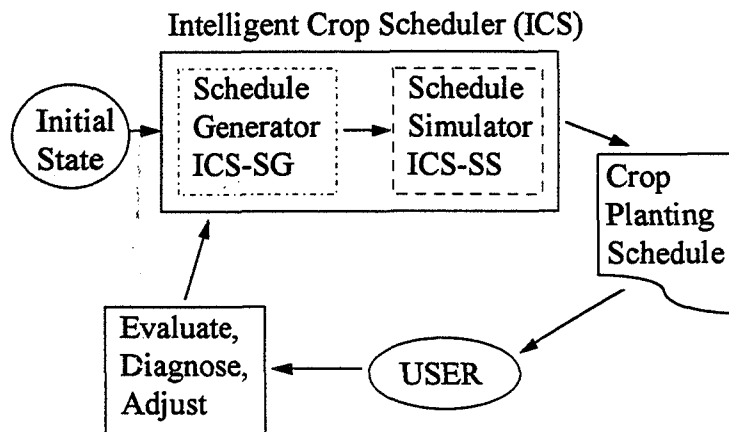


Figure 1. The Intelligent Crop Scheduler (Adapted from Leon, 1995)

Figure 2 shows the world model used in ICS-SG. It consists of three processors (human, plant, waste processor) and three reservoirs (food, O₂ and CO₂). For simplicity, net mass-flows are considered from processors to reservoirs, and vice-versa. However no direct flows are considered between processors or between reservoirs.

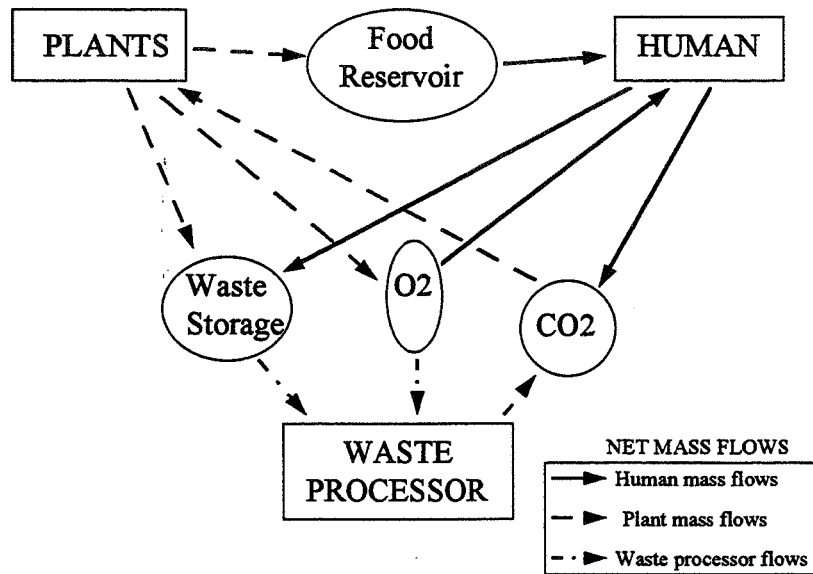


Figure 2. CELSS world model used in ICS-SG (Adapted from Leon, 1995).

Two important control strategies on what processors in the system to act on can be inferred from this simplified representation of the world (see Figure 2). Given the mass-closure condition, the stability (short- and long-term) of the system depends to a great extent on the degree in which reservoir levels are maintained close to their corresponding nominal levels. First, it makes sense to use the reservoir levels over time to derive surrogate measures of the probability-of-survival over that period of time. Second, in order to control the reservoir levels, one can exert control actions upon plants and waste processor. Acting on humans may not significantly affect the system in the short term. Very fast responses of the reservoir levels can be achieved by changing the environmental conditions in the growth chamber, or processing a certain amount of a given waste. On the other hand, long term reservoir levels can be controlled by carefully deciding on crop planting events. In summary, if the objective is to maintain healthy reservoir levels, then carefully manage crop planting (i.e., crop scheduling) for long-term stability, and waste processing and growth conditions for short-term stability. Care must be taken in the latter case because changes in growing conditions may resolve short-term problems but may drastically affect long-term behavior (e.g., reduced crop production rates).

BLSS Simulation

Excellent descriptions of this model can be found in Rummel and Volk (1987), Volk and Rummel (1987) and WinCELSS's User Manual.

Briefly BLSS "models an environment consisting of two modules, a crew compartment (CCM) and a plant growth module (PGM). Up to 100 humans and 180 "fields" each of lettuce, potatoes, soybeans, and wheat are modeled. Flows of Carbon, Hydrogen, Oxygen

and Nitrogen are tracked while the simulation executes. In addition to the initial conditions, twenty six different kinds of events (crew rotation events, crop/field planting events, resupply events, and catastrophes -- crop failures, food contamination, major resource losses, equipment failures) can be scheduled to occur throughout the simulated time period” (WinCELSS User Manual). The world model is depicted in Figure 3.

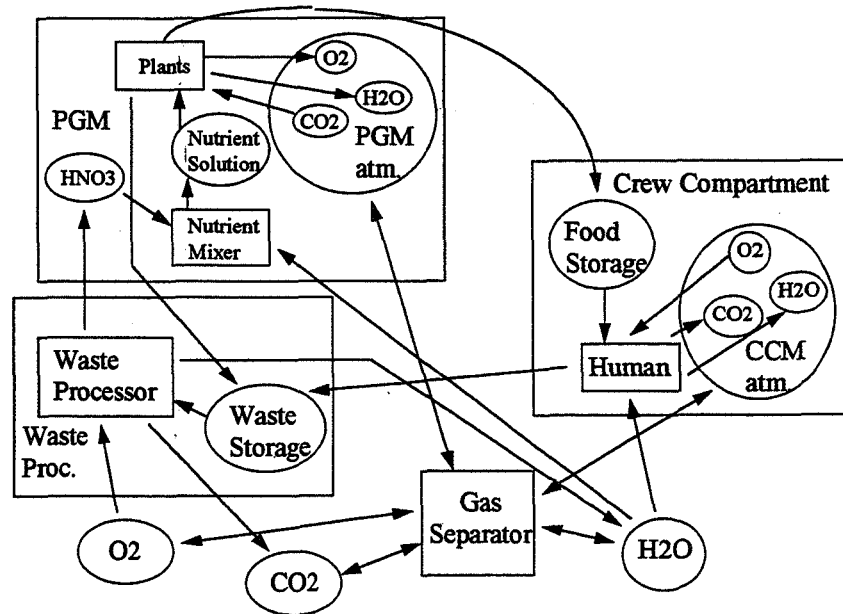


Figure 3. BLSS model (Adapted from Rummel and Volk, 1987).

The simulation model has the following main steps:

```

Bio_Init; {Initialize biology}
    Crop_Flows(); {determines main mass-flux rates associated with plants}
    Total_PCLF(); {protein, carbohydrates, lipids and fiber required by humans as per
        given menu preference}
    Hum_Flux(); {determines main mass-flux rates associated with humans as per PCLF}

CCM_Init; {Initialize crew compartment atmosphere}

PGM_Init; {initialize plant growth module atmosphere}

Initialize reservoirs

Simulation LOOP:
    Process events at given time
    Simulate one hour of the system
  
```

A major feature of BLSS is the approach used in determining mass-flows balances based on the work in (Volk and Rummel, 1987). As shown above, these calculations are performed mostly in procedure Bio_Init. The approach used is summarized in the following paragraphs.

Mass flow rates associated with plants are computed by (see Crop_Flows()):

- decomposing each plant type into their content of main nutrients (i.e., protein, carbohydrates, lipids and fiber);
- each main nutrient is then decomposed into main compounds (i.e., O₂, CO₂, HNO₃ and H₂O) or elements (C, H, O and N) using the biochemical stoichiometry derived in Volk and Rummel (1995);
- mass-flow rates are derived solving simultaneous equations established in the previous step assuming 1 gram of total mass.

Mass flow rates associated with humans are computed by (see Hum_Flux()):

- compute the fractions of protein, carbohydrates lignin and fiber that each human will consume based on a given diet. A diet is expressed as the amount of each plant type that the crew will like to eat in each meal and number of meals per day.
- given the amounts of main nutrient consumed, use the equations that convert food to human wastes also from Volk and Rummel (1995);
- once the human wastes are expressed in terms of their main chemical components, the mass flow rates are computed similarly than for the plant case above.

Mass flow rates associated with wastes, use the waste compounds derived for plant and human wastes and are converted to CO₂, H₂O and HNO₃.

INTEGRATION ISSUES

Similarities Between ICS and BLSS models

The current implementations of ICS and BLSS have two major similarities.

1. In both cases the fundamental system components are:

- processors (humans, plants, and waste processor)
- reservoirs (chemical components, wastes and food), and
- mass flows in a closed system.

Minor differences are due to more detailed world model used in BLSS. Notably:

- a. BLSS uses CO₂, O₂, Waste, Food, H₂O, Plant Nutrient and HNO₃ reservoirs; ICS only considers the first four.
- b. BLSS considers lettuce, wheat, soybean and potato. ICS only considers the first two. However, it appears that the BLSS plant growth models are

basically the same but with different parameter values for each plant type. ICS uses two different growth functions from the literature.

- c. BLSS mass flows and conversion rates are based on formal chemical stoichiometry; ICS uses rough estimates from the literature and plant growth experiments at JSC.
2. Both simulators (i.e., ICS-SS and BLSS) are event based. Moreover, both simulators can run from a prespecified list of crop planting events (in addition, BLSS can consider 26 different types of events). However, as it will be discussed later, some fundamental modifications are needed before these two programs can be used together.

These design similarities encourage the pursuit of the integration of ICS and BLSS. Specifically, it seems appropriate:

- to replace ICS-SS by BLSS, and
- modify ICS-SG for world model consistency.

Differences Between ICS and BLSS models

Although the ICS and BLSS are mostly compatible, there are some fundamental inconsistencies to resolve.

1. *The BLSS simulator assumes that planting occurs automatically after harvesting.* Therefore, the crop mixes in-growth at any point of time is mainly a function of (i) the initial planting decisions and (ii) the growth cycle of each plant-type. This is a major limitation because no consideration is given to the state of the system at the time of planting.

In scheduling terms, the strategy currently implemented in BLSS is a *static cyclic scheduling strategy*. A direct result of this assumption is that the same amount of each crop is always in-growth at any point of time. Although this strategy has many operational and logistic benefits, it is still necessary to determine (a) how much to plant (initially) of each crop type, and (b) what to do when the system deviates from the nominal planned path. First, deciding how much to plant of each type of crop is non-trivial once menu preferences, resource (time, energy, space) limitations, and mass-closure is considered. Second, invariably, the random disturbances will occur that will require the dynamic adjustment of the original cyclic schedule. The crop scheduler is aimed at answering these questions.

Clearly, this assumption needs to be relaxed to make the BLSS more flexible in terms of crop scheduling. In other words, the simulator must allow the user specify, at desire, the planting time and quantity to be planted (including the cyclic scheduling option).

2. *Edible-biomass waste processing* is considered in BLSS but not in ICS. In BLSS, a fixed level of food is prespecified which should last until the next harvest is due. At any point of time the “excess edible portion, if any, is sent to the Waste Storage” (Rummel and Volk, 1987). It seems that a strategy as this makes sense only under cyclic scheduling with minor disturbances; hence, this must be modified in conjunction with (1) above.
3. *Simulation time increments*. BLSS advances time every hour; ICS currently uses one day time advances. It is conjectured that using one day increments will suffice for long-term crop scheduling (e.g., 2 years look ahead). Clearly, smaller time increments may be implemented at the expense of shorter look-ahead and/or more computation time.

Model Detail

Detail refers to the fidelity with which the model represents the real world. A different level of detail is required for schedule *generation* than for schedule *validation*. Typically, the level of model detail used during generation should be coarser than that used during schedule validation. This difference in detail is aimed at reducing the computation requirements during scheduling generation.

Albeit modifications required mentioned later in the report, **the detail of the BLSS model is adequate for initial validation of long-term (up to two years) crop scheduling decisions. However, it is too detailed for schedule generation using the ICS-SG approach.**

Guidelines for the simplification of BLSS for schedule generation purposes. The underlying assumption is that, maintaining close-to-nominal reservoir levels in the long term is directly related to the probability of survival and long-term system stability.

1. Determine the *processors* that have main roles in mass transformation.
2. Determine the *reservoirs* that are critical.
3. Establish net mass flows from processors in (1) to reservoirs in (2), and vice-versa.
4. Assume that there is no direct mass interchange between processors; but instead, there is always a reservoir between processors.

To make ICS-SG consistent with BLSS, it is necessary to consider three processors and six reservoirs, namely:

Processors: Human, plants, Waste Processor.
 Reservoirs: CO₂, Food, H₂O, O₂, HNO₃, Waste.

Figure 4 shows a CELSS model that can be used for a revised version of ICS-SG and is consistent with the BLSS simulator.

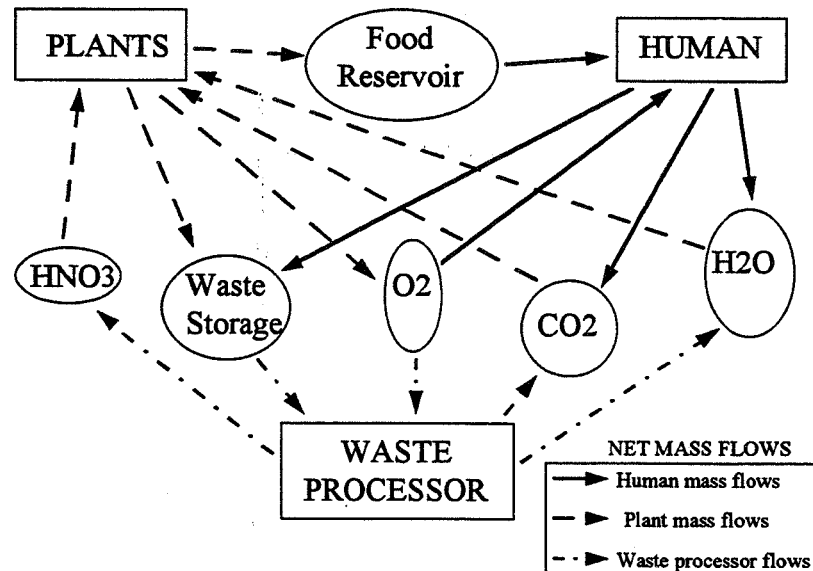


Figure 4. Proposed CELSS world for compatible ICS-SG and BLSS simulator.

When compared with the BLSS model (see Figure 3), the ICS-SG model is simpler (i.e., less fidelity) because it does not explicitly consider:

- PGM atmosphere
- CCM atmosphere
- Gas separator
- Nutrient mixer
- Nutrient mix storage

Of notice is that, only minor modifications are needed to enhance the world model in the current implementation of ICS-SG (compare Figures 2 and 4). This suggests a convenient level of modeling abstraction.

Although simpler, the net mass flows from-and-to the reservoirs will be very close to the ones considered in the BLSS simulator. As a result, the main C, H, O and N transformations are considered in the form of the main components CO₂, H₂O, HNO₃, O₂, edible biomass and waste (human and inedible biomass). The conversion rates associated with each of the arrows on Figure 4 will be described in detail later in the report.

Simulated Time Increment. The simulated time increment used in BLSS is one (1) hour; i.e., time advances in one (1) *hour* increments. Again, this may be appropriate for

schedule validation, but too fine for schedule generation using ICS-SG. The smallest time increment recommended for schedule generation is one (1) *day*; smaller time increments may result in lengthy schedule generation times with little gains in information.

It may be possible to estimate the *maximum simulated-time-increment (MSTI)* as half the minimum time any of the reservoirs can be beyond acceptable levels without causing catastrophic system failure. The simulation module of the crop scheduler (e.g., ICS-SS or BLSS) must use MSTI or smaller time increments. As a starting point, the schedule generation module of the crop scheduler should use $\text{Max}\{ \text{MSTI}, \text{one day} \}$.

MINIMAL REQUIRED MODIFICATIONS

The following sections will describe the minimal modifications of the current implementations of ICS and WinCELSS. The implementation of the recommended modifications are required before the integration of these applications.

ICS Modifications

Modifications are required:

1. Code modification due to added detail. This includes:
 - Add soybean and potato.
 - Add H₂O and HNO₃ reservoirs.

The modification of the current ICS-SG program is straight forward since it was designed to allow for the incorporation of more plants and reservoirs.

2. More accurate mass flow-rates and conversion factors as per the BLSS model. Most mass-flux rates can be computed using the functions in `Bio_Init` from the WinCELSS program. In particular, the functions `Crop_Flows()` and `Hum_Flux()` contain most necessary expressions. Plant growth rates can be estimated using the functions in `Delta_Growth()` from the WinCELSS program. Notice that, these factors are input parameters for ICS-SG; therefore, **no major modification of the code will be required**. It would be advisable to write **preprocessing routines** that sets all these values at the beginning of the program.

BLSS Modifications

1. Eliminate automatic replanting. Currently function `Simulate_PGM` executes the function `Plant_Some()` when it detects the variable `crop_time` with a value of -1.
2. Allow for "storage" of excess edible biomass. Modification can start in procedure `ComputeNeededFood()` where the amount of edible waste is computed in the following expression:

edibleWaste:= edibleWaste + (edible - foodNeeded);

3. Use 1 day simulated time increments.

ICS-SG and BLSS CORRECTIONS AND ENHANCEMENTS

ICS Corrections and Enhancements

The current procedure use in ICS-SG is only a preliminary one and can be enhanced to generate better quality solutions (Leon, 1995).

In terms of the underlying model, it seems important to consider explicitly:

- cyclic schedules
- harvest pre-processing
- meal preparation processes
- food menus
- crew workload to carry out planting, harvesting and related activities.
- expand to schedule waste processing activities.

BLSS Corrections and Enhancements

- Plant models are the same
- Crew loading
- Harvesting patterns
- Effect of temperature on biomass production
- Effect of temperature on human metabolism
- Food storage capacity
- Food shelf-life.
- Food processing
- Food processing occurs with a hard-coded "waste-processing batch"

A TWO PHASE INTEGRATION PLAN

A two phase plan is proposed for the integration of ICS and BLSS:

- Phase I: Decoupled Consistent Applications. The two applications are run separately, with ICS generating a schedule consistent with the parameters set for BLSS, and BLSS simulating the schedule generated by ICS. This phase involves the implementation of the minimal modifications mentioned previously.
- Phase II: Integrated Tool. A single program integrates ICS and BLSS. Possibly adding "schedule generation" capabilities to a WinCELSS-like user

interface. A major development issue is that WinCELSS is written in Delphi Pascal (version 1.0) while ICS is a C-ANSI program.

It is estimated that Phase I can be completed in 1.5 months and Phase II can be completed in 1.5 months (1 person full time).

CONCLUDING REMARKS

In conclusion, the integration of ICS and BLSS is feasible with relatively minor coding effort. The resulting scheduling and simulation tool can be a valuable decision support tool for system analysts, designers and operators. Its structure will provide a foundation for enhancements and refinements as the technologies to be used become available. Further, this project will demonstrate how better fidelity world models can be easily incorporated with the scheduling methodology.

REFERENCES

Leon, V.J., "Intelligent Planning and Scheduling for Controlled Ecological Life Support Systems," NASA Summer Faculty Fellowship Program, 1995.

Rummel, J.D. and T. Volk, "A Modular BLSS Simulation Model," *Advanced Space Research*, vol. 7, no. 4, 59-67, 1987.

"User Manual for the Controlled Ecological Life Support System (WINCELSS) Simulator," Information Technology Office, NASA Johnson Space Center, JSC-27239.

Volk, T. and J.D. Rummel, "Mass Balances For A Biological Life Support System Simulation Model," *Advanced Space Research*, vol. 7, no. 4, 141-148, 1987.

Whitaker, L.O. and V.J. Leon, "An Intelligent Crop Planning Tool For Controlled Ecological Life Support Systems," NASA Summer Faculty Fellowship Program, 1995.

Influence of Zero-shear on Yeast Development

Michael R. McGinnis, Ph.D.
University of Texas Medical Branch
SD-4
August 9, 1996

Duane L. Pierson, Ph.D.
Life Sciences Research Laboratories
Space and Life Sciences Directorate


Michael R. McGinnis, Ph.D.


Duane L. Pierson, Ph.D.

Influence of Zero-shear on Yeast Development

**Final Report
NASA/ASEE Summer Faculty Fellowship Program-1996
Johnson Space Center**

Prepared by:	Michael R. McGinnis, Ph.D.
Academic Rank:	Professor
University & Department	University of Texas Medical Branch Department of Pathology Galveston, Texas 77555-0609
NASA/JSC	
Directorate:	Space and Life Sciences
Division:	Medical Sciences
Branch:	Life Sciences Research Laboratories
JSC Colleague:	Duane L. Pierson, Ph.D.
Date Submitted:	August 9, 1996
Contract Number:	NAG9-867

ABSTRACT

The objective of the research was to begin evaluating the effect of zero-shear on the development of the cell wall of *Saccharomyces cerevisiae* employing the High Aspect Rotating-Wall Vessel (HARV) NASA bioreactor. This particular yeast has enormous potential for research as a model eukaryotic system on the International Space Station, as well as the production of food stuffs' at the future lunar colony. Because the cell wall is the barrier between the cell and the environment, its form and function as influenced by microgravity is of great importance.

Morphologic studies revealed that the circularity and total area of the individual yeast cells were essentially the same in both the control and test HARVs. The growth rates were also essentially the same. In zero-shear, the yeast grew in clumps consisting of rudimentary pseudohyphae in contrast to solitary budding cells in the control. Based upon mechanical and sonic shear applied to the yeast cells, those grown in zero-shear had stronger cell walls and septa This suggests that there are structural differences, most likely related to the chitin skeleton of the cell wall.

From this research further NASA support was obtained to continue the work. Investigations will deal with gene expression and ultrastructure. These will lead to a clearer assessment of the value of *S. cerevisiae* eukaryotic as a model for space station research.

INTRODUCTION

A practical method to study the influence of microgravity upon yeast cells involves using the High Aspect Rotating-Wall Vessel (HARV). The HARV (1) emulates microgravity, as well as provides an environment for efficient exchange of oxygen and carbon dioxide across a silicone membrane oxygenator. The instrument has been successfully used to cultivate a variety of eukaryotic cell types, anchorage-dependent and suspension cells, as well as normal and neoplastic cell lines. Preliminary studies conducted at NASA-JSC using species of *Candida* and *Lipomyces* have shown that these yeasts can be effectively grown and studied in the HARV (D. L. Pierson, unpublished data.)

The cell wall provides form and function for yeasts. Its mechanical strength enables fungi to assume a variety of shapes, such as proliferating solitary yeast cells to pseudohyphae. It provides protection to the protoplast against a large range of environmental stresses. For example, its physical strength protects the cell against osmotic bursting.

Chitin is a $\beta(1-4)$ -linked polymer of *N*-acetylglucosamine that occurs as a structural polysaccharide in the cell wall. Its molecular conformation gives the cell wall its mechanical strength. The individual chains of chitin are aggregated into microfibrils that are aligned in opposite directions to each other (2).

This study was undertaken to evaluate the effect of zero-shear upon the form and function of the yeast cell wall. Owing to its importance as a model, *S. cerevisiae* was selected for the studies.

EXPERIMENTAL SYSTEM

Based upon preliminary studies, yeast nitrogen base plus 0.5% glucose was selected as the growth medium. To insure that the yeast had ample time to produce a number of generations, the tests were incubated at 22°C. The yeast *S. cerevisiae* (ATCC 2366) was selected and all inocula were obtained from cultures that were 24 hrs old grown on Sabourand glucose agar incubated at 22°C. Approximately 10^7 cells were added to each HARVs, which can accommodate approximately 55 ml of medium.

The control HARV was run at approximately 10^0 to the horizontal with 5-10 glass beads. The test HARV was run as directed by the manufacturer. Both were rotated at 26 and 27 rpm. Approximately 2 ml of growth from each HARV was obtained daily. These samples were examined microscopically and cultured on Sabourand glucose agar or potato glucose agar to determine the number of colony forming units. An Optimas digital analysis system was used to determine circularity and area of the cells.

RESULTS

After 6 days of incubation, the colony forming unit (CFU) data showed that there were essentially no differences in the amount of growth. In one experiment, the values were 3.2×10^7 cfu/ml (control) and 2.4×10^7 cfu/ml (zero-shear).

The analysis of the individual cells showed that their circularity (ratio of perimeter length squared divided by the area) and total area (squared microns of the area of the cell) were essentially the same. In one experiment, the values were: median circularity 18.42 (zero shear) and 18.80 (control), and total areas of $49.16 \mu\text{m}^2$ (zero-shear) and $46.50 \mu\text{m}^2$ (zero-shear). These data are based upon the electronic separation of cells which had daughter cells as well as separated cells that were obtained by applying mechanical (vortexed, 30 seconds) and sonic (sonication, 2 minutes) shear forces.

Following the application of the two shear forces listed above, many of the zero-shear grown cells remained attached to each other. In addition, their cell walls were not broken. This is in contrast to the control cells which were separated from each other and many having broken cell walls.

CONCLUSIONS

The HARV has been shown to be an effective culture system for the cultivation of *S. cerevisiae* and *Candida albicans* (ATCC 14053, data not shown). The effect of zero-shear, an emulation of microgravity, can be studied in this system.

Preliminary data indicates that yeast cell shape (circularity) and size (total area) does not correlate with a zero-shear environment. A larger number of cells need to be evaluated before a final conclusion can be reached.

In zero-shear, yeast cells typically remain attached to each other forming rudimentary pseudohyphae. The attachment of the cells and their cell walls exhibit enhanced strength in comparison to cells grown in a shear environment. This suggests that there are structural differences, probably in the chitin, in the cell wall.

Future studies will be directed towards determining if ultrastructural differences exist, as well as the expression of chitin synthase and glucan synthase using PCR technology.

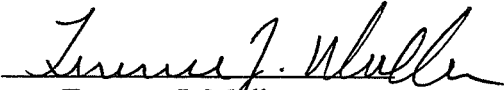
REFERENCES

1. Prewett, T.L., Goodwin, T.J., and Spaulding, G.F., "Three-dimensional modeling of T-24 human bladder carcinoma cell line: A new simulated microgravity culture vessel." *J. Tiss Cult. Meth.* 15; pp. 29-36: 1993.
2. Gooday, G.W. "Cell Wall". In GOW, N.A.R. and Gadd, G.M. (eds.). *The Growing Fungus*. Chapman and Hall, London; pp. 43-62: 1995.

COMPUTER BASED TRAINING:
FIELD DEPLOYABLE TRAINIER & SHARED VIRTUAL REALITY

Terence J. Mullen
Carroll College
DT47
July 24, 1996

Frank E. Hughes, JSC Colleague
Space Flight Training Division
Mission Operations Directorate


Terence J. Mullen


Frank E. Hughes

COMPUTER BASED TRAINING:
FIELD DEPLOYABLE TRAINER & SHARED VIRTUAL REALITY

Final Report
NASA/ASEE Summer Faculty Fellowship Program-1996
Johnson Space Center

Prepared By:	Terence J. Mullen
Academic Rank:	Associate Professor
University & Department:	Carroll College Mathematics and Engineering Helena, MT 59625
NASA/JSC	
Directorate:	Mission Operations
Division:	Space Flight Training
Branch:	Systems Training
JSC Colleague:	Frank E. Hughes
Date Submitted:	July 24, 1996
Contract Number:	NAG 9-867

ABSTRACT

Astronaut training has traditionally been conducted at specific sites with specialized facilities. Because of its size and nature the training equipment is generally not portable. Efforts are now under way to develop training tools that can be taken to remote locations, including into orbit. Two of these efforts are the Field Deployable Trainer and Shared Virtual Reality projects.

Field Deployable Trainer

NASA has used the recent shuttle mission by astronaut Shannon Lucid to the Russian space station, Mir, as an opportunity to develop and test a prototype of an on-orbit computer training system. A laptop computer with a customized user interface, a set of specially prepared CDs, and video tapes were taken to the Mir by Ms. Lucid.

Based upon the feedback following the launch of the Lucid flight, our team prepared materials for the next Mir visitor. Astronaut John Blaha will fly on NASA/MIR Long Duration Mission 3, set to launch in mid September. He will take with him a customized hard disk drive and a package of compact disks containing training videos, references and maps.

The FDT team continues to explore and develop new and innovative ways to conduct off-site astronaut training using personal computers.

Shared Virtual Reality Training

NASA's Space Flight Training Division has been investigating the use of virtual reality environments for astronaut training. Recent efforts have focused on activities requiring interaction by two or more people, called shared VR. Dr. Bowen Loftin, from the University of Houston, directs a virtual reality laboratory that conducts much of the NASA sponsored research.

I worked on a project involving the development of a virtual environment that can be used to train astronauts and others to operate a science unit called a Biological Technology Facility (BTF). Facilities like this will be used to house and control microgravity experiments on the space station.

It is hoped that astronauts and instructors will ultimately be able to share common virtual environments and, using telephone links, conduct interactive training from separate locations.

INTRODUCTION

Astronaut training has traditionally been conducted at specific sites with specialized facilities. Core system training has taken place at JSC and payload and science related training has been conducted at other locations. This required significant amounts of crew travel. Because of its size and nature the training equipment is generally not portable. Efforts are now under way at NASA to develop training tools that can be taken to remote locations, including into orbit. These research efforts fall into to the general category of computer based training.

Computer based training can take many forms. At its most fundamental, the student plays a previously prepared lesson and reads, views, and/or listens to the course material. A slightly more advanced form of a computer based lesson would allow the student to interact with the course material using buttons, menus, and links. Even more advanced lessons would include "intelligent" software that simulates an instructor's actions.

Provided there are communication links, computer based training can include real time interaction between instructor and student. At its most advanced, this type of training would include realistic, virtual settings that allow several students and instructors, each in separate locations, to conduct interactive training within the same virtual environment.

I worked with two project teams this summer at JSC. Both projects involve computer based training. They are, however, very different in their focus. The Field Deployable Trainer project uses current and readily available hardware and software while the Shared Virtual Reality project is research oriented and uses sophisticated computers and peripherals.

FIELD DEPLOYABLE TRAINER

The Field Deployable Trainer (FDT) project was conceived as a way for astronauts to be able to train any time and anywhere. With the participation of many countries in the International Space Station (ISS), training activities are much more distributed than with the Space Shuttle program. More crew travel is required and, of course, training centers are now spread around the world.

In addition, space missions will be longer in duration on the ISS than they have been with the Shuttle. There will, therefore, be a greater need for refresher and just-in-time training which must take place on orbit. The goal of the FDT project is to develop a portable training platform that will allow astronauts to train when they are away from traditional training facilities.

Throughout the summer I learned to use a multimedia software called Director. I also became quite proficient at using Netscape and HTML, along with Director, to create visually appealing, interactive web pages. One of my roles with the FDT team was to help develop, using multimedia software, training lessons to be taken into orbit on upcoming

shuttle flights. We prepared a user interface, customized software, and compact disks for the NASA/MIR Long Duration Mission 3.

The Mir Space Station has a laptop computer with a compact disk drive. A hard disk drive, loaded with software and configured to meet flight requirements, will be installed by astronaut John Blaha when he arrives on board Mir. The compact disks, to be played on the laptop, were specially prepared for Mr. Blaha's mission. They contain digital training videos, maps, references, and various personal items.

The FDT team is continually working on ways to improve the quality and expand the content of the training lessons. Most of these efforts involve the use of off-the-shelf software and Pentium-level personal computers. These applications include hardware and software for capturing and editing videos, digital photography equipment, multimedia software for making interactive animated productions, the internet, and screen-design software for building graphical interfaces.

To increase the effectiveness of computer based training instructor/student interaction should occur. For this reason the FDT project is also focusing on communications technology. This includes the internet, telephone lines, and radio communication. One of the goals of the project is to develop effective procedures for ground-based computers to communicate, by radio, with orbiting laptops.

The FDT project is in the prototype phase, which will last for three years. It will then become a fully operational program.

SHARED VIRTUAL REALITY

The ultimate form of computer based training would allow the student (or several students) and their instructor to share a realistic, simulated environment in which they conduct their training. Virtual reality technology will be able to provide this type of training environment in the not-to-distant future.

NASA's Space Flight Training Division has been exploring the applications of virtual reality since 1990. A 1993 project involved the creation of a virtual training environment for the Space Shuttle mission (STS-61) to repair the Hubble Space Telescope. Dr. Bowen Loftin, from the University of Houston, directs the virtual reality laboratory that conducts much of the NASA sponsored research.

Recent NASA efforts have focused on activities requiring interaction by two or more people, called shared VR. Like all current virtual reality work, powerful computers with specialized graphics capabilities are required. (Dr. Loftin's laboratory uses Silicon Graphics Onyx machines.) Because interaction of the participants (who may be in different cities) is desired, shared VR also contains some complex communications issues. Hughes Training is working with Dr. Loftin's group on this aspect of the project.

I was involved with a project to develop a virtual environment that can be used to train astronauts, and others, to operate a science unit called a Biological Technology Facility (BTF). Facilities like this will be used to house and control microgravity experiments on the space station. The goal of this activity is to create a virtual world that simulates, visually and operationally, the unit's functions and surroundings. Two or more user should then be able to access and interact in the same virtual setting.

The long term goal is to create a training system where astronauts and instructors can share common virtual environments and, using communication links, conduct interactive training from separate locations.

APPLICATIONS BEYOND NASA

Computer based training has many applications outside NASA. One of the most obvious areas where CBT has great potential is in education.

Several projects under way at Dr. Loftin's lab involve the use of virtual reality in education settings. One of these is a virtual physics laboratory (called Newton's World) in which students are immersed in a virtual environment and observe the behavior of moving objects under various scenarios. Other projects involve training in surgical and military procedures.

At present, this technology is beyond the reach of most schools because of the hardware requirements and the expertise needed to develop the models and operate the equipment. This will change, however, as standard personal computers become more powerful and VR systems are developed for mass users.

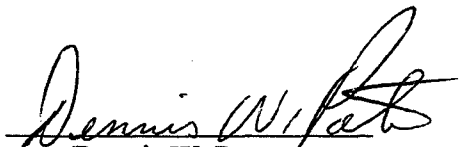
Many colleges are looking for ways to make course materials accessible to students in remote locations. The Field Deployable Trainer project has developed, using off-the-shelf software, platforms that can be used to deliver quality, interactive instruction to off-site students.

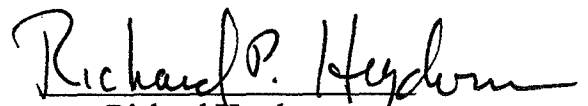
Because the software is inexpensive, relatively easy to learn, and can be used with readily available Pentium computers, I believe the techniques developed by the FDT team are ideal for developing computer based lessons for college courses. The lessons could then be accessed by resident students (through the campus network) or via the internet by off-site students.

**A HUMAN FACTORS ANALYSIS
OF
EVA TIME REQUIREMENTS**

Dennis W. Pate
Texas A&M University
NS3
August 16, 1996

Richard Heydorn
Analysis and Risk Assessment
Flight Systems Safety and Mission Assurance
Safety, Reliability, and Quality Assurance


Dennis W. Pate


Richard Heydorn

**A HUMAN FACTORS ANALYSIS OF
EVA TIME REQUIREMENTS**

Final Report
NASA/ASEE Summer Faculty Fellowship Program - 1996
Johnson Space Center

Prepared By: Dennis W. Pate

Academic Rank: Lecturer

University & Department: Texas A&M University
Engineering Technology Department
College Station, TX 77843
dpate@usa.net

NASA/JSC

Directorate: Safety, Reliability, and Quality Assurance

Division: Flight Systems Safety and Mission Assurance

Branch: Analysis and Risk Assessment

JSC Colleague: Dr. Richard P. Heydorn

Date Submitted: August 16, 1996

Contract Number: NGT-44-001-800

ABSTRACT

Human Factors Engineering (HFE) is a discipline whose goal is to engineer a safer, more efficient interface between humans and machines. HFE makes use of a wide range of tools and techniques to fulfill this goal. One of these tools is known as motion and time study, a technique used to develop time standards for given tasks. During the summer of 1995, a human factors motion and time study was initiated with the goals of developing a database of EVA task times and developing a method of utilizing the database to predict how long an EVA should take. Initial development relied on the EVA activities performed during the STS-61 (Hubble) mission. The first step of the study was to become familiar with EVAs, the previous task-time studies, and documents produced on EVAs. After reviewing these documents, an initial set of task primitives and task-time modifiers was developed. Data was collected from videotaped footage of two entire STS-61 EVA missions and portions of several others, each with two EVA astronauts. Feedback from the analysis of the data was used to further refine the primitives and modifiers used. The project was continued during the summer of 1996, during which data on human errors was also collected and analyzed. Additional data from the STS-71 mission was also collected. Analysis of variance techniques for categorical data was used to determine which factors may affect the primitive times and how much of an effect they have. Probability distributions for the various task were also generated. Further analysis of the modifiers and interactions is planned.

INTRODUCTION

International Space Station (ISS) will require unique procedures in the construction and maintenance of the facility. Never before has mankind attempted such an engineering and construction feat in such an alien environment. Many of these procedures will require extensive EVA missions. There have been several major studies performed to determine the amount of EVA time required in the construction phase of ISSA and in the operational phase (required maintenance). Many of the studies indicate EVA time will be a major issue.

For ease of maintenance, ISSA is being designed with components, orbital replacement units (ORUs), that are replaceable by astronauts performing EVAs or using remote manipulator systems. Both require the expenditure of valuable astronaut time. Tools are currently being developed to better predict the likely failure rate of the ORUs. The number of ORU failures will determine the number of EVAs required. Early studies to determine the amount of EVA time required to replace the ORUs have varied greatly in experimental design and in the findings. The variations between the studies is a direct result of the different methods people use to determine EVA time requirements. Currently, shuttle EVA timelines are developed by people with years of experience in the area of EVAs using their judgment to determine how the EVAs should be conducted and how long they should take. These estimates are further refined by hours of practice in the WETF and other facilities by the astronauts who will perform the EVA. A large portion of shuttle EVA timelines is attributed to overhead factors. The overhead is the non-productive time expended during an EVA mission. Planners regularly add between ten and thirty percent extra time to an EVA to account for individual differences and unexpected events. Even with this additional time, timelines are rarely met. This uncertainty in time makes predictions of future EVA time requirements difficult. To aid in analyzing the predicted EVA time required for a given task, a human factors analysis of EVAs was initiated. This paper will present the considerations that went into the human factors analysis of the EVA time requirements, the state of the current analysis of the Hubble mission, and the planned future activities.

DISCUSSION

Motion and Time Studies

Motion and time studies involve observing a task, whether in real time or recorded, and determining how long it takes to perform the basic movements of the task (known as "task primitives" in the EVA realm). The task primitives used in industry have undergone close to one hundred years of refinement. The Frank and Lillian Gilbreth were among the first people to perform motion and time studies on industrial activities. They developed a set of task primitives, known as Therbligs, that could be used to describe all the task performed by a worker. The Therbligs are divided into productive and non-productive

activities. This distinction allows the analyst to identify and eliminate waste within an operation. The primitives are useful both in the planning and in the analysis stages of a task. In planning, databases containing the standard times allowed for the various task primitives from prior motion and time studies can be used to predict how long a task should take. These predicted times can be adjusted for worker specific traits as well as environmental factors.

The unique environment of EVA precludes using the Therbligs in the analysis of EVAs. The Extravehicular Mobility Unit (EMU) the astronauts wear and the limited resolution of the videotape prevent viewing many of the visual queues an analyst of this system requires to determine what is going on. For these reasons, the basic system was modified to accommodate the EVA environment.

EVA Timeline Resources

A review of the NASA document database was conducted to locate EVA related materials that may have contained information useful in the development of the modified motion and time study system. None of the documents located were a complete source of EVA timelining information, however some did contain a few task primitives with their associated times as well as some general guidelines to be considered when developing a timeline. The main source of EVA information is the experience and intuition of the people working in the EVA area. Unfortunately, this experience and knowledge has yet to be collected into a single common EVA reference resource.

The Fisher-Price study, *Space Station Freedom External Maintenance Task Team: Final Report*, was one of the most comprehensive studies of EVA activities conducted to date. A motion and time study of task primitives performed in prior EVA missions and WETF training sessions was conducted as part of the study to determine how long it would take to perform certain key task. The task primitives were used to predict how long EVA maintenance missions would take. This study did not address the issue of modifiers effecting the task times.

The Mission Operations Directorate (MOD) training library contains two volumes of an EVA training manual entitled *EVA Lessons Learned*. The manuals contain observations from all of the past EVA missions and also includes a listing of EVA task primitives; however, the task primitives are taken directly from the Fisher-Price study.

Post-flight analysis of each mission are also available. These report how much time the major task required, but do not report the data at the task primitive level. They do provided a means of identifying the EVAs that did not meet the planned mission time. These could then be reviewed to determine what factors may have effected the times.

A copy of a post-flight EVA analysis report of STS-51A was obtained from the EVA office. The report included comparisons between task times in the WETF and the in-flight task times. The report also contained a listing of task primitives and their associated times. Some of the primitives included a general observation of possible modifiers.

Task Primitives

The Therbligs used in the traditional motion and time study were used as a starting point in developing the task primitives used in the EVA analysis. Some of these rely on being able to determine what the subjects looking at. This is not possible when viewing an astronaut within an EMU. The gold visor obscures their face during the day and the poor lighting and reflections obscure their face during the night. This also hinders determining what activities may be going on during a delay. Unavoidable delays, such as times when the astronaut are eating or drinking, cannot be distinguished from avoidable delays. The following is a list of the task primitives used in the initial study along with a brief description of the primitives:

- Adjust - the action of modifying a setting of a tool (powertool, foot restraint, etc...)
- Assemble - the action that occurs when two or more components are joined together.
- Delay - any time during which no work is occurring.
- Disassemble - the action that occurs when two or more components are taken apart.
- Grasp - the action of closing the fingers around an object.
- Hold - the action of supporting an object that is not being (dis)assembled or transported.
- Inspect - the action of visually checking an object to determine something about it.
- Operate - the action that occurs when work is being performed with a tool.
- Plan - the action of deciding what operation or task is to occur next.
- Position - the action of properly orienting and aligning an object.
- Reach - the action of moving a hand to or from an object.
- Rotate - the action of moving an articulating foot-restraint about its axis.
- Search - the action of locating an object.
- Select - the action of selecting one object from among a large number of objects.
- Tether - any action involving the use of a tether.
- Transfer - the action of transporting an object that is within the grasp of the astronaut.
- Translate - the action of moving from one position to another.
- Translate command - the action of communicating the desired RMS translation to the IV RMS operator.
- Verify - the required action of checking with the IV operators to ensure the proper tool setting or procedure.
- Wait - a delay due to someone else.

The tasks are further divided into different classes (e.g. Translate: manual, Translate: RMS, Tether: select, Tether: open, etc...). Further refinement of the primitives will likely become necessary as the analysis of the STS-61 and STS-71 data continues.

Task Time Modifiers

To increase the capability in predicting how long an EVA will take, one must have an understanding of the factors that may have an effect on the task times and what the effect will be. A list of factors effecting EVA times was developed from reviewing the lessons learned documents and other resources. Factors from the human factors field were added to these to develop the initial list used in the data collection and analysis of STS-61 (Hubble). In reviewing the EVA documents, the times given for the few task primitives listed were averages of observed times from past missions. The times did not include information on how to adjust the base task time for possible task modifiers nor did they indicate the distribution of the task times. Timeliners know from experience what factors they must take into account when assigning a time to a particular task.

The astronaut performing the EVA is one of the main sources of possible variation in the EVA system. The anthropometry (physical attributes) of the individual, their training, motivation, prior EVA experience, and mental ability will all have an effect on their ability to perform an EVA task. A 5th percentile female (i.e. given all the females in a population, 95% of the females will be larger in stature) will have different capabilities than a 95th percentile male (i.e. given all the males in a population, only 5% of the males will be larger in stature). There will be individual differences in stature, stamina, and strength. The intrinsic characteristics of the individual must be considered when predicting the time required to perform an EVA.

Related to this would be the posture the astronaut is in while performing the task. Some postures are biomechanically superior to others. Task times will be effected if the astronaut is in a twisted, extended, or otherwise contorted posture.

Another astronaut dependent factor would be the dominate side. Everyone has a dominant or preferred side (e.g. left or right). Task performed with the dominant side will be faster, more powerful, and more precise than those performed with the non-dominate side.

When analyzing a task time, one must consider the previous task(s) performed by the astronaut and the stamina of the astronaut. If the astronaut has just finished a labor intensive task or has been waiting on a reply from mission control, they may require more time to perform the next task. The longer they are into the mission, the more likely they are to slow down. The slow down may be offset, though, by the motivation factor. Studies presented by Wickens and by Siegal indicate operators placed under an increased level of stress, below a threshold limit, commit fewer errors and have faster response times. Based on comments from people involved in operational EVAs, this seems to be true for astronauts performing EVAs. When astronauts are informed they are behind on their schedule, they push themselves at a faster pace than they normally work.

The amount of training and the type of training an EVA astronaut receives will also affect the EVA time. Space station EVAs will not be practiced to the same degree shuttle EVAs are practiced due to time and monetary constraints. The effect the difference in training will have must be considered when predicting the time future EVAs will require. Ideally, a person should be trained until they reach the asymptote of their learning curve. This is the point where further training has no effect on the time required to perform the task. The training should continue till just prior to the mission. The longer the interval between their training and the actual performance of the task, the longer the in-flight task time will take due to recall problems and relearning. The STS-61 EVA missions were the most highly trained for EVA missions to date. This must be considered when including the data from this mission with the data from other missions. This mission also included many astronauts with prior EVA experience. This would increase the confidence of the astronaut as well as increase the value of the training they received prior to the mission. One must also be aware of the possible negative results of training; that is, actual task will require more time than the same task performed during training due to learning the wrong methods during training. An example of this would be material positioning task learned in the WETF. In the WETF, the water provides a damping action to the positioning task making it easier to stop the load than in orbit, yet it requires more force to start the object into motion. Another effect of training in the WETF leading to negative training is the pain induced by floating upside down. When the astronaut is upside down, their weight is supported by their collar bones resting on the bearing ring in the collar of the EMU. This leads astronauts to practice in a predominately heads-up manner. When in space, they may experiment with a heads-down attitude leading to a change in the planned activities and times.

The external lighting environment during the EVA will also affect some of the task times. When in sunlight, visually intensive task will be performed with greater ease. When out of the sunlight, lighting deficiencies become apparent and visual task will be hampered by the low light levels within the payload bay. During STS-61, the EVA astronauts required the IV crew to shine a spotlight through the orbiter window to provide more lighting for the task. Lighting induced psychological effects on the astronauts will also be possible. Some of the astronauts have commented that it is unsettling when you are on the RMS arm above the shuttle at night and everything except the shuttle is pitch black. The increased stress may also lead to some task being performed faster with fewer errors.

The thermal environment is also a function of the day and night conditions and will have an effect on the task times. During the night, the temperature will drop. As the temperature drops, the extremities, namely the fingers and hand, will cool at a faster rate than the bodies core. Conductive cooling that occurs while handling materials during the night can be severe enough to cause frostbite. Even a moderate cooling of the hands will cause a loss in the dexterity of the hands leading to an increase in the task times and an increased risk of accidents. Time will also be required to allow for the astronauts to don protective thermal mittens. The thermal mittens may no longer be required when the actively heated EVA gloves are manifested on futures flights. The changing thermal

environment can also cause equipment problems. PFRs may become difficult to ingress during the day when the boots and the PFR are thermally expanded. During the viewing of the Hubble mission, one of the astronauts had difficulty in ingressing a PFR attached to Hubble. The other astronaut had to interrupt his work to assist the ingress. In another incident, the astronaut could only ingress their right foot. Thermal vacuum chamber testing has helped to avoid the occurrence of thermal expansion and contraction problems, but they still need to be considered.

The restraint of the astronaut will also effect the time required to perform a task. A firmly restrained astronaut will be capable of using greater forces than one who is performing a task while free- floating. Tasks performed in these two different conditions must be differentiated.

The metabolic load the astronaut is under will also impact the task times. If an astronaut is under a heavy metabolic load, he will be producing large amounts of heat and CO₂ that must be removed by the EMU system. If they operate beyond the ability of the system, their body will respond by slowing them down to reduce the metabolic heat load and CO₂.

Some of the task times will be subject to modifiers unique to the task. While translating, factors such as encumbrance and obstacles must be considered. Direction of travel may also be important when looking at such things as rotational movements, and positioning tasks.

Interruption in the EVA activities can have a negative impact on task times. Story Musgrave describes EVA as a type of ballet. This is a useful and appropriate analogy to many tasks. Once you start the EVA/ballet, you enter a routine where everything starts to flow and you are thinking about the entire EVA/ballet as a whole, not just the next move. Whenever you interrupt the EVA/ballet, it will take some time to again get into the routine.

Data Collection

Videotapes of the entire STS-61 and STS-71 missions were obtained for analysis. These tapes included both onboard video (video recorded on tape recorders in the orbiter) and downlink video (video transmitted to mission control). Ideally the videotape to be analyzed included both the audio track and a time encoding. The audiotrack helped to determine the exact activity the astronaut was performing and determine what the pauses were for. Little useful information can be collected in the absence of the audio track. An essential tool used in conjunction with the audiotrack is the EVA timeline contained in the Flight Data File for the mission. The timeline allows one to know what is going on in the video and what operations are taking place. This also allows the analyst to know when the mission is deviating from the planned mission. The time encoding allows for the easy analysis of the time required to perform a task. It is possible to collect useful information in the absence of the encoding by using a stop watch to time the activities. This is cumbersome and does not allow for the slow motion analysis that is sometimes required to get a precise time.

The downlink video had a lower resolution than the onboard video, however, many of the onboard videos lacked either the audio tracks or time encoding. Initial data collection was performed using the downlink footage. This footage was taped in the order of the EVA missions and more attention had been paid to the focusing of the cameras on the activities that were being performed. Onboard videos were used to supplement the downlink videos when the astronauts were out of view in the downlink footage or the downlink was lost due to the lack of complete TDRS coverage. Even when making use of the two video sources, gaps in the coverage of a given EVA mission still exist.

The resolution and lighting of the videotapes is a problem in performing the motion and time study. At times the video image flares to white when the camera is over exposed with light and at times it fades to black when the light level drops when the camera is under exposed.

A studio quality tape player was used to play the tapes. The recorder allowed the speed of the tape to be controlled without a loss in the resolution of the image. This allowed speeding through portions of the video where there was no activity and slowing down for portions where there was a lot of activities occurring requiring close observation.

A spreadsheet to record the data was created using Microsoft Excel. An example of the resulting worksheet along with an explanation is included in the appendix. This information will allow for the analysis of the times required for the task primitives and for analyzing the effects of the possible modifiers. The database will be modified to reflect any lessons learned from the initial data collection performed on the STS-61 and STS-71 missions.

Analysis

Analysis of the data, using *JUMP* by the SAS Institute, is currently in progress. A summary of the current analysis is included in appendix A. An interesting finding was that several tasks were performed faster at night and the variation between times was also smaller than during the day. Tasks performed faster during the night are: Adjust PFR ($p=0.0893$), Tether to Object ($p=0.0735$), and Untether from Object ($p=0.0343$). There was a possible difference between missions in the time required to egress the PFR. There was no significant difference between the times required to egress the various types of foot restraints. There was a small difference between astronauts in the time required to disengage a bolt.

Significant task-time modifiers have yet to be identified for the remaining task. Further analysis will be performed in an attempt to identify the source(s) of the variation. As the size of the database is increased, the effect of the modifiers analyzed thus far may become significant.

In reviewing the data on observed errors, several areas of concern arise. The first is the problem with controlling small parts. In a contingency operation performed in an attempt to close the door on the Hubble, several washers were removed. The astronauts stored these small parts in their gloves and in a trashbag. Several parts were observed

floating free from the astronauts control. These parts could pose a severe risk to the astronauts and vehicles during that mission and future missions.

RMS operations were also a source of errors. The terminology used by the EV and IV astronauts in commanding RMS movements was not standardized. There were several times the commands were unclear or misunderstood. An example of the confusing commands was the use of the words "Left" and "Aft" by the astronauts. Phonetically these words are very similar. With the wide range of accents in the current astronaut corp and the international accents of the planned ISSA crew, care should be taken to determine the commands that will minimize the risk of confusing commands. Depending on how well the ISSA communication system works, this may become even more of a problem. The limited bandwidth of transmitted messages may increase the likelihood of command confusion. Another problem was the IV RMS operator failing to respond to the EV astronauts translate commands. The IV astronauts missed over 3 percent of the EV RMS translate commands.

Future Plans

Analysis of the currently collected data will continue. This will provide an insight into how the different task primitives should be handled and what types of adjustments will have to be made. Any necessary refinements to the system will also be made at this time. Additional data will also be collected from additional missions to study differences in task-times and error rates between missions. The predicted time for a given EVA task , constructed from the average task-times, will be compared to the actual time for the task in flight. Data will also be collected from the WETF training sessions with the hope of determining the correlation factors between WETF times and flight times.

ACKNOWLEDGMENTS

I would like to thank the following people for their assistance in this study:

Richard Heydorn	NASA
Pete Choban	Aerospace Corp.
Kent Castle	NASA
Bob Adams	NASA
Bob Bond	NASA
Mike Foale	NASA
Richard Fullerton	NASA
Amy, Kathy, & Silvia	Television and Photographic Services
Nancy & Vicky	MOD Library

ACRONYMS

EMU	extravehicular mobility unit
EVA	extravehicular activity
IV	intravehicular
ISSA	International Space Station Alpha
MFR	manipulator foot restraint
MOD	Mission Operations Directorate
PFR	portable foot restraint
PWS	portable work stanchion
RMS	remote manipulator system
TDRS	tracking and data relay satellite
WETF	weightless environment trainer

REFERENCES

Fisher, William F. & Price, Charles R., *Space Station Freedom External Maintenance Task Team, Final Report*, vol. I, parts 1-2, July 1990, NASA

Niebel, Benjamin W., *Motion and Time Study*, 8th ed., Homewood, IL: Irwin, 1988.

NASA, *EVA Lessons Learned*, vol. I, October 1994.

NASA, *EVA Lessons Learned*, vol. II, October 1994.

NASA, *STS-61 Flight Data File*

NASA, *STS-61 Videotape Scenelist*, JSC-25945-61

Siegal, Aurthur I. & Wolf, J. Jay, Wiley Series in Human Factors, *Man-Machine Simulation Models: Psychosocial & Performance Interaction*, Wiley Press.

Appendix A

TASK	N	Average (Std Deviation) MM:SS	Significant Modifiers
Adjust and Install PFR	1	3:54	None Identified (NI)
Adjust EMU Settings	2	0:12, 0:26	NI
Adjust Visor	6	0:10(0:05.6)	NI
Adjust, PFR Setting (1) Day	7	0:45(0:35)	Possibly faster at night (p=0.0893)
Adjust, PFR Setting (1) Night	8	0:23(0:05)	""
Assemble, Connectors	8	0:28(0:20)	NI
Assemble, Pip Pin	1	0:11	NI
Assemble, Powertool Extension	1	0:32	NI
Assemble, Velcro strap	1	0:07	NI
Close Storage door (lg)	1	0:07	NI
Close Thermal Cover (lg)	1	0:30	NI
Configure MWS after Object Xfer	1	1:34	NI
Configure PWS	4	0:52(0:26)	NI
Egress PFR	4	0:25(0:29)	Possible difference between missions.
Ingress Foot Restraint*	6	0:53(0:30)*	No significant difference between PFR and MFR
Ingress MFR	2	0:20, 0:77	NI
Ingress PFR	4		NI
Install (Engage) Bolt	30	$T(\text{sec})=16.3+1.58*(\text{turns})$	NI
Open Door (lg)	1	0:11	NI
Operate EMU Lights	11	0:15(0:08)	NI
Place Object in trashbag	1	0:13	NI
Remove (Disengage) Bolt	34	$T(\text{sec})=13.1+2.72*(\text{turns})$	There was a small significant difference between astronauts.
Remove ORU from Storage	1	1:28	NI
Remove Pip Pin	1	0:58	NI
Remove Thermal Cover	2	0:06, 0:07	NI

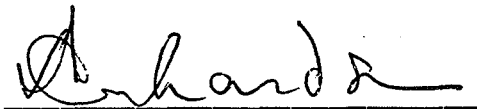
Appendix A

Replace Thermal Cover	2	0:09, 0:17	NI
Select MFR Control	10	0:04(0:003.5)	NI
Rotate MFR 45	28	0:05(0:03)	NI
Rotate MFR 90	11	0:10(0:09.8)	NI
Rotate MFR 135	12	0:12(0:06.7)	NI
Rotate MFR 180	6	0:09(0:03.7)	NI
Rotate PWS			
Select Powertool on MWS	7	0:12(0:14)	NI
Select Object from MWS	2	0:04, 0:15	NI
Stow ORU	2	0:43, 0:76	NI
Stow Powertool on MWS	24	0:18(0:12)	NI
Suit Status Callout	2	1:24, 1:43	NI
Tether to Object	34	0:19(0:11)	May be faster at night (p=0.0735).
Tether to Object, Day	18	0:22(0:13)	""
Tether to Object, Night	14	0:15(0:06)	""
Transfer Object	7	0:40(0:39)	
Transfer ORU	1	0:09	No tether Ops.
Transfer Tether	1	0:25	
Unassemble Connector	2	0:07, 0:30	
Unassemble PT Extension	1	0:27	
Untether Object (day)	12	0:15(0:09)	
Untether Object (night)	11	0:08(0:05)	Untether at night is significantly faster than day (p=0.0343)
Verify Connections	1	0:20/5	
Verify Part #	1	0:09	
Verify Procedure	2	0:14, 0:16	
Verify Tool Setting	31	0:23(0:18)	

SIMULATION OF THE PREDICTIVE CONTROL ALGORITHM FOR
CONTAINER CRANE OPERATION USING MATLAB FUZZY LOGIC TOOL
BOX

Albert O. Richardson
California State University, Chico
BT2
August 9, 1996

Robert O. Shelton
Information Technology Office
Information Systems Office
Business And Information Systems Directorate



Albert O. Richardson



Robert O. Shelton

**SIMULATION OF THE PREDICTIVE CONTROL ALGORITHM FOR CONTAINER
CRANE OPERATION USING MATLAB FUZZY LOGIC TOOLBOX**

**Final Report
NASA/ASEE Summer Faculty Fellowship Program-1996
Johnson Space Center**

Prepared by: Albert O. Richardson, Ph.D

Academic Rank: Professor

University & Department: California State University, Chico
Electrical & Computer Engineering
Chico, CA 95929-0888

NASA/JSC

Directorate: Business And Information
Systems

Division: Information Systems Office

Branch: Information Technology Office

JSC Colleague: Robert O. Shelton, Ph.D

Date Submitted: August 10, 1996

Contract Number: NAG 9-867

ABSTRACT

This research has investigated the use of fuzzy logic, via the Matlab Fuzzy Logic Tool Box, to design optimized controller systems. The engineering system for which the controller was designed and simulated was the container crane. The fuzzy logic algorithm that was investigated was the 'predictive control' algorithm. The plant dynamics of the container crane is representative of many important systems including robotic arm movements.

The container crane that was investigated had a trolley motor and a hoist motor. Total distance to be traveled by the trolley was 15 meters. The obstruction height was 5 meters. Crane height was 17.8 meters. Trolley mass was 7500 kilograms. Load mass was 6450 kilograms. Maximum trolley and rope velocities were 1.25 meters per sec. and 0.3 meters per sec., respectively. The fuzzy logic approach allowed the inclusion, in the controller model, of performance indices that are more effectively defined in linguistic terms. These include "safety" and "cargo swaying".

Two fuzzy inference systems were implemented using the Matlab simulation package, namely the Mamdani system(which relates fuzzy input variables to fuzzy output variables), and the Sugeno system(which maps fuzzy input variables to crisp output variable). It is found that the Sugeno FIS is better suited to including aspects of those plant dynamics whose mathematical relationships can be determined.

INTRODUCTION

Modeling and design of automatic controllers for complex systems is an important research activity for NASA. Examples of control systems relevant to NASA's operations are: a) rendezvous and docking of spacecrafts, and b) use of rovers to survey planets surface. Cost and developmental time constraints make highly desirable, rapid development of optimal controllers.

Conventional controllers yield accurate control for systems which match the linearized models of the system, and whose desired state is constant. In dealing with systems with time-varying parameters, unknown structures and multi-objects for control, conventional control design typically uses a very complex structured algorithm with the designer's knowledge. Unfortunately, re-constructions of the controller, due to sub-system alteration or change of system structure, requires the designer to engage in a complete remodeling of the system.

Recently, there has been considerable interest in the use of fuzzy logic control methodologies. These have been demonstrated to offer possibilities for the control of plants having uncertain and unpredictable dynamics, such as is obtained in the container crane operation under conditions of wind and cargo variations. The research explores the use of "predictive" fuzzy logic control algorithm for control of the container crane[1,2]. The algorithm is simulated using the Matlab Fuzzy Logic Tool Box. The importance of the container crane system is that its dynamics are similar to robot systems. The container hoist and trolley motors are analogous to robot shoulder and elbow motors. Both systems must move varying payloads from one point to another in minimum time.

The container crane operation is divided into two simultaneous functions. One is the trolley operation, which commands the trolley target velocity, and moves and stops the trolley at the pre-determined position. The other is the wire rope operation, which commands the container hoisting or lowering target velocity, and regulates the rope length.

PREDICTIVE FUZZY CONTROL AND THE CONTAINER CRANE

A. Control Strategy For Optimum Performance

At any given instant, the following sequence of actions take place:

1. Evaluate the system states.
2. Based on required target states, predict control results from the different control rules.

3. Select the most likely control rule derived from skilled human operator experiences.

B. Performance Indices of Interest .

The performance indices of interest are:

a) Safety: ----Height clearances between the cargo trajectory and the body of the ship or the piled containers, and the trolley position.

b) Stop-gap accuracy: ---- Difference between predicted stop position and target stop position. Judging of trolley speed is important for determining stop-gap

c)Maintained sway:----By accelerating or decelerating between characteristic cycle times determined by the rope length, trolley and cargo masses, acceleration and deceleration of a non-swaying load is possible. The acceleration and deceleration and times are ascertained along with the trolley speed.

d)Carrying time:---- Time taken to move cargo from the start point to the target point. The obstruction sections and their heights(danger zone) along the way which the cargo must cross safely, must be known ahead of time.

C. The Methodology of Predictive Control:

The fuzzy controller periodically evaluates the efficiency of linguistic control rules such as " if the performance index, x , is A_i and index, y , is B_i , when a control command, u , is decided to be C_i at the present time, then this control rule is selected and the control command , C_i , is decided to be the output.

(i) the control rules, $R(R_1, R_2, \dots, R_n)$ are described as " R_i : if(u is $C_i \rightarrow x$ is A_i and y is B_i), then u is C_i ",

(ii) the control rule, R_j , is selected from the predictive results(x, y) indicating the highest likelihood, and

(iii) the control command, C_j , is decided as the controller output.

The linguistic control rule is formulated as:

R_i : "if u is $C_i \rightarrow x$ is A_i and y is B_i , then u is C_i ."

D. Trolley Operation:

This section details out the crane operation strategies that a skilled human operator uses. It therefore forms the expert knowledge base upon which the automated trolley controller is based.

Trolley movement is divided into SEVEN DOMAINS(P0-P6):

P0-----Start

P1-----Acceleration

P2-----Constant Speed Control

P3-----Deceleration

P4-----Stop

P5----Correcting(Inching) trolley position around target stop position

P6----Lowering the Cargo

Trolley operation is divided into two function levels. One is decision level, in which the present domain of the trolley operation is decided. The other is the activation level, in which the target trolley velocity and the acceleration force are commanded.

(1) Trolley decision level

The timing for switching the domain is affected by the initial sway, the wind and the rope length, which are operated independent of the trolley. These timing changes are given below. Refer to conditions for changing domains based on the predictive control strategy outlined in section C above.

(T-1) In the start domain, when the acceleration control is started by an operator under conditions of the present rope length and trolley position, if the trolley is accelerated to a maximum speed in terms of safety and a small maintained sway, then the acceleration control is started. (P0--->P1)

(T-2) When the acceleration control terminates and the trolley reaches the maximum speed, then the operation domain is shifted to the constant speed control domain. (P1--->P2)

(T-3) In the constant speed control domain, when the deceleration control is started by an operator under these trolley speed, trolley position and rope length conditions, if the trolley is stopped beyond the target position at the small maintained sway, then the deceleration control is started. (P2--->P3)

(T-4) When the deceleration control is ended by an operator and the trolley speed reaches the lower speed, then the operation domain is shifted to the stop domain. (P3--->P4 and P5--->P4).

(T-5) After a few seconds in the stop domain, if the trolley stops and the stop gap between the trolley and target position is large, then correction control is started. (P4--->P5)

(T-6) After a few seconds in the stop domain, if the trolley stops near the target position, then lowering control is started. (P4-->P6)

(2) Trolley activation level

In any given situation the domain that gets applied or activated is determined by the trolley decision level mentioned above. At the activation level, the domains are applied as described below:

- (C-1) In the start domain(P0), the trolley speed is held to zero.
- (C-2) In the acceleration domain(P1), the method of acceleration control determined at the last start domain(P0) is performed.
- (C-3) In the constant speed control domain(P2), the trolley speed is held at the maximum trolley speed.
- (C-4) In the deceleration domain (P3), the method of deceleration control determined at the last constant speed control domain(P2), is performed.
- (C-5) In the stop domain (P4), the trolley speed is held to zero.
- (C-6) In ther correcting domain (P5), the trolley is moved toward the target position.
- C-7) In the lowering domain (P6), the trolley speed is held at zero.

E. Wire Rope Operation.

Two function levels: (i) decision level, in which target rope length is decided; and (ii) activation level, in which target rope velocity is commanded.

(1) Rope decision level.

Hoisting or lowering of cargo determined by cargo(trolley) position.

- (R-1) Before reaching a danger zone, the cargo is hoisted to a safe rope length which permits the cargo to pass overhead.
- (R-2) In the danger zone, the rope length is held at the safe rope length.
- (R-3) After passing over the danger zone, the cargo is lowered to a target rope length which is determined by the final target rope length and subsequent obstruction height.
- (R-4) The cargo is stopped near the target point and is lowered to the final target height.

(2) Rope activation level

Target rope velocity is commanded according to present rope length and determined target rope length, taking the hoist motor specifications into consideration.

F. Design of Predictive Fuzzy Controller for the ACO.

(1) Controller Inputs

There are two groups of inputs to the controller. One group of input variables to the controller represents the state of the controlled system.

These are:

- x'-----trolley velocity; x-----trolley position;
- l-----rope length

Another group of inputs to the controller is the group of performance indices, which is used in the predictive control model to select the most likely control rules for accomplishing the control objective and to meet the prescribed performance indices. These are: safety, stop-gap accuracy, minimum container sway, and minimum carrying time.

(2) Controller Outputs

Controller outputs are: Target velocity of trolley(V_T), Target velocity of rope system(V_1), Brake command force of trolley(B_T), Brake command force of rope system(B_1), Maximum traction force to trolley(F_m).

(3) Controller Performance Indices as Fuzzy Sets.

Since the performance indices are expressed using human linguistic forms, they are particularly suitable for representation as fuzzy sets which are defined below, and whose membership functions will be fully defined subsequently.

Trolley Position(S):

Hoisting zone(XC), Danger zone(XD), Lowering zone(XE)

Trolley Position at target Point(Stop-Gap Position)(G).

Bad stop(XB), Good stop(XG), Beyond-target position(XT)

Trolley Velocity(W):

High trolley speed(VM), Low trolley speed(VL)

Trolley velocity at Stop-gap position(G):

Zero trolley speed

Performance Index----Cargo Safety Height(S)

Height danger(HD), Height safe(HS)

Performance Index----Sway time(W)

Acceleration end(AE), Deceleration end(DE)

Performance Index----Carrying time(P)

P0-P6

G. Predictive Model

The predictive models enable us to predict (1) the height clearance and (2) stop position.

(1) Height clearance

The height clearance between the trajectory and the ship's body or piled containers is calculated by the acceleration-influenced cargo trajectory which is dependent on both the present trolley position and rope length.

(2) Predicted stop position

The predicted stop position (X_p) is calculated by

$$X_p = X + (V_t * T_d) / 2 \quad (1)$$

where X is the trolley position, V_t is the trolley velocity and T_d is the deceleration time interval.

H. Fuzzy Control Rules.

The rules of operational experience outlined previously are converted into fuzzy control rules.

(1) Trolley fuzzy decision rules

Taking the case of decision rule (T-3) as an example, each phrase of the "experience rule"(T-3) is rewritten as follows:

In the constant speed control domain ----> P is P2.

The deceleration control is started by an operator ---> t_3 is t and $t_4=t+T_d$.

The trolley is stopped by an operator beyond the target position respectively----> G is XT.

In the small maintained sway ----> $F_d=F_m$,

where t_3, t_4 are the start and end times of the deceleration control P3, t is the present time, F_d is the deceleration force, and F_m is a deceleration or acceleration force of a non-swaying load.

The decision level rules are therefore summarized as follows:

(T-3) If P is P2 and ($t_3=t$ and $t_4=t+T_d$ and $F_d=F_m$ --->G is XT), then $t_3 =t$ and $t_4=t+T_d$ and $F_d=F_m$.

(T-1) If P is P0 and ($t_1=t$ and $t_2=t+T_d$ and $F_a=F_m$ --->S is HS), $t_1=t$ and $t_2=t+T_d$ and $F_a=F_m$

(T-2) If P is P2 and W is AE W is VM, then $t_2 =t$,

(T-4) if P is P4 and W is DE and W is VL, then $t_4=t$ and $t_5=t+3.0$,

(T-5) If P is P5 and G is VZ and G is XB, then $t_5=t$,

(T-6) If P is P5 and G is VZ and G is XG, then $t_6=t$,

where t_1, t_2 are start and end times, respectively, of the acceleration control P1, T_a is the acceleration time interval, F_a is the acceleration force, t_5 is the start time of the correcting control P5, and t_6 is the start time of the lowering control P6.

(2) Trolley fuzzy activation rules

(C-1) If P is P0, then $V_T=0$

(C-2) If P is P1, then $V_T=2V$ and $F=F_a$

(C-3) If P is P2, then $V_T=V$

(C-4) If P is P3, then $V_T=-V$ and $F=F_d$,

(C-5) If P is P4, then $V_T=0$,

(C-6) If P is P5, then $V_T=X_T-X$,

(C-7) If P is P6, then $V_T=0$,

where V_T is the target trolley velocity, V is the maximum trolley velocity, F is the trolley motor force and X_T is the horizontal target position.

I. Rope operation

(1) Rope fuzzy decision rules

- (R-1) if S is XC and P is <P6, then $h=L_s$,
- (R-2) If S is XD and P is <P6, then $h=L_s$,
- (R-3) If S is XE and P is <P6, then $h=L_n$,
- (R-4) If P is P6, then $h=L_b$

where h is the target rope length, L_s is the minimum rope length, L_n is the safety rope length between X and X_T , and L_b is the target(final) rope length.

(2) Rope activation rules

The target rope velocity is regulated by proportional control, based on target and actual rope length references.

J. Realization of Fuzzy ACO Controller

The computation flowchart for realizing the fuzzy controlled ACO is shown below. In the system, following a depart signal, both the decision level phase and the activation level phase are executed periodically, say 100ms and 10ms respectively.

I. Example Calculations For Container In Reference 1.

Container Specs:

Crane Height, L_c	17.8[m]
Max. Trolley Vel, V	1.25[m/s]
Max. Rope Vel., V_r	0.3[m/s]
Trolley Mass, M_{Tr}	7500[kg]
Load Mass, M_{load}	6450[kg]

Data and Calculated Parameters For a Particular Case:

Total Distance Travelled by Trolley, X_T ,	15[m]
Obstruction Height, L_o ,	5[m]
Acceleration Time, T_a ,	5[sec]
Constant Velocity Time, t_3-t_2	11[sec]
Deceleration Time, T_d ,	6[sec]
Cargo Raising(Hoist) Time, t_1	13[sec]
Cargo Lowering(Hoist) Time, t_7-t_6	7[secs]
Swaying Time at Destination, t_s	4[secs]
Total Trolley Travel Time, T_t	22[sec]
Total Carrying Time , T_c	46[sec]
Mean Carrying Time Human Operator, M_{ho}	51.7[sec]
Mean Stop Gap for Human Operator, L_{gh}	5.6[cm]

Mean Sway for Human Operator, L_{sh}	10.8[cm]
Mean Carrying Time for ACO, T_{maco}	47.0[sec]
Mean Stop Gap Error for ACO, L_{mgaco}	1.9[cm]
Mean Maintained Sway for ACO, L_{msaco}	5.7[cm]
Minimum Rope Length, L_s ,	12.8

Equations of Motion of The Trolley:

Time $t_0 < t < t_1$, Cargo Raise, $V_t = 0$ (1)

Time $t_1 = 0$ sec.

Time $t_1 < t < t_2$, Acceleration, $V_t = a * t$ (2)

$X = (V_t * t) / 2 = (a * t^2) / 2$ (3)

At $t = t_2$ $V_t = V_T$ (4)

$X = (a * T_a^2) / 2$

Time $t_2 < t < t_3$, Constant Vel. Region, $V_t = V_T = a * T_a = a * (t_2 - t_1)$ (5)

At $t = t_3$, $V_t = V_T$

Time $t_3 < t < t_4$ $T_d = t_4 - t_3$ (6)

$V_t = V_T - a * (t_4 - t_3) = V_T - a * T_d$ (7)

$X = (a * T_a^2) / 2 + a * T_d$

Time $t_4 < t < t_5$ $V_t = V_T - a * T_d - a * (t_5 - t_6)$ (8)

Equations of Motion of The Hoist Motor

Moving velocity of rope is constant at 0.3[m/s]

RESULTS AND CONCLUSIONS

So far a mamdani and sugeno fuzzy inference systems(FIS) have been designed and simulated with incorporation of linguistically defined variables such as 'safety' as it breaks down into safety zone, and danger zone. The designed and simulated controller for the Sugeno fuzzy inference system for the container is listed below.

The Sugeno FIS:

[System]

Name='cont_crane_sugeno'

Type='sugeno'

NumInputs=7

NumOutputs=2

NumRules=10

AndMethod='min'

OrMethod='max'

ImpMethod='min'

AggMethod='max'

DefuzzMethod='centroid'

[Input1]

Name='safety'

Range=[0 5]

NumMFs=2

MF1='hd': 'trapmf',[0 0 1.7 3]

MF2='hs': 'trapmf',[2.5 3.3 5 5]

[Input2]

Name='position'

Range=[0 50]

NumMFs=3

MF1='xc': 'trapmf',[0 0 10 22.5]

MF2='xd': 'trapmf',[10 20 30 40]

MF3='xe': 'trapmf',[27.5 40 50 50]

[Input3]

Name='stopgap_position'

Range=[-1 1]

NumMFs=2

MF1='xg': 'trapmf',[-1 -0.2 0.2 1]

MF2='xt': 'trapmf',[-1 -0.6 1 1]

[Input4]

Name='stopgap_velocity'

Range=[-2 2]

NumMFs=1

MF1='vz': 'trapmf',[-1.8 -0.2 0.2 1.8]

[Input5]

Name='sway_time'

Range=[0 10]

NumMFs=1

MF1='ae(de)': 'trapmf',[5 7.5 10 10]

[Input6]

Name='sway_velocity'

Range=[0 3]

NumMFs=2

MF1='vl': 'trapmf',[0 0 0.4 2]

MF2='vm': 'trapmf',[0.4 2 3 3]

```
[Input7]
Name='carrying_time'
Range=[0 50]
NumMFs=7
MF1='p0':trapmf,[0 0 5 7.5]
MF2='p1':trapmf,[0.8335 7.5 14 15.83]
MF3='p2':trapmf,[9.165 15.83 22 24.16]
MF4='p3':trapmf,[17.5 24.16 28 32.5]
MF5='p4':trapmf,[25.84 32.5 37 40.84]
MF6='p5':trapmf,[33 37 42.5 49.16]
MF7='p6':trapmf,[42.5 43 50 50]
```

```
[Output1]
Name='trolley_vel'
Range=[-3 3]
NumMFs=7
MF1='carry_time_p0':constant,0
MF2='carry_time_p1':linear,[0 0 0 0 0 0 0.2 0]
MF3='carry_time_p2':constant,0
MF4='carry_time_p3':linear,[0 0 0 0 0 0 -0.2 0]
MF5='carry_time_p4':constant,0
MF6='carry_time_p5':linear,[0 0 0 0 0 0 .01 0]
MF7='carry_time_p6':constant,0
```

```
[Output2]
Name='rope_length'
Range=[0 20]
NumMFs=2
MF1='hoist_length':constant,12.8
MF2='lowering_length':constant,17.8
```

```
[Rules]
0 0 0 0 0 0 1, 1 0 (1) : 1
0 0 0 0 0 0 2, 2 0 (1) : 1
0 0 0 0 0 0 3, 3 0 (1) : 1
0 0 0 0 0 0 4, 4 0 (1) : 1
0 0 0 0 0 0 5, 5 0 (1) : 1
0 0 0 0 0 0 6, 6 0 (1) : 1
0 0 0 0 0 0 7, 7 0 (1) : 1
0 1 0 0 0 0 0, 0 1 (1) : 1
0 1 0 0 0 0 0, 0 1 (1) : 1
0 3 0 0 0 0 0, 0 2 (1) : 1
```

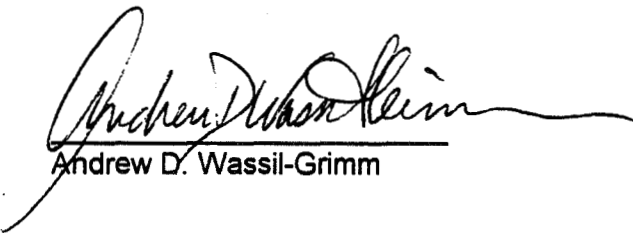
REFERENCES

- [1] Yasunobu, S., and Hasegawa, T., "Evaluation of an Automatic Container Crane Operation System Based on Predictive Fuzzy Control", Control Theory And Advanced Technology, Vol.2, No.3, pp419-432.
- [2] Yasunobu, S., and Miyamoto, S., "Automatic Train Operation System by Predictive Fuzzy Control", Industrial Application of Fuzzy Control, M. Sugeno(ed)., Elsevier Science Publishers, 1985, pp.1-18.

Database Development
for
Electrical, Electronic, and Electromechanical (EEE) Parts
for the
International Space Station Alpha

Andrew D. Wassil-Grimm
West Virginia University at Parkersburg
JSC Mail Code: OB
August 9, 1996

Patrick S. Pilola
Design Integration Team,
Systems Engineering and Analysis Section,
Systems Integration Branch,
Vehicle Division,
International Space Station Alpha Program Office


Andrew D. Wassil-Grimm


Patrick S. Pilola

**DATABASE DEVELOPMENT FOR ELECTRICAL, ELECTRONIC, AND
ELECTROMECHANICAL (EEE) PARTS FOR THE
INTERNATIONAL SPACE STATION ALPHA**

**Final Report
NASA/ASEE Summer Faculty Fellowship Program—1996
Johnson Space Center**

Prepared by:	Andrew D. Wassil-Grimm
Academic Rank:	Associate Professor
University & Department:	West Virginia University at Parkersburg Technology Division Parkersburg, WV 26101
NASA/JSC	
Directorate:	Systems Integration
Division:	Systems Engineering & Analysis
Branch:	Design Integration
JSC Colleague:	Patrick S. Pilola
Date Submitted:	August 9, 1996
Contract Number:	NAG 9-867

ABSTRACT

More effective electronic communication processes are needed to transfer contractor and international partner data into NASA and prime contractor baseline database systems. It is estimated that the International Space Station Alpha (ISSA) parts database will contain up to one million parts each of which may require database capabilities for approximately one thousand bytes of data for each part. The resulting gigabyte database must provide easy access to users who will be preparing multiple analyses and reports in order to verify as-designed, as-built, launch, on-orbit, and return configurations for up to 45 missions associated with the construction of the ISSA. Additionally, Internet access to this data base is strongly indicated to allow multiple user access from clients located in many foreign countries.

This summer's project involved familiarization and evaluation of the ISSA Electrical, Electronic, and Electromechanical (EEE) Parts data and the process of electronically managing these data. Particular attention was devoted to improving the interfaces among the many elements of the ISSA information system and its global customers and suppliers. Additionally, prototype queries were developed to facilitate the identification of data changes in the data base, verifications that the designs used only approved parts, and certifications that the flight hardware containing EEE parts was ready for flight. This project also resulted in specific recommendations to NASA for further development in the area of EEE parts database development and usage.

INTRODUCTION

Historically, NASA has been able to acquire human-space-flight qualified electrical, electronic, and electromechanical (EEE) parts through the military supply system. As the defense contractor manufacturing base has declined, it has become more difficult to purchase already qualified parts which satisfy the performance specifications thus requiring NASA to perform some part qualifications themselves and to establish a new parts management approach. As a result, the International Space Station Alpha (ISSA) Parts Control Board (PCB) Analysis and Integration Team (AIT) selected EPIMS (EEE Parts Information Management System), which is a NASA-wide parts management system, as their baseline system because it was already operational and eliminated the need to create their own database. The EPIMS is managed by Goddard Space Flight Center (GSFC) in Greenbelt, Maryland.

Even though EPIMS is currently capable of accepting data in various formats, the huge volume and uniqueness of the data from ISSA contractor, International Partner, and the precursor Space Station Freedom Program required that the ISSA data be translated, reformatted, and then loaded onto Johnson Space Center's local EPIMS server before the GSFC EPIMS administrator could bulk load the data into the EPIMS database. An additional complexity is that electronic interfaces between EPIMS and the ISSA's PALS (Program Automated Library System) and VMDB (Vehicle Master Data Base) needed to be established so that subsystem parts' lists could be loaded into the VMDB and EEE parts documents. This is required so that the ISSA quality specifications and approved parts lists could be assessed by the International Partners and NASA contractors in their design and operations efforts.

This technical situation, coupled with the extremely heavy workload on the understaffed GSFC EPIMS administrator making it essentially unavailable, led to the decision to develop an ISSA EEE parts database. The primary task of this development effort was to build/establish more effective electronic processes for transferring contractor and International Partner data into the ISSA baseline database systems (EPIMS, PALS, RTM [Requirements Tracability Manager], IMDS [Item Management Database System], and the VMDB.)

The EEE parts database development plan was to begin with a requirements review, proceed to a capabilities search for an adaptable database system, followed by development of some specialized software and database procedures and culminate in testing of the database system. The underlying research aspect of this effort involved the search for and development of the means and procedures to create an electronically-based configuration management system for the ISSA's EEE parts.

ISSA EEE PARTS DATABASE DEVELOPMENT

The uses for the EEE parts database were twofold: (1) facilitate verification of the design and certification of the built hardware for launch, and, (2) facilitate input of EEE parts data into the VMDB. There were approximately 240 fields or data entries associated with the EEE parts database not all of which were for each individual EEE part for the ISSA. A tabalized organization of these data items is shown in Figure 1.

Vehicle_Indentured_Parts_List	Standard_EEE_Parts_List	Stress_Analysis_Approval_Status
Record_ID	Record_ID	Record_ID
Assembly	CAGE_Code	Approval_Status
Certification_Status	Comment_#	Comments
CI/CEI_Number	FSC	Contractor_Approved_By
Comments	Generic	Contractor_POC
Contractor_POC	Grade	Document_Number
Element	Manufacturer	Program_Approved_By
H/W_Code	Materials_&_Processes_Information	Status_Date
Launch_Sequence_Rev/Date	Part_Description	VIPL_Equipment_Part_Number
LP/S	Program_POC	
ORU	Qualification_Status	System_Application_Analysis_Approval
Program_POC	Radiation_Record_Number	Record_ID
Status_Date	Spec_Rev_at_Qualification	Approval_Status
Subcontractor	Specification_Number	Comments
Subelement	Specification_Part_Number	Document_Number
Subsystem	Status_Date	Program_Approved_By
System		Status_Date
Verification_Status	Radiation_Data_1	VIPL_Equipment_Part_Number
VIPL_Equipment_Description	Record_ID	
VIPL_Equipment_Part_Number	Comment_#	Equipment_Using_Grade_2_Parts
SSQ_Revs	Computed_SEU/SEL_Rate_Summary	Record_ID
Record_ID	Manufacturer	Approval_Forum
Comments	Maximum_Analyzed_Total_Dose	Approval_Memo_Number
CRs_Incorporated	Part_Description	Approval_Status
Program_POC	Program_POC	Approval_Supporting_Data
Release_Status	Radiation_Record_Number	Comments
Revision	Report_#	Contractor_Approved_By
Specification_Number	Status_Date	Contractor_Contract_Letter_Number
Title	Technology	Contractor_Supporting_Data_List
	Test_POC	Program_Approved_By
	Tested_Lot_Date_Code	Status_Date
	Tested_Part_Number	VIPL_Equipment_Part_Number

Figure 1.- Tablized Organization of EEE Parts Data Items....continued on next page

As-Built_Parts_List	GIDEP_Hits_& Assessments	Points_of_Contact_List
Record_ID	Record_ID	Record_ID
Approval_Status	CAGE_Code	Name
CAGE_Code	Comments	Address
Comment_#	Contractor_Assessment	Company
Contractor_Contract_Letter_Number	Contractor_Status	Mail_Stop
Lot_Date_Code	Contractor_Status_Date	City
Program_Approved_By	GIDEP_Number	State
Reference_Designator	Manufacturer	Zip
Specification_Part_Number	Program_Approved_By	Country
Status_Date	Program_Assessment	Phone_Number
Std/N	Program_Status	FAX_Number
VIPL_Equipment_Part_Number	Program_Status_Date	E-Mail_Address
	Specification_Part_Number	Org
	Status_Date	Org_Code
	VIPL_Equipment_Part_Number	Overnight_Address
As-Designed_EEE_Parts_List		Overnight_Mail_Stop
Record_ID	NSPAR_Status	Overnight_City
Approval_Status	Record_ID	Overnight_State
CAGE_Code	Approval_Status	Overnight_Zip
Comments	CAGE_Code	Overnight_Country
Contractor_Approved_By	Comment_#	Notes
Contractor_Contract_Letter_Number	Contractor_Approved_By	
Program_Approved_By	Contractor_POC	Supplier_Survey_Status
Quantity_per_assembly	FSC	Record_ID
Reference_Designator	Generic_Number	Approval_Status
Specification_Part_Number	Grade	CAGE_Code
Status_Date	Manufacturer	Capability_&_Specifications
Std/N	NSPAR_Number	Comments
VIPL_Equipment_Part_Number	Part_Description	Contractor_POC
	Program_Approved_By	FSC
GIDEP_Data	Radiation_Record_Number	Program_POC
Record_ID	Spec_Rev_at_Qualification	Report_Approval_Date
CAGE_Code	Specification_Number	Report_Contractor_Approved_By
Comments	Specification_Part_Number	Report_Program_Approved_By
FSC	Status_Date	Report_Approval_Status
Generic_Number	Qualification_Status	Status_Date
GIDEP_Date	VIPL_Equipment_Part_Number	Supplier_Type
GIDEP_Description		Supplier_Name
GIDEP_Number	OTS_Equipment_Status	Plant_Address
GIDEP_Text	Record_ID	Plant_City
GIDEP_Title	Approval_Forum	Plant_State
Lot_Date_Code	Approval_Memo_Number	Plant_Zip
Manufacturer	Approval_Status	Plant_Country
Part_Description	Approval_Supporting_Data	Supplier_POC
Specification_Number	Comments	Mailing_Address
Specification_Part_Number	Contractor_Approved_By	Mailing_City
Status_Date	Contractor_Contract_Letter_Number	Mailing_State
	Contractor_Supporting_Data_list	Mailing_Zip
	Program_Approved_By	Mailing_Country
	Status_Date	
	VIPL_Equipment_Part_Number	

Figure 1.- (Continued) Tablized Organization of EEE Parts Data Items

It was estimated that on the order of one million EEE parts will be used in the ISSA when considering each separate usage of the parts. The EEE parts database needed to be easily populated from input sources utilizing Microsoft, Oracle, Macintosh, and other software systems as well as some paper sources not supported by computer systems. Additionally, change control and data pedigree information must be kept for each data record. To this end, the database system needed to be easily searchable and provide for the comparison of data sets to determine which information has been changed or does not match other comparison criteria. Also, the EEE parts database must be a relational one and allow normalization processes in order to ensure efficiency.

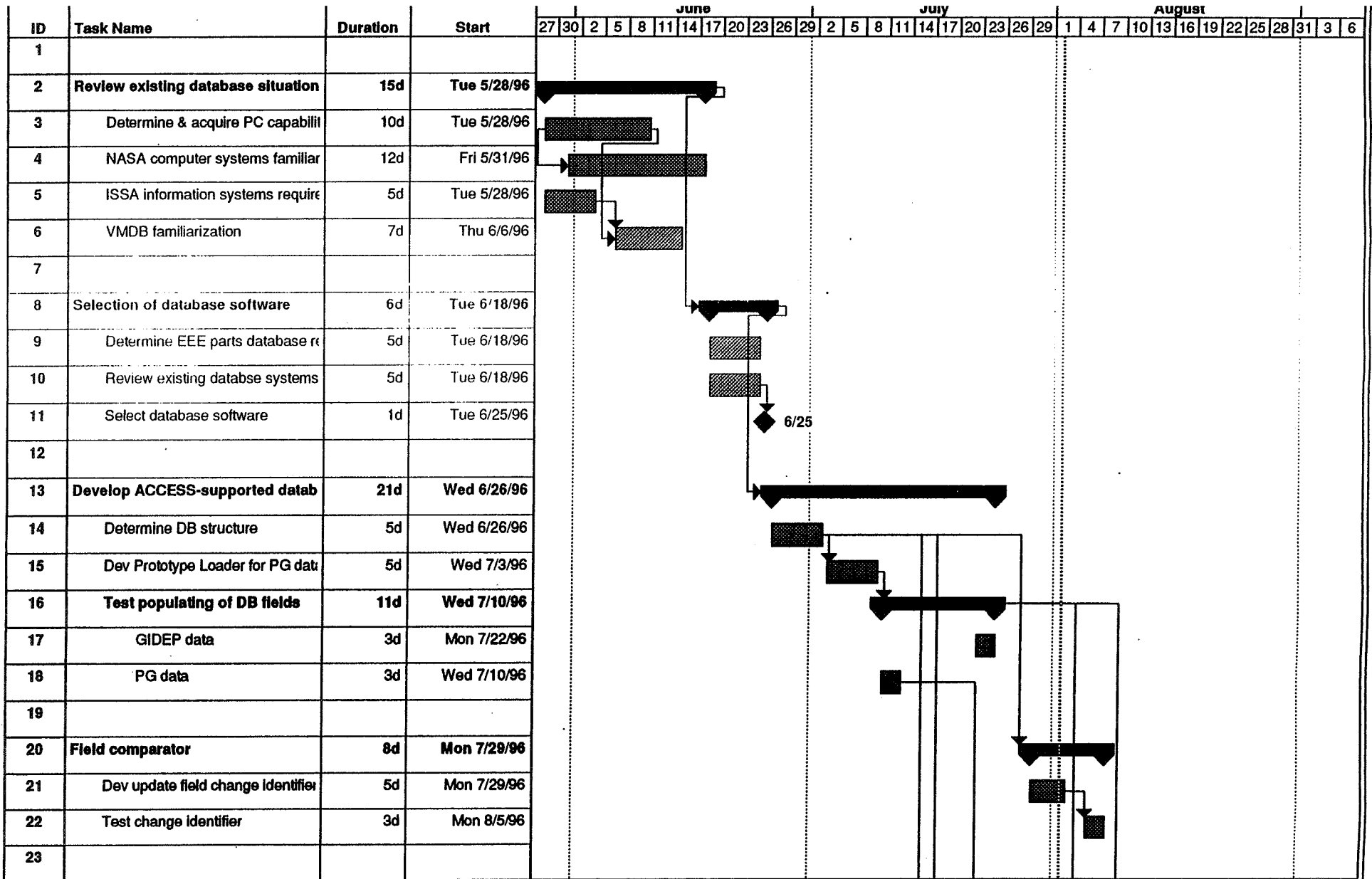
The search for database management software quickly resulted in selection of Microsoft's Access based on its capacity, flexibility, adaptability, maturity, supportability, availability, and confidence the EEE database developers had in it. Since the database was to be used primarily by the ISSA prime (integrating) contractor—Boeing—during the assembly phase of the ISSA and by NASA later, a user friendly and widely available software package was considered to be the best choice. Also, the Access program has the capacity to allow development and use of macros which would be needed to efficiently perform the needed functions of this database.

The schedule shown at Figure 2 illustrate the plan that was utilized to conduct the EEE parts database development.

The NASA/JSC computer/information system utilized by the ISSA is relatively mature and consists of several local area networks which have interconnectability with each other and with the NASA-wide system as well as the Internet. The ISSA home page is accessible from the Internet and is broken into a public access portion and a privileged portion requiring user id and password authorizations. This network system is very heavily relied upon by NASA engineers and managers and is the conduit for almost all program information.

The VMDB is part of the ISSA information system and is the database which contains all official space station technical data or links to other databases such as engineering drawings. Figure 3 shows the architecture of the VMDB.

27-7



Project: EEE Parts DB development Date: Fri 8/2/96	Task		Summary		Rolled Up Progress	
	Progress		Rolled Up Task			
	Milestone		Rolled Up Milestone			

Figure 2.- EEE Parts Database Development Plan....continued on next page

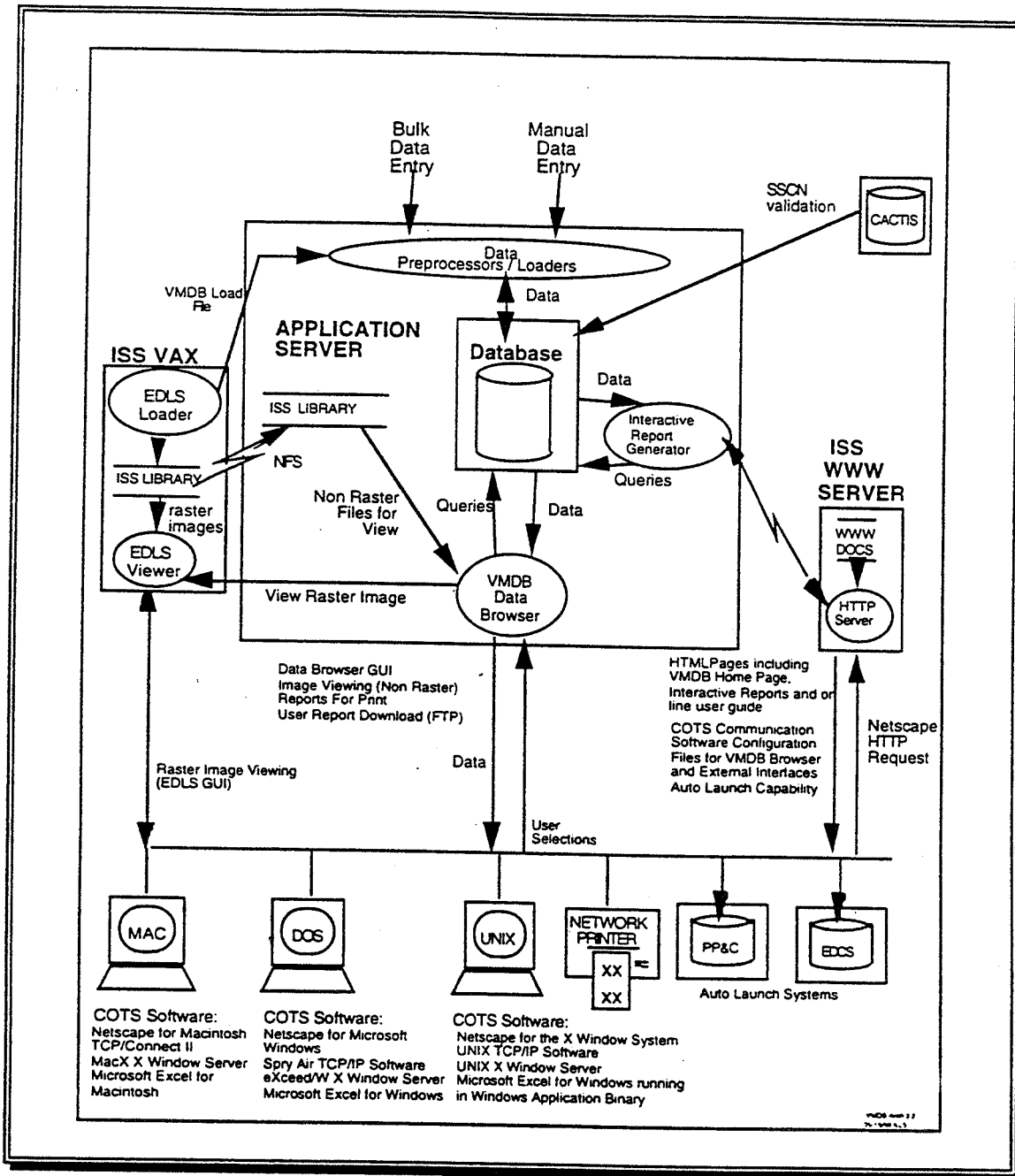


Figure 3.- VMDB Architecture

Not all ISSA technical data is contained in the VMDB. In the case of EEE parts data, VMDB contains only a small subset of the data needed to design, test, build, and certify space station parts. The VMDB data table for EEE parts is shown at Figure 4.

Input Col. #	Input Column Name	TT Col. #
1	Sub Element Number	9
2	Part Number	2
3	Part Name	7
4	Part Instance Number	3
5	Mfg. Cage Code	1
6	NHA Part Number	5
7	NHA Part Inst. Num.	6
8	NHA Mfg. Cage Code	4
9	Part Instance Quant.	8
10	Flight	10
11	System Number (Abbrev.)	11
12	Subsystem	12
13	IPL Level	13
14	GFE Designator	14
15	Part Instance Name	15
16	Reference Designator	16
17	Logistics Control Number	17
18	PI Comment	18
19	DIL Designator	19
20	FLT GSE Designator	20
21	Item Function Desc.	21
22	Change Type	22
23	SSCN	23
24	Change Justification	24
25	Prime Designator	25
26	PUI	26
27	DFMD Designator	27
DYN	Table Designed Part	1,2,7
DYN	Table Hardware Part	1,2
DYN	Table Part Instance	1,2,3,8,13-21, 25-27
DYN	Table PI NHA	1,2,3,4,5,6
DYN	Table System Part	1,2,3,11,12
DYN	Table Subelement	9,1,2,3
	Table Change Logs	22, 24
	Table Change Log Auths	23

Figure 4.- Vehicle Master Data Base Data Table Field Names

The Access database this project developed needed to contain all data relevant to EEE parts as shown above in Figure 1.

Populating the Access database with contractor, subcontractor, and supplier EEE parts data required that data loaders be built to accept electronic data from these sources, check the data for correctness, and reformat it for input into the Access database. Prototype loaders were developed for data from the three Product Groups supplying data to the prime contractor, Boeing, and the database populated with enough data to test the Access database system. Data from other sources such as Government Furnished Equipment (GFE) or the Government Industry Data Exchange Program (GIDEP) were identified for development of data loaders as well.

In order to meet the EEE parts data needs of the ISSA Program, several tables were created to facilitate data presentations and to conduct verifications and certifications. These tables are those shown in Figure 1. To facilitate data organization and access, the inherent relational structure of the Access database system was utilized. Also, a normalization process was implemented to ensure there were no duplications of data and that the relationships among the various database tables were identified.

The remaining portion of the project that was completed involved creating Access macros that served as data field comparitors between database tables. The first was a comparitor that identified any records that contained fields in which the field contents were changed in a data resubmittal or update. This enabled database managers to expediently make changes to the data base using electronic data processing and still maintain control over each change in the database. The second comparitor checked specified field values for approved status for EEE parts. One of the key EEE parts data management tasks was to verify that all of the parts, and only the correct and approved parts, were actually in the database. Using a computer-based review of engineering drawing parts lists, next higher assembly data from indentured parts lists, and checking the reasonableness of subtier data on parts were decided to be appropriate ways to validate the EEE parts data. These comparitors were tested with a sample of the EEE parts data to verify their correct operation.

Additional tasks were identified to complete the development of an Access database for EEE parts for the ISSA. These additional tasks were proposed for a follow-on grant which was submitted to the JSC Director for consideration. These additional tasks were:

- a. Create the as designed to the as built parts list comparitor.
- b. Test the process of verifying that all parts are in the database.
- c. Write a users' manual.
- d. Update the Access software with Microsoft's latest version.
- e. Verify The EEE parts database accuracy and efficiency.
- f. Create a loader to input data from the VMDB.
- g. Complete data base populating process.

CONCLUSIONS

The structure and initial testing of the EEE parts database for the ISSA was completed. After a lengthy familiarization process of the existing NASA information system capabilities and the data management requirements of the ISSA program, it was decided to use Microsoft's Access database software to host the EEE parts information needed in the design, testing, and fabrication phases. The database was organized into tables for use in reports and certifications utilizing relational structures and normalization techniques. Several prototype data loaders were developed to facilitate the transfer of data from contractor sources into the Access database. Also, several prototype queries were developed and exercised to compare new data with existing and to check status of parts in order to verify their acceptability for design or readiness for flight. Much more work needs to be done; several of those tasks were identified in the report.

Dynamics Questions Associated with the AERCam Sprint Free-Flyer

Trevor Williams
University of Cincinnati
ER6
August 25, 1996

Jon Erickson
Chief Scientist
Automation, Robotics, & Simulation Division
Engineering Directorate


Trevor Williams


Jon Erickson

**DYNAMICS QUESTIONS ASSOCIATED WITH THE
AERCAM SPRINT FREE-FLYER**

Final Report

NASA/ASEE Summer Faculty Fellowship Program - 1996

Johnson Space Center

Prepared By: Trevor Williams, Ph.D.
Academic Rank: Associate Professor
University & Department: University of Cincinnati
Department of Aerospace Engineering
Cincinnati, Ohio 45221-0070

NASA/JSC

Directorate: Engineering
Division: Automation, Robotics and Simulation
Branch: Special Projects Office
JSC Colleague: Jon Erickson, Ph.D.
Date Submitted: August 25, 1996
Contract Number: NAG9-867

ABSTRACT

The International Space Station will require the development of small robotic vehicles for such tasks as external inspection, monitoring of extravehicular activities (EVAs) and station build-up, and providing additional lighting at EVA worksites. The Autonomous EVA Robotic Camera (AERCam) family of free-flyers is currently being developed at NASA Johnson Space Center to perform these functions; the first member of the family is the AERCam Sprint vehicle [1].

Many interesting dynamical questions are associated with the Sprint free-flyer. For instance, the reaction of a vehicle which is nearly spherically symmetric (such as Sprint) to a stuck-on thruster is significantly more complicated than that obtained for an idealized, perfectly spherical, spacecraft model. In particular, the real spacecraft will experience a form of forced nutation, with convergence towards either its major or minor principal axis, depending on both the applied torque and the mass properties of the vehicle. Furthermore, the body-fixed jet force vector may have a significant component along this principal axis, so giving rise to a considerable net linear acceleration of the spacecraft. The large velocity that can result is very important, as it may lead to collision with the nearby Orbiter, and is completely overlooked in the idealized analysis. This report will firstly briefly describe the stuck-on thruster dynamics of the real vehicle, and outline how the small products of inertia of the spacecraft determine the time constants of the motion. Secondly, the dynamical effects of a failed-off jet on the Sprint free-flyer will be described in more detail, and compared with the stuck-on thruster case. This will help to show whether the two malfunctions should be dealt with differently in flight.

Finally, the stuck-on thruster detection software (known as the *uncommanded motion* algorithm) that is proposed to be flown on the Sprint vehicle will be analyzed, and all possible perturbation sources that may tend to give rise to false stuck-on thruster alarms quantified. It will be shown that false alarms can be triggered by discrete events such as a failed-off thruster, a glancing collision with Orbiter structure, or thruster saturation. They can also be triggered by a combination of errors introduced by constantly present sources such as thrust level errors, thruster misalignment, inertial cross-coupling, angular rate sensor noise, and structural vibrations induced by thruster firings. Based on this fact, the original plan to have the spacecraft enter safe mode whenever the uncommanded motion algorithm is triggered does not appear to be advisable. A better approach seems to be to provide the Sprint pilot with a warning whenever uncommanded motion is detected, and then allow the crew to determine whether safing the vehicle is appropriate.

INTRODUCTION

The Sprint uncommanded motion algorithm compares the actual angular acceleration experienced by the vehicle, as measured by differencing filtered data from rotation rate sensors on-board, with the accelerations that would be obtained if the current command inputs were applied to an idealized, perfectly spherically symmetric, vehicle. If one of the Sprint thrusters were to stick on, a significant difference (approximately 16.3 deg/s^2) would exist between these two accelerations. The intent of the uncommanded motion algorithm is to detect this potentially hazardous condition [2] and automatically place the vehicle into safe mode by closing its isolation valve, so deactivating the propulsion system.

However, several discrete events other than a stuck-on thruster can also trigger the uncommanded motion algorithm. For instance, a jet which has failed off will generate the same type of acceleration error as will a stuck-on one. However, a failed-off jet is actually, as will be shown, a fairly benign event, leaving the vehicle fully controllable in 2.5 translational and 2.5 rotational degrees-of-freedom. Causing Sprint to enter safe mode, and consequently possibly be lost, as a result of a failed-off jet is not advisable. In the case of two other events which can also give rise to uncommanded motion, safing the vehicle appears to be essentially the worst possible action to take. The first of these is a glancing blow with Orbiter structure, which can lead to significant uncommanded Sprint angular rates. (According to analysis by D. Wells, these rates may be increased by the shear properties of the Sprint free-flyer protective covering.) The second is inadvertent rotation of the vehicle at rates (above about 30 deg/s) which are high enough to saturate the Sprint rate sensors; saturation causes the measured rates to "freeze", and hence gives rise to a measured angular acceleration of zero. In both these cases, it seems likely that immediate maneuvering by the crew is desirable in order to prevent loss of Sprint; this is not possible if the vehicle is in safe mode.

There also include various effects which are essentially constantly present that can similarly give rise to some amount of difference between measured and predicted angular accelerations. These sources include errors in the level of thrust produced by the Sprint jets, thruster misalignment, cross-coupling due to imperfect mass properties (CG offsets and non-spherically symmetric inertias), rate sensor noise, and Sprint structural vibrations excited by thruster firings. In order to determine whether these effects can give rise to false alarms which are not associated with a discrete event, it is necessary to quantify each of them in turn. This is the subject of the present report. In this analysis, the nominal parameters for the Sprint free-flyer given in Table 1 will be assumed. Worst-case values for the perturbation quantities considered, for example CG offset or thruster misalignment angle, will be given as required in the appropriate sections.

TABLE 1.- SPRINT NOMINAL PARAMETERS

Quantity	Value
Jet thrust, f	0.085 lbf
Jet moment arm, l	4 in
Axial moment of inertia, I_o	464 lbmin^2
Two-jet angular acceleration, α_o	32.5 deg/s^2

STUCK-ON THRUSTER DYNAMICS

The Sprint free-flyer is nominally a spherically symmetric vehicle, with center of mass (or center of gravity: CG) located at the geometric center of the spacecraft, and with principal axes aligned with the thruster axes. However, Sprint is actually made up of many individual discrete components, and so is by no means uniform. Consequently, it will inevitably have mass properties that are slightly perturbed from those of a perfect sphere. This small difference in mass properties can be shown [2] to have very significant implications in the event that Sprint develops a stuck-on thruster.

If a thruster mounted on an ideal sphere sticks on, the resulting axis of rotation of the body is fixed, and aligned with the applied torque. As a result, the applied force cancels as the vehicle rotates; the only net linear acceleration occurs during the very first phase of the motion, before a significant rotation rate has been set up. In the near-symmetric case, on the other hand, the motion can be broken into several distinct phases: an initial phase, where the motion is much as in the ideal case; a transition phase, with quite complicated body rates; and an asymptotic phase, where the motion approaches a spin about either the major or minor principal axis of the spacecraft. The linear acceleration experienced in the asymptotic phase can, for the worst possible combination of thrust direction and vehicle mass properties, approach the one jet thrust/mass ratio of the spacecraft. Furthermore, it can act for an extended period of time, unlike the short initial period that produces a Δv in the ideal case. Consequently, the Δv resulting from a stuck-on thruster on a realistic vehicle may be considerably greater than that obtained for an ideal symmetric one. This is illustrated in Figure 1, where the solid curve is the linear speed that would be obtained for a stuck-on thruster using the current best estimate of Sprint mass properties; the dotted curve, by comparison, is the much smaller velocity obtained in the ideal case. It can be seen that a period of about 25 s (this time constant depends [2] on the mass properties of the spacecraft, increasing as these become more nearly spherical) exists before the near-symmetric vehicle enters into the asymptotic phase, with its undesirably high linear acceleration. The importance of timely detection and deactivation of a stuck-on thruster on a real vehicle is therefore clear.

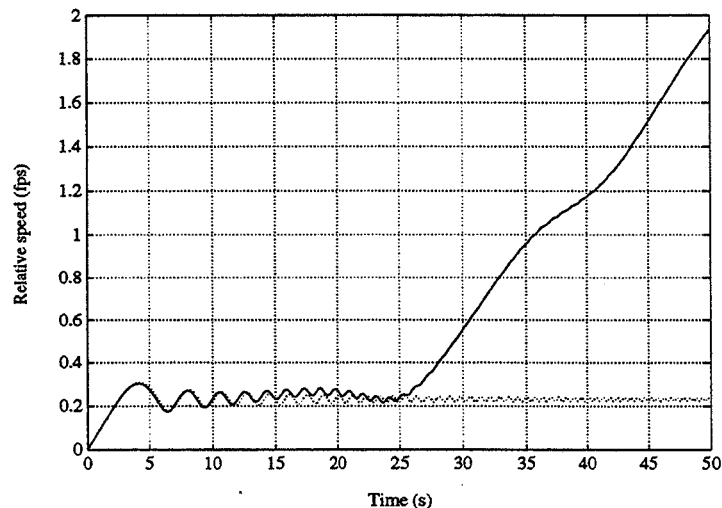


Figure 1.- Linear speed resulting from Sprint stuck-on thruster.

FAILED-OFF THRUSTER DYNAMICS

A single failed-off thruster on the Sprint free-flyer will be shown in this section to produce the following effects, whether or not Automatic Attitude Hold (AAH) is operating:

- (1) The vehicle will be rendered effectively uncontrollable in one translational direction.
- (2) Rotational control authority in one direction will be approximately halved. Rotations in this direction will also induce a small amount of uncommanded translational motion.

These effects can be seen to be quite benign when compared to those that were described above for a stuck-on thruster.

Translation Maneuvers, AAH On

Suppose, for example, that thruster 1 fails closed. If a positive x command is input with AAH on, the Sprint jet select logic will command the two $+x$ jets, numbers 1 and 2, to fire. Only jet 2 will actually open though, leading to a significant positive pitching acceleration of about 16.3 deg/s^2 . The AAH rate limit of 0.3 deg/s will consequently be reached after less than 20 ms . At this point, AAH will attempt to select jets in order to impart both a positive x and a negative pitch acceleration, i.e. (again from the Sprint jet select logic) only the non-operational thruster 1 will be commanded on. Consequently, no further changes will occur to either the linear or angular rates of the vehicle, regardless of how long the $+x$ command remains on; the resulting total Δv is a negligible 0.0017 fps (0.021 in/s). A $+x$ translation command thus cannot be executed under AAH if jet 1 (or jet 2) fails off; however, y , z and $-x$ translations are unaffected. Similar results apply for inoperability of any other single thruster.

Translation Maneuvers, AAH Off

If the same $+x$ command is input with jet 1 again failed closed but AAH now off, Sprint will initially accelerate at a rate of 0.094 ft/s^2 in the desired direction. However, it will again experience a positive pitch acceleration of about 16.3 deg/s^2 , leading to a non-zero pitch rate as the maneuver proceeds. For instance, a command input of 0.5 s duration will give rise to a Δv of 0.047 fps , a pitch rate of 8.3 deg/s and a pitch angle of 2.1 deg at the end of firing. If this rotation rate is to be nulled after the Δv is established, this requires (from the jet select table) firing jets 1 and 4. The effect of firing the single operational negative pitch jet, 4, will be not only to null the pitch rate, but also essentially to null the linear Δv (apart from a small effect due to the rotation of the vehicle between the two burns). It is therefore not possible to translate Sprint in the $+x$ direction while manually keeping its attitude rates low if jet 1 (or jet 2) fails off.

Rotation Maneuvers

The effect of a failed-off jet on rotation commands is independent of whether AAH is activated. In either case, the control authority in the affected rotational direction (e.g. negative pitch for thruster 1; roll, yaw and positive pitch are unaffected) is reduced to

about half of its nominal value. In addition, an uncommanded Δv is induced by rotational inputs in this direction. For firing durations of less than about 3 s, the resulting linear distance covered is roughly proportional to the total angle of rotation: for example, for a pitch through 90 *deg* with a failed-off thruster, the associated distance is about 0.5 *ft*. The small magnitude of this distance is a reflection of the fact that Sprint is much more responsive in rotation than in translation.

Finally, other rotational inputs may give rise to a positive pitch rate as a result of cross-coupling through non-zero products of inertia. Translational inputs may similarly produce pitch as a result of non-zero CG offsets. If jet 1 has failed and this induced pitch rate is nulled, either manually or by means of AAH, a net linear Δv will again result. However, this effect will be minor, and almost certainly not noticeable, for the mass properties expected of the Sprint free-flyer.

It is therefore clear that a failed-off jet produces a much more benign dynamics problem than does a stuck-on thruster. The operational actions that should be taken in response to these two types of malfunction are consequently likely to be very different. However, both failures will trip the Sprint uncommanded motion alarm in precisely the same way. This suggests that it is not advisable to have the vehicle automatically enter safe mode, by shutting its propulsion system isolation valve, whenever the uncommanded motion alarm trips. The following sections will emphasize this conclusion by examining several other ways in which the uncommanded motion alarm can potentially be triggered by causes other than a stuck-on thruster.

JET THRUST LEVEL ERRORS

The specified tolerance on the thrust produced by each Sprint jet is $\pm 10\%$. Indeed, the thrust of the SAFER jets on-orbit during STS-64, as determined from post-flight data analysis [3], was approximately 10% below the nominal value of 0.80 *lbf*. Since the Sprint thrusters are simply SAFER ones operated at lower inlet pressure, their thrust level will presumably be similarly affected by such factors as ambient temperature. Consequently, it seems highly plausible that a Sprint thrust error of up to 10% may be observed on-orbit. However, there should not be significant differences between the thrust produced by each jet, since the lengths of the propellant lines in the Sprint free-flyer are all very similar. (On the other hand, analysis by D. Wells suggests that the openings for each thruster in the Sprint protective covering will inevitably differ slightly; this can then give rise to differential forces and moments, as a result of plume impingement. This mechanism is quite difficult to characterize fully and is not addressed here, but should be considered for further analysis.)

The result of this type of thrust error is essentially no angular acceleration in reaction to a translation command, but up to a 10% error in response to a rotation input. For the nominal Sprint parameters, this corresponds to an uncommanded angular acceleration of about 3.25 *deg/s*² for a two-jet command.

THRUSTER MISALIGNMENT

This section quantifies the largest unmodeled angular accelerations that can be caused as a result of credible errors in alignment and positioning of the Sprint thrusters. The bulk of this effect will be shown to be due to misalignment, rather than position, errors.

Analysis

Consider, for example, Sprint jet 1 (similar results will apply for all other jets). This has nominal thrust vector $\mathbf{f}_o = f(1 \ 0 \ 0)^T$ and position $\mathbf{r}_o = (-x \ 0 \ -l)^T$, where the distance $x = 5$ in, being along the direction of nominal thrust, has no effect on the nominal torque. In fact, this torque is a pure negative pitching moment,

$$\mathbf{t}_o = \mathbf{r}_o \times \mathbf{f}_o = fl \begin{pmatrix} 0 \\ -1 \\ 0 \end{pmatrix}. \quad (5.1)$$

Suppose now that the alignment of this jet is slightly in error, making a (small) cone angle γ to the nominal thrust axis. If the clock angle, φ , of the thrust direction in the yz-plane is measured from the positive y axis towards the positive z axis, then the new thrust vector can be written as

$$\mathbf{f} = f \begin{pmatrix} \cos \gamma \\ \sin \gamma \cos \varphi \\ \sin \gamma \sin \varphi \end{pmatrix}. \quad (5.2)$$

Suppose that the thruster is in addition slightly displaced from its nominal position, to the new location

$$\mathbf{r} = \begin{pmatrix} -x + \delta x \\ \delta y \\ -l + \delta z \end{pmatrix}. \quad (5.3)$$

The resulting actual torque produced by the jet can then be shown to be, for small cone angle γ ,

$$\mathbf{t} = \mathbf{r} \times \mathbf{f} \approx \mathbf{t}_o + \gamma \cdot f \begin{pmatrix} \delta y \sin \varphi + l \cos \varphi \\ x \sin \varphi \\ -x \cos \varphi \end{pmatrix} + f \begin{pmatrix} 0 \\ \delta z \\ -\delta y \end{pmatrix}. \quad (5.4)$$

Approximating Sprint as a spherically symmetric vehicle, the error between the actual angular acceleration produced by firing this jet and the pure negative pitch that is expected in the nominal case is given by

$$\delta \boldsymbol{\alpha} = (\mathbf{t} - \mathbf{t}_o) / I_o, \quad (5.5)$$

where I_o is the moment of inertia of the idealized spherical vehicle about any axis, as given in Table 1.

Results

Based on discussions with designers W. Templeman and T. Garnett, a conservative choice of worst case values for misalignment and positioning error are $\pm 5 \text{ deg}$ and $\pm 0.020 \text{ in}$, respectively. Substituting these values into Eqs. (2.4) and (2.5), and choosing the value for the clock angle ϕ which produces the largest error for each axis in turn ($\phi = 0$ for x and z; $\phi = 90 \text{ deg}$ for y), gives the following maximum errors:

Roll: 1.42 deg/s^2 ;

Pitch: 1.77 deg/s^2 ;

Yaw: 1.77 deg/s^2 .

These correspond to 9%, 11% and 11%, respectively, of the nominal one-jet angular acceleration of 16.25 deg/s^2 . The worst-case unmodeled angular accelerations that can be caused by thruster misalignment during a two-jet translation or rotation command are clearly double the values listed above. However, it should be remembered that Sprint is actually capable of firing up to six thrusters at any one time. Although it is likely that the crew will be trained to input only single-axis commands, two clear mechanisms exist whereby more than two thrusters can be fired simultaneously in practice. The first mechanism is AAH, which will fire multiple thrusters to null out rates due to cross-coupling during a single-axis command input by the crew; the second is the inadvertent input of simultaneous commands by the Sprint pilot. During the on-orbit flight test of SAFER on STS-64, there were a total of 43 such occurrences [4]. As the Sprint pilot will operate the SAFER handcontroller without the encumbrance of a pressurized suit glove, it is likely that there will be fewer such inadvertent commands when flying Sprint. However, their occasional appearance certainly cannot be ruled out.

From the point of view of triggering a stuck-on thruster false alarm, the worst misalignment case appears to be two simultaneous two-jet inputs, both of which produce the worst possible angular acceleration about the third, uncommanded, axis. The resulting acceleration discrepancy can be seen from the above to be 7.08 deg/s^2 .

INERTIAL CROSS-COUPLING

The small differences in mass properties between the Sprint free-flyer and an ideal spherically symmetric vehicle lead to three distinct types of unmodeled angular accelerations. These cross-coupling effects are as follows:

- (1) Angular accelerations in response to a translation input, as a result of CG offsets.
- (2) First-order (or direct) modification to the angular acceleration produced by an applied torque, as a result of both non-zero products of inertia and small variations between the moments.
- (3) Second-order (or high-rate) angular acceleration, even in the torque-free case, again due to small inertia variations.

All three sources are quantified in this section.

Sprint Equations of Attitude Motion

The equation of rotational motion for any rigid body is

$$\mathbf{t} = I\dot{\boldsymbol{\omega}} + \boldsymbol{\omega} \times I\boldsymbol{\omega}, \quad (6.1)$$

where \mathbf{t} is the applied torque about the CG of the vehicle, $\boldsymbol{\omega}$ the angular velocity vector in body-fixed coordinates, and I the inertia matrix about the CG in this same coordinate system.

For a near-spherically symmetric vehicle such as Sprint, we have

$$I = I_o I_3 + \Delta I, \quad (6.2)$$

where I_o is the nominal (i.e. mean) moment of inertia of the ideal sphere about any axis, I_3 the 3x3 identity matrix, and ΔI a matrix made up not only of the small products of inertia of the real spacecraft, but also of the variations of its true moments of inertia from the nominal value. In practice, we will have $\|\Delta I\| \ll I_o$; however, we are unlikely to know for certain how small ΔI actually is. We are even less likely to know the perturbation in any particular moment or product of inertia. Consequently, in what follows, one question that will be studied is how the size of $\|\Delta I\|$ affects the worst case cross-coupling that can be encountered.

Substituting Eq. (6.2) into Eq. (6.1) yields

$$\begin{aligned} \mathbf{t} &= (I_o I_3 + \Delta I)\dot{\boldsymbol{\omega}} + \boldsymbol{\omega} \times (I_o I_3 + \Delta I)\boldsymbol{\omega} \\ &= (I_o I_3 + \Delta I)\dot{\boldsymbol{\omega}} + \boldsymbol{\omega} \times \Delta I\boldsymbol{\omega}, \end{aligned} \quad (6.3)$$

since $\boldsymbol{\omega} \times I_o \boldsymbol{\omega} = \mathbf{0}$. Consequently, the angular acceleration is given as

$$\dot{\boldsymbol{\omega}} = (I_o I_3 + \Delta I)^{-1} [\mathbf{t} - \boldsymbol{\omega} \times \Delta I\boldsymbol{\omega}]. \quad (6.4)$$

From the well known matrix inverse perturbation result

$$(I_o I_3 + \Delta I)^{-1} \approx [I_3 - (\Delta I/I_o)]/I_o \quad (6.5)$$

for small ΔI , we therefore have that

$$\begin{aligned} \dot{\boldsymbol{\omega}} &\approx [I_3 - (\Delta I/I_o)] [\mathbf{t} - \boldsymbol{\omega} \times \Delta I\boldsymbol{\omega}] / I_o \\ &\approx [I_3 - (\Delta I/I_o)] \mathbf{t} / I_o - \boldsymbol{\omega} \times \Delta I\boldsymbol{\omega} / I_o, \end{aligned} \quad (6.6)$$

where second-order terms in ΔI have been neglected. To simplify the notation, define the normalized inertia matrix perturbation $\tilde{\Delta I} = \Delta I/I_o$. Eq. (6.6) then becomes

$$\dot{\boldsymbol{\omega}} \approx [I_3 - \tilde{\Delta I}] \mathbf{t} / I_o - \boldsymbol{\omega} \times \tilde{\Delta I} \boldsymbol{\omega}. \quad (6.7)$$

This expression will now be used to study the three possible types of cross-coupling.

Translation to Rotation Cross-Coupling

Suppose the CG is offset to a position $\delta \bar{\mathbf{r}}$ relative to the geometric center of the vehicle. The resulting torque if two translation jets with thrust directions \mathbf{f} fire is then

$$\mathbf{t} = -2\delta \bar{\mathbf{r}} \times \mathbf{f}. \quad (6.8)$$

Substituting this expression into Eq. (6.7) and neglecting higher-order terms, i.e. the one involving the product of the perturbation quantities $\delta\bar{\mathbf{r}}$ and $\Delta\tilde{\mathbf{I}}$ and the one involving both $\Delta\tilde{\mathbf{I}}$ and the squared rotation rate (which will be low for translation maneuvers), yields

$$\dot{\boldsymbol{\omega}} \approx -2\delta\bar{\mathbf{r}} \times \mathbf{f}/I_o. \quad (6.9)$$

This has norm satisfying the inequality

$$\|\dot{\boldsymbol{\omega}}\| \leq 2f\delta\bar{r}, \quad (6.10)$$

with the worst-case angular acceleration achieved if $\delta\bar{\mathbf{r}}$ is perpendicular to \mathbf{f} .

Direct Rotation to Rotation Cross-Coupling

In this case, the applied torque is unchanged from the nominal, $\mathbf{t} = \mathbf{t}_o$. However, the inertia perturbations lead to changes in the resulting angular accelerations. For relatively low angular rates, e.g. during the initial phase of a maneuver, the last term on the right-hand side of Eq. (6.7) can be omitted, giving

$$\dot{\boldsymbol{\omega}} \approx [I_3 - \Delta\tilde{\mathbf{I}}]\dot{\boldsymbol{\omega}}_o, \quad (6.11)$$

where $\dot{\boldsymbol{\omega}}_o = \mathbf{t}_o/I_o$ is the angular acceleration expected in the ideal, spherically symmetric case. The norm of the difference between the actual and ideal angular accelerations therefore satisfies

$$\|\dot{\boldsymbol{\omega}} - \dot{\boldsymbol{\omega}}_o\| \leq \|\Delta\tilde{\mathbf{I}}\| \cdot \|\dot{\boldsymbol{\omega}}_o\|, \quad (6.12)$$

with equality being achieved when $\dot{\boldsymbol{\omega}}_o$ is parallel to the eigenvector of $\Delta\tilde{\mathbf{I}}$ that corresponds to its greatest eigenvalue.

High-Rate Rotation to Rotation Cross-Coupling

At high angular rates, the fact that the last term on the right-hand side of Eq. (6.7) depends on ω^2 makes this quantity potentially significant. This is particularly so when no external torques are applied to the vehicle, as the other forcing terms are then zero. But

$$\|\boldsymbol{\omega} \times \Delta\tilde{\mathbf{I}}\boldsymbol{\omega}\| \leq \|\Delta\tilde{\mathbf{I}}\| \cdot \|\boldsymbol{\omega}\|^2 = \omega^2 \|\Delta\tilde{\mathbf{I}}\|, \quad (6.13)$$

with equality holding if the vector $\Delta\tilde{\mathbf{I}}\boldsymbol{\omega}$ is orthogonal to $\boldsymbol{\omega}$.

Results

The current best estimates for the actual, non-spherically symmetric, mass properties of the Sprint free-flyer correspond to $\|\Delta\tilde{\mathbf{I}}\| = 8\%$ and a CG offset of magnitude 0.43 in. A reasonably conservative choice of upper limits for these values therefore appears to be 10% and 0.5 in, respectively. Also, the Sprint rate sensors saturate at around 30 deg/s, so this is the highest rate that should ever be encountered in (intentional) on-orbit maneuvering. In what follows, this limit will be assumed to be reached about only one axis at any given time, the other two having zero rates. Using these values, it can be shown that the maximum angular accelerations that can be produced by the three cross-coupling mechanisms are as follows:

- (1) CG offset (translation command): 4.06 deg/s^2 .
- (2) Direct inertia variation effects (early stage of a rotation command): 3.25 deg/s^2 .
- (3) High-rate inertia variation effects (later stage of a rotation command): 1.57 deg/s^2 .

These effects will typically not all occur simultaneously. However, as noted previously, simultaneous maneuvering about more than one axis cannot be ruled out with Sprint. For example, consider applying simultaneous x and roll commands to the vehicle. For the worst-case combination of CG and inertia perturbations, the translation input can produce an acceleration about, for instance, yaw of 4.06 deg/s^2 , while the roll can contribute another 3.25 deg/s^2 , in its early stages, about this same axis. Thus, the worst-case aggregate cross-coupling acceleration is approximately 7.31 deg/s^2 .

RATE SENSOR NOISE

The angular rates output by the Sprint quartz rate sensors (termed the SE rates) are quite noisy, as was seen from the results produced by this same type of sensor during the STS-64 SAFER orbital test flight (see, for instance, [3]). Consequently, if these measured rates were differenced in order to generate approximate vehicle angular accelerations, the results that would be obtained would be extremely poor. Instead, the SE rates are first passed through a vibration filter (described in detail in [5]), producing the vibration filtered (VF) rates. These filtered rates are then differenced to obtain approximate vehicle angular accelerations. The question addressed in this section is that of quantifying the extent to which the noise present in the SE rates can lead to errors in these estimated accelerations.

Analysis

Suppose each SE rate output is corrupted by additive white noise $v(t)$, band-limited to the frequency range $|\omega| \leq \omega_c$ and with standard deviation σ_v . From the upper loop in the vibration filter [5], the transfer function from this noise to the estimated angular acceleration of the vehicle $a(t)$, i.e. the derivative of the VF rate, is

$$G(s) = \frac{s}{1 + sT}, \quad (7.1)$$

where $T = K_1^{-1} = 0.125 \text{ s}$ for Sprint.

Now, the spectral function of the white noise $v(t)$ is [6]

$$S_v(j\omega) = \begin{cases} A, & |\omega| \leq \omega_c, \\ 0, & |\omega| > \omega_c, \end{cases} \quad (7.2)$$

where the constant $A = \pi\sigma_v^2/\omega_c$. The spectral function of the output $a(t)$ is therefore

$$S_a(j\omega) = G(j\omega)G(-j\omega)S_v(j\omega). \quad (7.3)$$

But, from Eq. (7.1),

$$G(j\omega)G(-j\omega) = \frac{j\omega}{1 + j\omega T} \cdot \frac{-j\omega}{1 - j\omega T}$$

$$\begin{aligned}
&= \frac{\omega^2}{1 + \omega^2 T} \\
&= \frac{1}{T^2} \cdot \left\{ 1 - \frac{1}{1 + \omega^2 T} \right\}.
\end{aligned} \tag{7.4}$$

The spectral function of $a(t)$ is thus given as

$$S_a(j\omega) = \frac{A}{T^2} \cdot \left\{ 1 - \frac{1}{1 + \omega^2 T} \right\}, |\omega| \leq \omega_c; 0 \text{ otherwise.} \tag{7.5}$$

Consequently, the variance of the output can be computed as

$$\begin{aligned}
\sigma_a^2 &= \frac{1}{2\pi} \cdot \int_{-\infty}^{\infty} S_a(j\omega) d\omega \\
&= \frac{1}{2\pi} \cdot \int_{-\omega_c}^{\omega_c} \frac{A}{T^2} \cdot \left\{ 1 - \frac{1}{1 + \omega^2 T} \right\} d\omega \\
&= \frac{A\omega_c}{\pi T^2} - \frac{A}{\pi T^3} \arctan \omega_c T,
\end{aligned} \tag{7.6}$$

from [6], Eq. (3.4.6), p. 128. Using the expression for A that followed Eq. (7.2), this can be simplified to yield

$$\begin{aligned}
\sigma_a^2 &= \frac{\sigma_v^2}{T^2} - \frac{\sigma_v^2}{T^3 \omega_c} \arctan \omega_c T \\
&= \frac{\sigma_v^2}{T^2} \cdot \left\{ 1 - \frac{\arctan \beta}{\beta} \right\},
\end{aligned} \tag{7.7}$$

where $\beta = \omega_c T$ is dimensionless.

Results

The raw Sprint rate sensor noise is white, band-limited at 100 Hz and with standard deviation 0.1 deg/s. However, the sensor outputs are initially passed through an analog pre-filter which produces the SE rates that actually enter the vibration filter. This analog filter has bandwidth 50 Hz, with 40 dB/decade decay above this frequency. The result of this is that the sensor noise entering the vibration filter has parameters $\omega_c \approx 100\pi$ rad/s and $\sigma_v \approx 0.08$ deg/s. Consequently, from Eq. (7.7), the estimated angular acceleration has standard deviation $\sigma_a \approx 0.63$ deg/s. It should be noted that this is approximately 8 times as large as the standard deviation of the noise in the SE rates. This follows from that fact that ω_c is comparatively large, so β is also. Hence, $(\arctan \beta)/\beta \approx \pi/2\beta$ is small, so (from Eq. (7.7)) $\sigma_a \approx \sigma_v/T = K_1 \sigma_v = 8\sigma_v$ for Sprint.

Consequently, the largest apparent uncommanded acceleration that may reasonably be generated as a result of sensor noise, after passing through the Sprint vibration filter, is $3\sigma_a \approx 1.89$ deg/s.

STRUCTURAL VIBRATIONS

Firing the Sprint thrusters will, to some extent, excite vibration modes of the free-flyer, which can then lead to oscillations in the structure that supports the rate sensors. An apparent vehicle oscillatory rotation may therefore be observed that is actually the result of structural vibration. This section gives a simplified analysis of this problem, and provides an approximate quantification of the apparent uncommanded acceleration that can be caused in this way.

Analysis

Consider a single degree-of-freedom model for the first vibration mode of the Sprint free-flyer. If the sinusoidal linear displacement resulting from this mode when excited by two thrusters of thrust f is denoted by x , then the equation of motion for this mode is

$$\hat{m}\ddot{x} + \hat{k}x = 2f, \quad (8.1)$$

where \hat{m} is the effective modal mass (the portion of the mass of the vehicle that contributes to the motion of this mode) and $\hat{k} = \omega^2 \hat{m}$, where ω is the modal natural frequency. Assuming the initial conditions $x(0) = 0$ and $\dot{x}(0) = 0$, Eq. (8.1) can be shown to have solution

$$x(t) = X_{\max} [1 - \cos \omega t], \quad (8.2)$$

oscillatory at the natural frequency, where the amplitude $X_{\max} = 2f/\hat{m}\omega^2$. The resulting linear rate is thus

$$\dot{x}(t) = \omega X_{\max} \sin \omega t. \quad (8.3)$$

This deflection will, for the first vibration mode, occur approximately at the midpoint of the vehicle. If the effective radius of the vehicle for this vibration mode is \hat{R} , the approximate sensed angular rate caused by this oscillation will be

$$\dot{\theta}(t) = (\omega X_{\max} / \hat{R}) \sin \omega t, \quad (8.4)$$

which has amplitude

$$\dot{\theta}_{\max} = \frac{2f}{\hat{m}\hat{R}\omega}. \quad (8.5)$$

Results

Based on a structural analysis performed by S. Kienle, the fundamental frequency of the Sprint structure occurs at approximately 80 Hz, which corresponds to $\omega \approx 500 \text{ rad/s}$. Furthermore, values of 3 kg and 0.1 m appear to be reasonable for the effective mass and radius, respectively, for this mode. The amplitude of the resulting angular rate is thus, from Eq. (8.5), given as $\dot{\theta}_{\max} \approx 0.29 \text{ deg/s}$, which acts as a signal superimposed onto the raw rate sensor outputs. This then passes through the analog filter described in the last section, which attenuates it by a factor of approximately $50^2/80^2$, before entering with the SE rates into the network shown in the Figure. From Eq. (7.1), the transfer function between SE rates and estimated angular acceleration at these high frequencies is approximately $T^{-1} = K_1 = 8 \text{ s}^{-1}$. Consequently, the effect of structural vibrations on the

apparent uncommanded acceleration of the vehicle can be shown to be approximately 0.91 deg/s^2 .

SUMMARY OF OVERALL RESULTS

Table 2 summarizes the results obtained in the previous sections. The final angular acceleration value is the root-sum-square of the preceding ones. Thus, as each individual acceleration given is an estimate of the worst-case (or 3σ) contribution from each particular mechanism, this RSS total should likewise be an estimate of the worst-case (or 3σ) acceleration expected from all terms acting together.

TABLE 2.- CONTRIBUTORS TO APPARENT UNCOMMANDED ACCELERATION

Effect	Apparent acceleration (deg/s^2)
Thrust errors	3.25
Misalignment	7.08
Cross-coupling	7.30
Sensor noise	1.89
Vibrations	0.91
Total (RSS)	10.88

The angular acceleration that is expected to occur as a result of a single-thruster command about any particular axis is 16.25 deg/s^2 ; that for a two-jet command is 32.5 deg/s^2 . The method in which the uncommanded motion algorithm is implemented is that a tolerance band is set up around each of these nominal values, as well as around the null rate. Then, if the measured angular acceleration lies within the one-jet band, one thruster is deemed to be firing; if within the two-jet band, two are said to be operating; if within the null band, none are presumed to be firing about this axis.

In order for this approach to work, the bands must clearly be non-overlapping. They therefore can have half-widths of at most about 8 deg/s^2 . However, Table 2 shows that the worst-case uncommanded acceleration that may occur in practice as a result of the mechanisms studied, 10.88 deg/s^2 , exceeds this limit. The uncommanded motion algorithm therefore cannot be set up in this way and still avoid false alarms as a result of these sources. It therefore seems prudent to make this algorithm send a warning message to the Sprint pilot, rather than automatically put the free-flyer into safe mode.

Two final points should be noted. Firstly, the two major sources of uncommanded acceleration can be seen to be thruster misalignment and cross-coupling effects. Both of these would be considerably smaller if only one input at a time were possible. However, as previously mentioned, simultaneous multi-axis commands can arise either intentionally, via AAH, or by means of inadvertent handcontroller inputs. They therefore certainly should not be omitted from a worst case analysis of uncommanded motion. Secondly, considerable uncertainty exists in many of the parameters considered, notably thrust level, jet misalignment angle, CG offset, inertia variations, and structural vibrations

excited by thruster firings. Air bearing tests should be used before flight to quantify the CG offset and vibrations more accurately; most of the other parameters will be characterized from the on-orbit maneuvers that will be performed by Sprint. Future vehicles of the AERCam class should therefore possess considerably less uncertainty in these areas.

REFERENCES

- [1] 'Autonomous EVA Robotic Camera (AERCam) Sprint Critical Design Review', NASA Johnson presentation, June 1996.
- [2] T. Williams and S. Tanygin, 'Dynamics of a Near-Symmetrical Spacecraft Driven by a Constant Thrust', presented at AAS Spaceflight Mechanics Meeting, Austin, Texas, Feb. 1996.
- [3] T. Williams, S. Tanygin and L. Bolender, 'SAFER Mass Properties Determination: Results from On-Orbit Data', presented at AAS/AIAA Astrodynamics Conference, Halifax, Nova Scotia, Aug. 1995.
- [4] T.W. Williams and L. Bolender, 'SAFER Inadvertent Commands On-Orbit', report to Cliff Hess, January 26, 1995.
- [5] L. Merkel, 'Sprint DTO1 Avionics Software Design Document - Preliminary', Version 0.06, LMES, Feb. 20, 1996.
- [6] R.G. Brown, *Introduction to Random Signal Analysis and Kalman Filtering*, New York: John Wiley & Sons, 1983.

**ANALYSIS OF IMPACT INDUCED DAMAGE AND ITS EFFECT ON
STRUCTURAL INTEGRITY OF SPACE FLIGHT COMPOSITE
OVERWRAPPED PRESSURE VESSELS**

**Michael P. Wnuk
University of Wisconsin-Milwaukee
Johnson Space Center, NASA White Sands Test Facility**

**NASA Colleague:
Harold D. Beeson
Laboratories Office
White Sands Test Facility**



Dr. Michael P. Wnuk



Harold D. Beeson, Ph.D.

**ANALYSIS OF IMPACT INDUCED DAMAGE AND ITS EFFECT ON
STRUCTURAL INTEGRITY OF SPACE FLIGHT COMPOSITE
OVERWRAPPED PRESSURE VESSELS**

**Final Report
NASA/ASEE Summer Faculty Fellowship Program-1996
Johnson Space Center**

**Prepared by:
Academic Rank:**

**Michael P. Wnuk, Ph.D.
Professor**

University and Department:

**University of Wisconsin - Milwaukee
Dept. of Civil Engineering and
Mechanics
PO Box 784, Milwaukee, WI 53201**

NASA/JSC

**Laboratories Office
White Sands Test Facility**

JSC Colleague:

Harold D. Beeson, Ph.D.

Date Submitted:

August 9, 1996

Contract Number:

NAG 9-867

ABSTRACT

The objective of this research work has been to provide analytical background and support to the ongoing experimental program at NASA, White Sands Test Facility, involving testing composite overwrapped pressure vessels (COPV) for impact damage and cyclic pressurization.

Preliminary theoretical basis, including the governing equations for a shallow shell subjected to internal pressure, has been established. Effects of the Griffith type cracks on the structural integrity of the cylindrical vessel were evaluated by methods of Fracture Mechanics. The results indicate that the effective mass of the pressure vessel is an important factor influencing the response to impact events. We also have found that the material properties of the target, contained in the constitutive equations of the composite attached to the Aluminum liner, dominate the impact event in the low velocity range, the material properties become less important, while the target mass distribution and the impactor mass become more significant as the velocity of the impactor increases. Therefore, at high-velocity impact it is not only the kinetic energy of the impactor but also its mass which has a significant effect on the dynamics of the event, and consequently on the induced damage.

This work also suggests a methodology for an assessment of the rate of loading effects on the degradation of the material toughness associated with a high-velocity impact where the rate effects become significant. To model the rate dependence of the material response a viscoelastic-plastic constitutive equations were assumed, and on this basis predictions are made regarding the rate dependent material **resistance curve**.

Other dynamic phenomena associated with the impact event have been treated in the framework of the Computational Mechanics using the courtesy of Prof. P. Guebelle and his graduate student at University of Illinois at Urbana-Champaign who have an access to a super-fast computer located on their campus.

Finally, the guidelines for a follow-up research program are provided in the body of this report. They address three major areas:

- * theoretical research,
- * numerical studies, and
- * further experimental work.

1. Introduction

Experience has shown us that when a pressure vessel is damaged by an impacting hard object, two events may take place: (1) if the induced damage is small, the vessel will leak, (2) if the vessel is penetrated within a critical flaw size range, fracture will propagate catastrophically and a pneumatically pressurized vessel will explode.

Thin-walled pressure vessels resemble balloons and therefore are subject to puncture and sudden loss of structural integrity. For a given material, under a specified stress field due to internal pressure, there exists a characteristic crack length at which the structure becomes unstable and succumbs to a catastrophic failure. Inversely, one may conjecture that the burst pressure in a damaged vessel is a function of the material properties, geometry of the structure and the flaw size and shape.

Cracks of length less than critical threshold will cause leakage but not destruction. However, if the critical length is eventually reached, either by penetration or by growth of a small fatigue crack initiating from the damaged area, an explosion and complete loss of structural integrity may occur.

The subject of this investigation is to assess analytically (or numerically) the relation between the residual strength, i.e., the burst pressure of an impacted vessel, and the extent of damage incurred by the vessel in the event of impact. Eventually, the ultimate objective of this investigation is to establish the "accept or reject" criterion for impacted composite overwrapped pressure vessels (COPV), either spherical or cylindrical, as used either by the Air Force or in space applications. This criterion shall be derived from the damage tolerance procedures, and will be developed as the result of

- * analysis encompassing structural engineering approaches, i.e., solutions to certain boundary value problems and techniques offered by Fracture Mechanics;

- * computer assisted studies involving finite element codes;

- * further acquisition of experimental data.

2. Theoretical Preliminaries

Let us consider a segment of a thin shallow shell (when the ratio thickness/radius= h/R is less than 0.01, shell is considered "thin") of constant thickness h , subjected to an internal pressure $q(x,y)$ and containing a through the thickness line crack of length $2c$ (see Table 1). As a first approximation, we shall limit our considerations to elastic, isotropic and homogeneous segments of shells subjected to small deformations.

The basic variables in the theory of shallow shells are the out-of-plane displacement component $w(x,y)$ - in the thickness direction of the z -axis - and a stress function $F(x,y)$ which represents the stresses at the mid surface of the shell. Following Marguerre (1938) and Fung et al. (1974), the coupled differential equations governing w and F , with x and y chosen as Cartesian coordinates in the base plane, can be reduced to this form

$$\nabla^4 F = Eh \left[2 \frac{\partial^2 w}{\partial x \partial y} \frac{\partial^2 w}{\partial x \partial y} - \frac{\partial^2 w}{\partial x^2} \frac{\partial^2 w}{\partial y^2} - \frac{\partial^2 w}{\partial y^2} \frac{\partial^2 w}{\partial x^2} \right] \quad (2.1)$$

$$D\nabla^4 w = -q - 2\frac{\partial^2 F}{\partial x \partial y} \frac{\partial^2 w}{\partial x \partial y} + \frac{\partial^2 F}{\partial x^2} \frac{\partial^2 w}{\partial y^2} + \frac{\partial^2 F}{\partial y^2} \frac{\partial^2 w}{\partial x^2} \quad (2.2)$$

where $w_0(x,y)$ describes the initial shape of the shell in reference to that of a flat plate, while D and E are the flexural rigidity and Young's modulus, respectively. Even though these equations do not take into account the transverse anisotropy (orthotropy for our problem), neither do they address the dynamics of the impact loading on the shallow shell structure, they are useful in studying the possible choices of the kinematically admissible displacement functions needed in the variational techniques such as Rayleigh-Ritz method.

Closed-form solutions to so stated problem for an arbitrary initial curvature present formidable mathematical complexities. Certain exact asymptotic solutions valid for spherical and cylindrical shells, however, have been obtained, cf. references [2-4].

Without going into the mathematical details, the stress distribution around the crack tip for a symmetrical loading was found, cf. Folias (1974), to be

$$\sigma_x^{(e)} = P^{(e)} \left(\frac{c}{2r} \right)^{1/2} \left[\frac{3}{4} \cos \frac{\theta}{2} + \frac{1}{4} \cos \frac{5\theta}{2} \right] + o(r^0) \quad (2.3)$$

$$\sigma_y^{(e)} = P^{(e)} \left(\frac{c}{2r} \right)^{1/2} \left[\frac{5}{4} \cos \frac{\theta}{2} - \frac{1}{4} \cos \frac{5\theta}{2} \right] + o(r^0) \quad (2.4)$$

$$\tau_{xy}^{(e)} = P^{(e)} \left(\frac{c}{2r} \right)^{1/2} \left[-\frac{1}{4} \sin \frac{\theta}{2} + \frac{1}{4} \sin \frac{5\theta}{2} \right] + o(r^0) \quad (2.5)$$

for the membrane (or "extensional") state of stress, and

$$\sigma_x^{(b)} = P^{(b)} \left(\frac{c}{2r} \right)^{1/2} \left[-\frac{3-3\nu}{4} \cos \frac{\theta}{2} - \frac{1-\nu}{4} \cos \frac{5\theta}{2} \right] + o(r^0) \quad (2.6)$$

$$\sigma_y^{(b)} = P^{(b)} \left(\frac{c}{2r} \right)^{1/2} \left[\frac{11+5\nu}{4} \cos \frac{\theta}{2} + \frac{1-\nu}{4} \cos \frac{5\theta}{2} \right] + o(r^0) \quad (2.7)$$

$$\tau_{xy}^{(b)} = P^{(b)} \left(\frac{c}{2r} \right)^{1/2} \left[-\frac{7+\nu}{4} \sin \frac{\theta}{2} - \frac{1-\nu}{4} \sin \frac{5\theta}{2} \right] + o(r^0) \quad (2.8)$$

for the stresses due to bending on the tension side of the shell. Here, ν is Poisson ratio and (r, θ) are the polar coordinates around the crack tip. The load/geometry coefficients $P^{(e)}$ and $P^{(b)}$ are functions of the crack size, geometry of the shell, material properties and loading characteristics. While the exact expressions for the coefficients $P^{(e)}$ and $P^{(b)}$ can be found in reference [10], some engineering approximate formulae for commonly encountered loading schemes and with error below 7% are quoted in Table 1. The geometry dependent parameter λ is defined as follows

$$\lambda = \left(\frac{Ehc^4}{R^2D} \right)^{1/4} = \{12(1 - \nu^2)\}^{1/4} \left\{ \frac{R}{h} \right\}^{1/2} \frac{c}{R} = \{12(1 - \nu^2)\}^{1/4} \frac{c}{(Rh)^{1/2}} \quad (2.9)$$

A Fracture Mechanics model suggested by Folias (1974) provides the following expression for the critical hoop stress

$$\sigma_h = \sigma_F \left\{ \frac{1 + 0.317\lambda^2 \left(\frac{1-\alpha}{\alpha} \right)^2}{1 + 0.317\lambda^2 \left(\frac{1}{\alpha} \right)^2} (1 - \alpha) \right\}^{1/2} \quad (2.10)$$

in where σ_F is the so-called flow stress suggested by McClintock

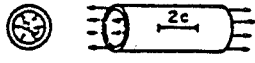
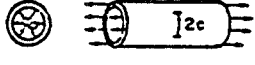
$$\sigma_F = \frac{1}{2} \left\{ \sigma_Y + \frac{\sigma_Y + \sigma_U}{2} \right\} \quad (2.11)$$

(with σ_Y denoting yield stress and σ_U being the UTS), while the variable α expresses the ratio of the actual to the effective (i.e., corrected for the plasticity effects) crack length. This ratio is related to the crack length c , material toughness K_{Ic} and the flow stress in the following way

$$\alpha = \frac{c}{c_e} = \exp \left[\frac{-\pi K_{Ic}^2}{8c \sigma_F^2} \right] \quad (2.12)$$

For negligible plasticity effects α approaches zero.

TABLE 1

<p>Long cylinder axial crack</p> 	$P(e) \approx \sqrt{1 + 0.317\lambda^2} \quad (q_0 R/h)$ $P(b) \approx 0$
<p>Long cylinder peripheral crack</p> 	$P(e) \approx \sqrt{1 + 0.05\lambda^2} \quad (q_0 R/2h)$ $P(b) \approx 0$
<p>Spherical cap</p> 	$P(e) \approx \sqrt{1 + 0.466\lambda^2} \quad (q_0 R/2h)$ $P(b) \approx 0$

3. Effect of Rate of Loading on Material Toughness

Graphite/epoxy laminates are a special class of composites which possesses a definite strength-to-weight advantage over many standard engineering materials used in aerospace applications. This advantage is somewhat lessened, however, by their sensitivity to operational hazards such as low-velocity impact by foreign objects. Impact may cause delamination damage since the strength of the plate (or structure) in its thickness direction is quite low. Under service loads this delamination may grow and lead to a global failure of the structure at load well below the design level.

In contrast to metals most high-strength graphite/epoxy composite laminates lack ductile response. Therefore, composite structures are sensitive to local strain concentrations, either pre-existing or those incurred in service. They are also sensitive to the **rate of loading**, especially at high-velocity impact. Such sensitivity may trigger localized failure which in turn reduces the local stiffness and transfers high strain concentrations into adjacent regions, resulting in **propagation** of damage, cf. Kriz and Wnuk (1985).

To assess effects of the loading rate on the initial stages of fracture in the composite, the so-called R-curve approach is employed here, compare Wnuk et al. (1996). To exemplify the use such "resistance curve" methodology in evaluating degradation of material toughness, let us choose a configuration of a central crack

contained in an infinite width plate subject to tensile stress. Then $R = \frac{1}{2} Q^2 (\ell) \ell$

$Q = \pi \sigma / 2 \sigma_o$, and the governing equation of motion, which describes the variations of the resistance parameter R as crack propagates, becomes

$$\frac{dR}{d\ell} = \frac{\hat{R} - \frac{\Delta}{2} \log\left(\frac{4R}{\Delta}\right) + \Delta C R^2 / \ell \sqrt{2\ell R}}{\Delta + \Delta C R / \sqrt{2\ell R}} \quad (3.1a)$$

Both R and ℓ are expressed in Δ units, and this leads to some astronomical numbers. To avoid such inconvenience, new variables are suggested, much more suitable for the numerical work. Setting

$$\begin{aligned} \log (\ell / \Delta) &= X \\ \log (R / \Delta) &= Y, Y = Y(X) \end{aligned} \quad (3.1b)$$

we transform equation (3.1) into the form

$$\frac{dY}{dX} = \frac{A - \frac{1}{2}Y + (C/\sqrt{2}) \exp \left[\frac{3}{2}(Y - X) \right]}{1 + (C/\sqrt{2}) \exp \left[\frac{1}{2}(Y - X) \right]} \quad (3.2)$$

This is the final form of the equation of motion used for numerical integration. The constant

$A = (\alpha + 1) - \frac{1}{2} \log(4e)$. Fig.2 gives some examples of the resulting integral curves.

Now, the “universal” R curve is seen to be strongly affected by the rate-sensitivity parameter C (which includes the material-sensitivity $\dot{\Psi}(0)$ and the rate of loading \dot{Q} , $C = \dot{\Psi}(0)/B$). It can be also shown that the R curve is no longer a function of the difference $(\ell - \ell_o)$ only, but rather it depends on the current length ℓ .

It is seen from Fig.2 that the extent of subcritical growth is substantially dependent on the rate-sensitivity. In particular, the final instability points for the three runs shown can be read out directly from the curves R vs. $\Delta\ell$, since they coincide in each case with the points at which the slope dY/dX equals unity. They are

$$\begin{array}{lll} \text{At } C = 0, & \ell_f/\Delta = 1153 & R_f/\Delta = 5710 \\ \text{At } C = 1, & \ell_f/\Delta = 5064 & R_f/\Delta = 22026 \\ \text{At } C = 10, & \ell_f/\Delta = 268337 & R_f/\Delta = 627814 \end{array} \quad (3.3)$$

The index “f” stands for “failure”.

For engineering applications it is convenient to rewrite the governing equation (2.20) in terms of the ratios R/R_{SS} and ℓ/R_{SS} , where R_{SS} denotes the steady-state limit of the size of nonlinear zone, related to the K_{SS} fracture parameter in this way:

$$R_{ss} = \pi K_{ss}^2 / 8 \sigma_o^2$$

The symbol K_{SS} denotes the maximum plane stress fracture toughness which would be attained in an ideal case, when the conditions of the test are such that the subcritical crack growth is fully developed. Of course, in most practical cases the actual critical fracture toughness value attained at the terminal instability, say K_c , is bracketed by the initiation toughness K_i and the steady-state level K_{SS} .

If we define

$$Q = \pi\sigma / 2\sigma_o \quad (3.4)$$

then for the central crack contained in an infinite plate we have

$$R = \frac{1}{2} Q^2 \ell \quad (3.5)$$

and for a central crack located in a panel of width $2b$ we have

$$R = \frac{1}{2} Q^2 \ell \sec\left(\frac{\pi\ell}{2b}\right) \quad (3.6)$$

The corresponding equations governing the subcritical growth take on the form

$$\frac{dR}{d\ell} = \frac{\frac{1}{2} \log(R_{ss}/R) + CR^2 / \ell \sqrt{2\ell R}}{1 + CR / \ell \sqrt{2\ell R}} \quad (3.7)$$

$$\frac{dQ}{d\ell} = \frac{\log(R_{ss}/Q^2\ell) - Q^2}{\ell Q(2 + CQ)} \quad (3.7)$$

for an infinite plate, and

$$\frac{dR}{d\ell} = \frac{\frac{1}{2} \log(R_{ss}/R) + CR^2 \{1 + (\pi\ell/2b) \tan(\pi\ell/2b)\} / \ell \sqrt{2\ell R} \sec(\pi\ell/2b)}{1 + CR / \sqrt{2\ell R} \sec(\pi\ell/2b)} \quad (3.8)$$

$$\frac{dQ}{d\ell} = \frac{\log[(R_{ss}/Q^2\ell \sec(\pi\ell/2b))] - Q^2 [1 + (\pi\ell/2b) \tan(\pi\ell/2b)] \sec(\pi\ell/2b)}{\ell Q(2 + CQ) \sec(\pi\ell/2b)}$$

Effect of tearing modulus on the fracture enhancement ratio and the margin of safety with respect to onset of crack growth

NOTE: minimum tearing modulus at $\dot{Q}_c=10$ is $M_{min}=2.3444$

TABLE 2

M (at $\dot{Q}_c = 10$)	$\mathcal{L} = J_{cg}/J_c$	margin of safety
2.3444	1.0000	0 (brittle fracture)
2.35	1.0112	1.12%
2.40	1.1175	11.75%
2.50	1.3649	36.49%
2.60	1.6672	66.72%
2.70	2.0363	103.63%
2.80	2.4871	148.71%
2.90	3.0378	203.78%
3.00	3.7103	271.03%

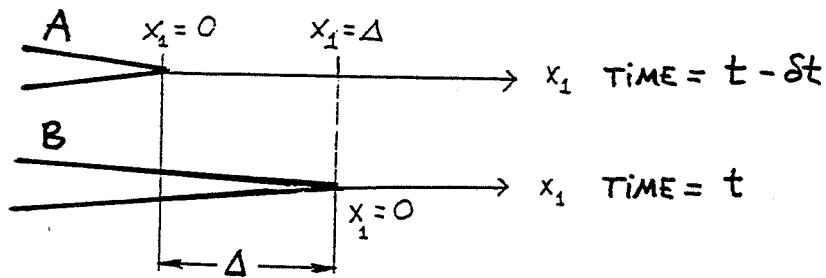


Fig. 1. Two subsequent states A and B corresponding to quasi-static propagation of the crack by a unit growth step Δ .

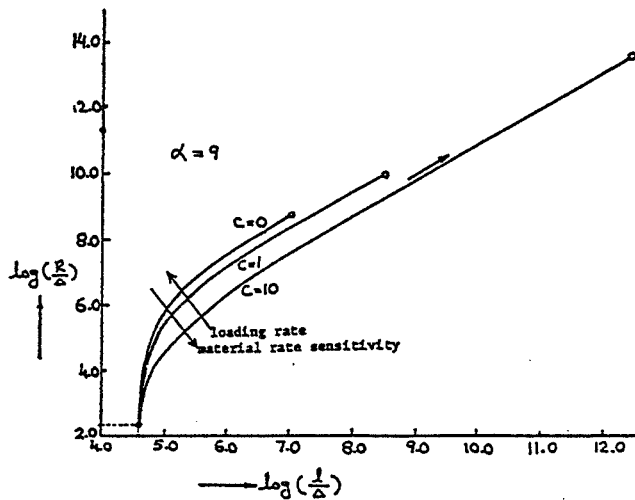


Fig. 2. Slow growth of a crack in a ductile rate-dependent solid. Ultimate instability is reached when the slope of the R-curve plotted on log-log scale equals unity (points are marked with circles). Initial crack size is 100Δ .

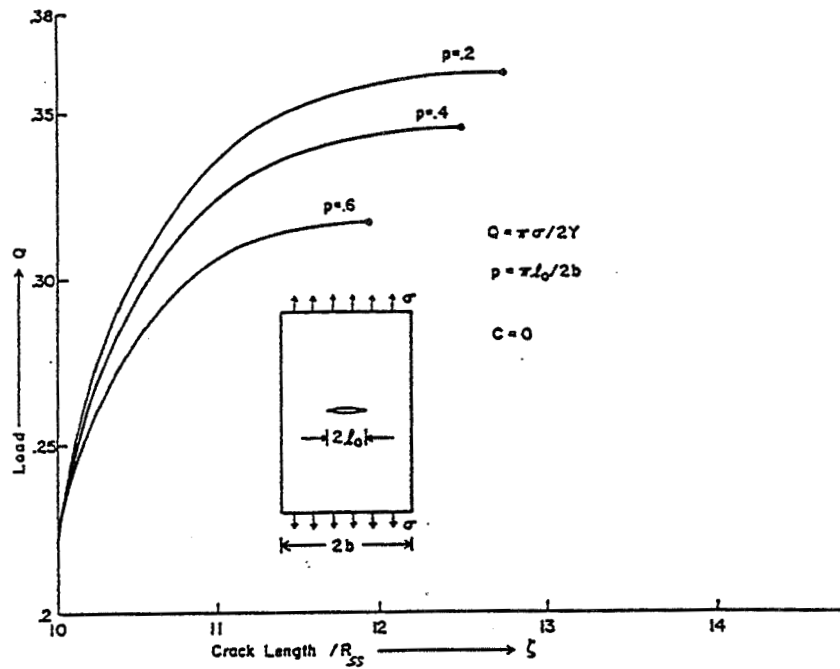


Fig. 3(a) $C = B/\dot{Q} = 0$

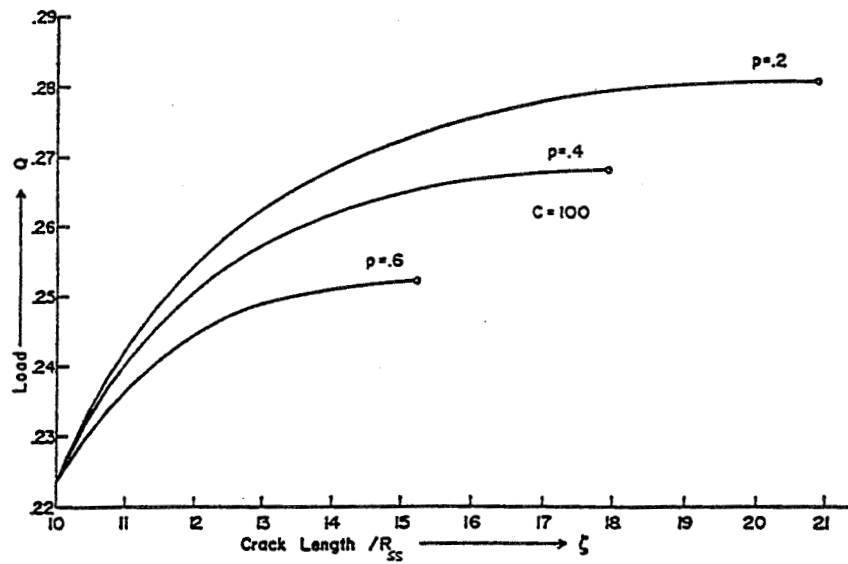


Fig. 3(b) $C = B/\dot{Q} = 100$

Fig. 3. Slow growth in a finite width panel containing a central crack; two different material rate-sensitivity (or rate of loading) levels are considered.

for a finite plate. The locus of terminal instability follows readily from Eqs. (3.7b) and (3.8b) if $dQ/d\ell$ is set equal zero. Then for an infinite plate we obtain

$$\ell_f = R_{ss} Q_f^{-2} \exp(-Q_f^2) \quad (3.9)$$

while for a finite width panel we have

$$\begin{aligned} & \log \left[2R_{ss} / Q_f^2 \ell_f \sec(\pi \ell_f / 2b) \right] \\ & = Q_f^2 \left[1 + (\pi \ell_f / 2b) \tan(\pi \ell_f / 2b) \right] \times \sec(\pi \ell_f / 2b) \end{aligned} \quad (3.10)$$

Of course, equations (3.7) and (3.9) are “contained” in equations (3.8) and (3.10) respectively, and can be deduced from the latter by simply setting the panel width $b = \infty$. Examples of the subcritical growth in a finite width panel due to a monotonically increasing load are shown in Figs.3 a and b.

Interestingly, the rate-sensitivity C does not enter explicitly in the relations (3.9) and (3.10). It is present here, though, in an implicit way, since both the critical load Q_f and the critical crack size ℓ_f are significantly affected by the rate-sensitivity. This can be seen only **after** the integration of equations (3.7b) and (3.8b) is completed.

In general, we conclude then, that the amount of slow crack growth prior to the terminal instability distinctly depends on the following variables

1. Ductility.
2. Rate sensitivity.
3. Rate of loading.
4. Initial crack size.
5. Geometry of the test.

These conclusions are clearly illustrated by the graphs shown in Figs.2-3. The results discussed in this presentations are valid for small scale yielding range and linear (or nearly linear) viscoelastic response of the medium weakened by a crack and subjected to variable rates of loading.

To establish analogous relationships for a large scale yielding case would require a much more complete analytical investigation.

4. Outline of the Follow-up Research Program

The future research on the assessment of influence of damage induced by impact on the residual strength of space flight composite overwrapped pressure vessels (COPV) will consists of three parallel programs:

1. Analytical work addressing the pertinent boundary value problems and encompassing structural engineering, mechanics of composites and Fracture Mechanics.

2. Numerical investigation of related problems such as propagation of damage caused by low- or high-velocity impact in the composite overwrapped pressure vessel. In this particular field we anticipate to develop a cooperative research program with Professor Phillippe Guebelle of the Department of Aero and Astro Engineering at the University of Illinois at Urbana Champaign. Professor Guebelle is currently working on a development of a new FE code compatible with a super-fast computer available at his campus.

3. Experimental program which should focus on

- More precise measurements of the extent and mode of damage incurred within the graphite/epoxy composite. Modified NDE techniques should be employed including C-scan, acoustic emission and infra-red radiation to make the damage visible and provide a visual record of various modes of damage. Concurrently with these tests an investigation should be launched to determine the optimum placement and orientation of fibers in the laminae, so that the protective layer of composite would dissipate the maximum energy at impact.
- Experimental effort should be made to establish occurrence of the “characteristic damage state” (CDS) which is indicative of imminent fracture. This will require a large number of tests. It is expected, though, that an empirical correlation between the CDS and the energy imparted to the vessel at impact will eventually emerge from these tedious and time consuming tests.
- Acquisition of local stress vs. strain data aimed at better understanding of the dynamics of the material properties degradation associated with evolution of damage during the impact process.
- More precise measurements of the out-of-plane displacements incurred during impact. Application of the optical method adapted by Chai et al. (1983) to measure shadow moiré patterns seems to be good choice. Another possibility would be to adapt the latest ultra-fast technology, available now at Caltech, to record optically the out-of-plane displacements during a dynamic loading event, cf. Lambros and Rosakis [9, 10].

Our plan for the future involvement in this research program is outlined briefly in the remainder of this report (see also the NASA Proposal dated July 23, 1996, submitted to NASA/WSTF for divisional funding).

Analytical work will be based on the global or “structural engineering” approach involving statement of the appropriate boundary value problems, derivation of the governing partial differential equations expressed either in terms of the displacement

field components or the stress potential, and the presentation of the solution methodology will be the primary aspect of this investigation. In addition to these Continuum Mechanics considerations, the analysis of the catastrophic failure in pressurized vessels, based on Fracture Mechanics approach, cf. Folias (1974), will be incorporated into the program.

Extension of the Cairns and Lagace (1989) theory of plate impact will be worked out for the cylindrical geometry retaining the essential features of their mathematical model, compare also the review of all other available mathematical approaches to the problem of impact on laminated composites as given by Abrate (1991).

Admissible solutions to the governing equations of the problem in conjunction with the fundamental theorems of the Calculus of Variations will be suggested. Finally, basing on this theoretical investigation it is expected that we will be able to show the interrelations between the following variables:

energy of impact ~ extent of the delaminated area in the protective composite layer ~ secondary damage modes associated with dynamic interaction of the COPV with impactor ~ reduction of the burst pressure ~ damage tolerance.

Briefly, a computational model will be worked out which may be represented by a black box for which the **input** is designated as the energy imparted to the COPV during the act of impact, while the ultimate **output** is a quantified estimate of the structural integrity of the pressure vessel measured by the residual burst pressure attained in a monotonic loading process. In summary, the most essential goal of this research project is to establish the quantitative guidelines for damage tolerance procedures on the impacted COPVs.

At this point it is expected that in order to correlate the analytical results with the experimentally available data, it will be necessary for the NASA colleague to perform some additional measurements pertaining to the **local stiffness** of the damage region and to obtain a more precise evaluation of the extent (and mode) of the damaged volume by use of an appropriate NDE technique.

Since some aspects of the problem stated above may be mathematically intractable, a parallel numerical investigation employing a finite element code will be launched. Samples of these calculations were shown to my NASA colleagues; they involve dynamically loaded bi-material plates simulating an element of the COPV cut along the principal orientations. Some models have been proposed to predict the initiation of impact-induced damage, cf. Geubelle (1996), but very little data are available to predict the propagation and extent of the delamination (crucial for establishing the damage tolerance procedures and evaluation of the residual structural integrity of the pressure vessels). The code used currently by Prof. Guebelle at University of Illinois at Urbana-Champaign will be expanded to accommodate the need for a very large number of degrees of freedom, required for the numerical representation of the impact problem (nodes must be rapidly relaxed and superposed

along cohesive elements to allow for the dynamic separation process). This will require the use of advanced computational facilities, such as the massively parallel machines available now at the National Center for Supercomputing Applications (NCSA) located on the U. of Illinois at Urbana-Champaign campus. Toward this end we foresee a closer cooperation with Professor Phillippe Geubelle and his graduate students in the Department of Aero and Astro Engineering of the University of Illinois at Urbana-Champaign.

REFERENCES

- [1] K. Marguerre, 1938, "Zur Theorie der Gekrumnten Platte Grosser Formanderung", in Proceedings of the 5th International Congress of Applied Mechanics, pp. 93-101.
- [2] E. S. Folias, 1965 Int. J. Fracture, Vol. 1, No. 1, pp.20-46.
- [3] E. S. Folias, 1969, "On the Effect of Initial Curvature on Cracked Flat Sheets", Int. J. Fracture, Vol. 5, No. 4, pp.327-346.
- [4] E. S. Folias, 1974, "On the Prediction of Catastrophic Failures in Pressurized Vessels", in "Prospects of Fracture Mechanics - Proceedings of Int. Conference", Delft University of Technology, publ. by Noordhoff Int. Publishers, Leiden, The Netherlands, pp. 405-418.
- [5] Y. C. Fung and E. E. Sechler, 1974, "Thin Shell Structures", book publ. by Prentice-Hall, Chapter 21.
- [6] H. Chai, W. G. Knauss and C. D. Babcock, 1983, "Observation of Damage Growth in Compressively Loaded Laminates", Experimental Mechanics, Vol. 23, No. 3, pp. 329-337.
- [7] M. P. Wnuk and R. Kriz, 1985, "CDM Model of Damage Accumulation in Laminated Composites", Int. J. Fracture, Vol. 28, pp.121-138.
- [8] M. P. Wnuk, M. Choroszynski and A. N. Joshi, 1996, "Rate Dependent Resistance Curves in Viscoelastic-Plastic Solids", paper to be presented at Int. Conference on MESOFRACTURE, Tomsk, RF, August 27-31, 1996; submitted to Int. J. Fracture.
- [9] J. Lambros and A. J. Rosakis, 1996, "Dynamic Crack Initiation and Growth in Thick Unidirectional Graphite/Epoxy Plates", Progress Report "GALCIT 96" on research sponsored by ONR, California Institute of Technology, Pasadena, CA.
- [10] J. Lambros and A. J. Rosakis, 1995, "Dynamic Delamination and Fracture in Thick Fiber Reinforced Composites", Progress Report on research sponsored by the Office of Naval Research, California Institute of Technology, Pasadena, CA.

REPORT DOCUMENTATION PAGE			Form Approved OMB No. 0704-0188	
Public reporting burden for this collection of information is estimated to average 1 hour per response, including the time for reviewing instructions, searching existing data sources, gathering maintaining the data needed, and completing and reviewing the collection of information. Send comments regarding this burden estimate or any other aspect of this collection of information, incl suggestions for reducing this burden, to Washington Headquarters Services, Directorate for Information Operations and Reports, 1215 Jefferson Davis Highway, Suite 1204, Arlington, VA 22202- and to the Office of Management and Budget, Paperwork Reduction Project (0704-0188), Washington, DC 20503.				
1. AGENCY USE ONLY (Leave Blank)	2. REPORT DATE June 1997	3. REPORT TYPE AND DATES COVERED Contractor Report		
4. TITLE AND SUBTITLE National Aeronautics and Space Administration (NASA)/American Society for Engineering Education (ASEE) Summer Faculty Program - 1996 Volume 2			5. FUNDING NUMBERS	
6. AUTHOR(S) Richard B. Bannerot* and Donn G. Sickorez, Editors				
7. PERFORMING ORGANIZATION NAME(S) AND ADDRESS(ES) Lyndon B. Johnson Space Center Houston, Texas 77058			8. PERFORMING ORGANIZATION REPORT NUMBERS	
9. SPONSORING/MONITORING AGENCY NAME(S) AND ADDRESS(ES) National Aeronautics and Space Administration Washington, D.C. 20546-0001			10. SPONSORING/MONITORING AGENCY REPORT NUMBER CR-202008	
11. SUPPLEMENTARY NOTES * University of Houston; Houston, Texas				
12a. DISTRIBUTION/AVAILABILITY STATEMENT Unclassified/Unlimited Available from the NASA Center for AeroSpace Information (CASI) 800 Elkridge Landing Road Linthicum Heights, MD 21090-2934 (301) 621-0390 Subject Category: 99			12b. DISTRIBUTION CODE	
13. ABSTRACT (Maximum 200 words) The 1996 JSC NASA/ASEE Summer Faculty Fellowship Program was conducted by the University of Houston and JSC. The objectives of the program, which began nationally in 1964 and at JSC in 1965 are to (1) further the professional knowledge of qualified engineering and science faculty members, (2) stimulate an exchange of ideas between participants and NASA, (3) enrich and refresh the research and teaching activities of participants' institutions, and (4) contribute to the research objectives of the NASA centers. Each faculty fellow spent at least 10 weeks at JSC engaged in a research project in collaboration with a NASA JSC colleague. This document is a compilation of the final reports on the research projects completed by the faculty fellows during the summer of 1996.				
14. SUBJECT TERMS information transfer, research, research projects, urban research, engineering, science, universities, university program			15. NUMBER OF PAGES 161	16. PRICE CODE
17. SECURITY CLASSIFICATION OF REPORT Unclassified	18. SECURITY CLASSIFICATION OF THIS PAGE Unclassified	19. SECURITY CLASSIFICATION OF ABSTRACT Unclassified	20. LIMITATION OF ABSTRACT Unlimited	